

Interfacial Area Transport Equation Models and Validation against High Resolution Experimental Data for Small and Large Diameter Vertical Pipes

by

Akshay J. Dave

A dissertation submitted in partial fulfillment
of the requirements for the degree of
Doctor of Philosophy
(Nuclear Engineering and Radiological Sciences)
in the University of Michigan
2016

Doctoral Committee:

Associate Professor Annalisa Manera, Chair
Stephen Bajorek, United States Nuclear Regulatory Commission
Professor Thomas J. Downar
Assistant Professor Eric Johnsen
Professor Edward W. Larsen
Research Scientist Victor E. Petrov

To my family.

Acknowledgements

I am grateful for the constructive advice and support given by both Professor Manera and Dr. Petrov throughout my time at the Experimental and Computational Multiphase Flow group. Professor Manera has been an outstanding mentor – guiding me towards improving my research skills.

Additionally, I would like to thank the University of Michigan faculty members who have taught me throughout my graduate career. A special thanks to Dr. Beyer and Dr. Lucas from HZDR, and Dr. Prasser from ETH Zurich for their willingness to help with the wire-mesh sensor software and TOPFLOW experimental data.

The analyses presented in this work were sponsored by the United States Nuclear Regulatory Commission, grant No. NRC HQ 60 14 G 0008. The TOPFLOW experiments and the development of the original wire-mesh sensor software were carried out within the framework of research projects funded by the German Federal Ministry for Economic Affairs and Energy, project numbers: 150 1411 and 150 1329.

Contents

Dedication		ii
Acknowledgements		iii
List of Figures		vi
List of Tables		x
Nomenclature		xii
Abstract		xiv
Chapter 1	Introduction	1
1.1	Nuclear Plant Operation	1
1.1.1	Application to other plants	3
1.2	Multiphase Modelling	4
1.2.1	Two-fluid Model	5
1.2.2	Regime Map	7
1.2.3	Interfacial area transport equation	10
1.3	Experimental Methods	14
1.3.1	X-ray and γ -ray tomography	14
1.3.2	Needle probe sensor	16
1.3.3	Wire-mesh sensor	18
1.4	Experimental Database	21
1.5	Previous Evaluations	22
1.6	Objectives	24
1.6.1	Outline	24
Chapter 2	Wire-mesh Sensors	26
2.1	Background	26
2.1.1	Wire-mesh Sensor Operation	26
2.1.2	Post-processing Algorithms	29
2.2	Uncertainty Analysis	33
2.2.1	Convex Hull Algorithm	34
2.2.2	Multiple Spherical Bubbles	35
2.2.3	Sensor Operating Frequency	36
2.2.4	Ideal Bullet Bubble	38

	2.2.5	Ideal Bullet Bubble with Internal Cavity	39
	2.2.6	Bubbles Approaching Coalescence	42
2.3		Remarks	44
Chapter 3		Two-group Interfacial Area Transport Equation	45
3.1		Formulation	46
	3.1.1	Existing Two-group Models	49
3.2		Experimental Database	52
	3.2.1	TOPFLOW DN50	52
	3.2.2	TOPFLOW DN200	53
	3.2.3	Application of TOPFLOW Data	54
3.3		Fu-Ishii Model	55
	3.3.1	Interaction Mechanisms	55
	3.3.2	Evaluation	62
	3.3.3	Remarks	70
3.4		Smith-Schlegel Model	71
	3.4.1	Scaling Effects in Larger Diameters	72
	3.4.2	Interaction Mechanisms	73
	3.4.3	Evaluation	79
	3.4.4	Remarks	87
Chapter 4		Optimization Studies	89
4.1		Genetic Algorithm	93
	4.1.1	Implementation	95
4.2		Optimization of Fu-Ishii Model	96
	4.2.1	Individual Optimization	96
	4.2.2	Global Optimization	98
	4.2.3	Localized Optimization of Group-2 Wake Entrainment	102
	4.2.4	Remarks	107
4.3		Optimization of Smith-Schlegel Model	108
	4.3.1	Individual Optimization	108
	4.3.2	Global Optimization	110
	4.3.3	Remarks	113
Chapter 5		Conclusions	114
Appendix			120
References			131

List of Figures

1.1	Generalized schemes for BWRs and PWRs [1].	2
1.2	Generalized two-phase flow regimes that are typical for a vertical small diameter pipe. The dark green color represents steam, while the light green color represents water. Example of typical flow regimes observed experimentally are presented in Fig. 3.14.	3
1.3	Diagram showcasing the dependencies of the two-fluid model [32].	5
1.4	Example of pre-CHF flow regime map used by TRACE V5 [2].	8
1.5	Example of post-CHF flow regime map used by TRACE V5 [2].	9
1.6	An overview of bubble interaction mechanisms that are considered by the interfacial area transport equation model. Vertical orientation indicates the upstream position of the bubbles during the interaction. Color indicates relative expected bubble size.	13
1.7	A γ -ray tomograph indicating void fraction distribution for a 26.35 cm pipe with $v_g = 5.0$ m/s [43].	15
1.8	Slices of a reconstructed image for a single slug bubble with artificial noise [9].	16
1.9	Diagram of double-sensor and four-sensor conductivity probes with typical dimensions [39]. The conductivity probes are an intrusive measurement technique.	17
1.10	CAD of a wire-mesh sensor assembly that is placed into the vertical test section of the TOPFLOW DN200 assembly [8].	18
1.11	Examples of the high resolution capabilities of the wire-mesh sensor. Post processing methods can be used to carefully study the interfacial structure of complicated bubble structures [60].	19
1.12	A comparison of void fraction distributions measured with X-ray tomography and wire-mesh sensor for $j_g = 0.3$ m/s [61].	20
1.13	A comparison of interfacial area concentration measurements using wire-mesh sensor (continuous) and needle probe for $j_g = 2.1$ m/s and $j_f = 2.6$ m/s in a vertical 50.8 mm pipe [48]. The data is separated by bubble diameter.	21
1.14	An overview of the dissertation organization.	24
2.1	Simplified diagram of circuits used in the operation of the wire-mesh sensor [57].	27
2.2	Diagram of control signals [57].	27
2.3	Histogram of the raw voltage measured for mesh (43,43), test 140, for the large diameter TOPFLOW test [8].	28

2.4	Wire intersections measure local conductivity. Intersections at the edge need to account for a smaller area of influence.	29
2.5	Schematic of a two-level wire-mesh sensor assembly. The separate wire-mesh sensors are highlighted in red [8].	30
2.6	A hexahedral domain about a void fraction point under analysis and its neighbors; the spatial dimensions are indicated by the axis kk and jj , temporal dimension is indicated by axis ii	32
2.7	Detection of liquid-gas interface at the horizontal faces of prisms formed within the hexahedral domain.	32
2.8	Triangularization of a skew quadrilateral in order to determine the area of the liquid-gas interface. There are 10 groups of $g(0 \rightarrow 9)$ that consist of two triangles each ($sq1$ and $sq2$). Areas of the triangles are calculated by vectors ($\vec{x}11, \vec{x}21, \vec{x}12$ and $\vec{x}22$).	33
2.9	A 3D scatter plot of a bullet bubble's coordinates generated by the HZDR algorithm (left). The convex hull of the coordinates generated by CGAL (right).	35
2.10	Error on interfacial area concentration for a set of 1000 Spherical bubbles ranging between 3 mm to 10 mm in diameter, with velocity of 1 m/s.	36
2.11	Error for 2000 (left) and 4000 (right) Spherical bubbles between between 3 mm to 10 mm in diameter, with velocity of 1 m/s.	36
2.12	Illustration of the impact of increasing operating frequency on capturing data.	37
2.13	Error for varying operating frequencies for a 3 mm spherical bubble at 1 m/s.	37
2.14	Error for varying operating frequencies for 5 mm (left) and 10 mm (right) spherical bubbles at 1 m/s	38
2.15	Error for varying bubble diameter at a constant operating frequency of 2.5 kHz (0.4 mm bubble displacement between frames) at 1 m/s.	38
2.16	Error for a 10 mm ideal bullet shaped bubble with varying tail lengths at at 1 m/s.	39
2.17	Error for a 10 mm ideal bullet shaped bubble with an internal cavity and varying tail lengths at at 1 m/s.	40
2.18	Three separate frames during the computational analysis of the bullet bubble with cavity. The continuous lines indicate the synthetic shape's inner and outer edge. Discrete data represent points that have been interpolated by the HZDR algorithm.	41
2.19	A 3D representation of the void fraction distribution generated for analysis in Case 3, Table 2.1.	42
2.20	Visual of a 15 mm bubble coalescing into a 20 mm bubble traveling vertically at 1 m/s. The numeric values indicate the normalized proximity of the bubble centroids.	43
2.21	Error for bubbles approaching coalescence.	43
3.1	Classification of bubbles and variation in interfacial drag in group 1 and group 2.	46

3.2	A diagram of various interaction mechanisms that are considered in the two-group model. Vertical orientation indicates the upstream position of bubbles during the interaction. Green bubbles belong to group-1 and orange bubbles belong to group-2.	51
3.3	A visual of the TOPFLOW DN50 and DN200 test sections [8].	52
3.4	Assumption of bubble population distributions in Fu-Ishii model [22].	56
3.5	Wake entrainment of large group-2 bubbles [22].	59
3.6	Assumed geometry for modelling shearing-off (a) and volume of gas sheared off (b) [22].	62
3.7	Anticipated flow regimes in DN50 TOPFLOW tests.	63
3.8	A comparison of performance for DN50 TOPFLOW data. Left column indicates error for group 1 interfacial area concentration and right column indicates error for group 2 interfacial area concentration. The third column indicates error for prediction of total interfacial area.	63
3.9	Results for Test 30 using the 2G IATE model.	65
3.10	Results for Test 94 using the 2G IATE model.	65
3.11	Results for Tests 115 to 119 using the 2G IATE model.	66
3.12	Results for Tests 96, 107, 118, 129, and 140 using the 2G IATE model.	68
3.13	A comparison of performance for DN50 TOPFLOW data. Left column indicates error for standalone IATE model, center column indicates error for two-fluid IATE model. The right column presents the experimental void fraction contribution from group 2 bubbles.	70
3.14	Virtual side projections of void distributions from wire mesh sensor measurements in DN50 test section (left) and DN200 test section (right) for $j_f = 1$ m/s [58].	72
3.15	Flow regime map for DN200 experimental conditions using criteria proposed by Schlegel [67]. In comparison to Fig. 3.7, no stable slug flow regime exists.	73
3.16	Assumption of bubble population distributions in Smith-Schlegel model [73].	75
3.17	A comparison of performance for DN200 TOPFLOW data. Left column indicates error for group 1 interfacial area concentration and right column indicates error for group 2 interfacial area concentration. The third column indicates error for prediction of total interfacial area.	80
3.18	IATE results for Test 17 and 42.	81
3.19	IATE results for tests 52, 63, 74, and 85.	82
3.20	IATE results for tests 116, 117, 118, and 119.	83
3.21	IATE results for Test 140 and 160.	85
3.22	Performance for DN200 TOPFLOW data with interaction mechanisms nullified. Left column indicates error for group 1 interfacial area concentration and right column indicates error for group 2 interfacial area concentration. The third column indicates error for prediction of total interfacial area.	87
4.1	A comparison of performance for DN50 TOPFLOW data.	90
4.2	A comparison of performance for four sets of Purdue University experimental data.	90

4.3	A comparison of performance for DN200 TOPFLOW data. Left column indicates error for group 1 interfacial area concentration and right column indicates error for group 2 interfacial area concentration. The third column indicates error for prediction of total interfacial area.	92
4.4	A comparison of performance for two sets of Purdue University experimental data.	93
4.5	Results for optimizing individual TOPFLOW DN50 tests. The improvement in predicting interfacial area ($\Delta(a_i)$ using Eq. (4.3)) is presented at the top. The relative change in coefficient values (δC using Eq. (4.4)) is presented. . .	97
4.6	Improvement of performance for DN50 TOPFLOW data using optimized \vec{C}	99
4.7	Results for Tests 115 to 118 using the 2G IATE model.	100
4.8	Improvement of performance for Purdue University data using optimized \vec{C}	101
4.9	Principle components biplot for 50th percentile and above genetic algorithm candidates.	103
4.10	Improvement of performance for TOPFLOW DN50 data using optimized C_{WE}^2	104
4.11	Results for Tests 115 to 118 using the 2G IATE model.	105
4.12	Improvement of performance for Purdue University data using optimized C_{WE}^2	105
4.13	Results for optimizing individual TOPFLOW DN200 tests. The improvement in predicting interfacial area ($\Delta(a_i)$ using Eq. (4.3)) is presented at the top. The relative change in coefficient values (δC using Eq. (4.4)) is presented. . .	109
4.14	Improvement of performance for TOPFLOW DN200 data using optimized \vec{C}	110
4.15	Improvement of Smith-Schlegel performance for Test 160. Both tests use the same legends.	112
4.16	Improvement of performance for large diameter Purdue tests using optimized \vec{C}	113
5.1	Preliminary DNS results in attempting to simulate shearing-off effects for a slug bubble.	119

List of Tables

1.1	Summary of existing experimental database suitable for vertical small diameter interfacial area transport equation development. Regimes: (1) bubbly, (2) slug, (3) churn-turbulent, (4) annular.	22
1.2	Summary of existing experimental database suitable for vertical large diameter interfacial area transport equation development. Regimes: (1) bubbly, (2) cap-turbulent, (3) churn-turbulent, (4) annular.	22
2.1	Improvement of cavity detection in the HZDR algorithm. Error is calculated by Eq. (2.6).	42
3.1	Availability of existing models that are applicable to vertical two-phase flows.	49
3.2	Experimental test matrix for the DN50 TOPFLOW tests. Tests that have been executed and have available data are colored. The colors indicate flow regime.	53
3.3	Experimental test matrix for the DN200 TOPFLOW tests. Tests that have been executed and have available data are colored. The colors indicate flow regime.	54
3.4	List of various interaction mechanisms accounted for in the Fu-Ishii model. All parameters used by the model are listed in the last column [32, Ch. 11]. .	56
3.5	Average error calculated by Eq. (3.15) for standalone IATE ('ST') and two-fluid IATE ('TFT').	70
3.6	List of various interaction mechanisms accounted for in the Smith-Schlegel model. All parameters used by the model are listed in the last column [74]. .	74
3.7	Average error [%] for total interfacial area calculated by Eq. (3.15) for Smith-Schlegel model ('IATE') and IATE equations with only expansion term ('EXP').	87
4.1	A comparison of average error calculated by Eq. (3.15) for all TOPFLOW DN50 tests.	90
4.2	A comparison of average error calculated by Eq. (3.15) for 48.3 mm Purdue University tests.	91
4.3	A comparison of average error calculated by Eq. (3.15) for other Purdue University tests.	91
4.4	A comparison of average error calculated by Eq. (3.15) for all TOPFLOW DN200 tests.	92
4.5	A comparison of average error calculated by Eq. (3.15) for large diameter Purdue University tests.	93

4.6	Global optimization of all TOPFLOW DN50 tests. The change in coefficients and objective function is calculated by Eq. (4.4) and Eq. (4.3), respectively. .	98
4.7	Average error gain/loss calculated by Eq. (3.15) for all TOPFLOW DN50 tests using optimized \vec{C}	101
4.8	Average error gain/loss calculated by Eq. (3.15) for 48.3 mm Purdue tests using optimized \vec{C}	101
4.9	Average error gain/loss calculated by Eq. (3.15) for other Purdue tests using optimized \vec{C}	102
4.10	Principal components of genetic algorithm candidates in optimization of all Fu-Ishii coefficients for TOPFLOW DN50.	102
4.11	Results for localized optimization of group 2 wake entrainment.	104
4.12	Average error gain/loss calculated by Eq. (3.15) for TOPFLOW DN50 tests using optimized C_{WE}^2	106
4.13	Average error gain/loss calculated by Eq. (3.15) for 48.3 mm Purdue tests using optimized C_{WE}^2	106
4.14	Average error gain/loss calculated by Eq. (3.15) for other Purdue tests using optimized C_{WE}^2	106
4.15	Global optimization of all TOPFLOW DN200 tests. The change in coefficients and objective function is calculated by Eq. (4.4) and Eq. (4.3), respectively. .	110
4.16	Average error gain/loss calculated by Eq. (3.15) for all TOPFLOW DN200 tests using optimized \vec{C}	111
4.17	Average error gain/loss calculated by Eq. (3.15) for for large diameter Purdue tests using optimized \vec{C}	112

Nomenclature

Abbreviations

1G	One-group classification, see Section 1.2.3
2G	Two-group classification, see Section 3.1
IATE	Interfacial area transport equation, see Section 1.2.3
WMS	Wire-mesh sensor, see Section 1.3.3

Greek

α	Void fraction of gas phase
χ	IATE distribution parameter
ε	Turbulence dissipation rate
Γ	Rate of mass generation
μ	Dynamic viscosity
ϕ	Interfacial area source/sink rate
ρ	Density
σ	Surface tension
τ	Stress tensor
ξ	Heat dissipation rate

Roman

a_i	Interfacial area concentration
C	Coefficient
D	Pipe diameter
D_{sm}	Sauter mean diameter $\equiv 6a_i/\alpha_g$
\mathbf{g}	Gravitational acceleration
H	Total enthalpy $\equiv h + v'^2/2$
h	Enthalpy
j	Superficial gas/liquid velocity
\mathbf{M}	Generalized interfacial drag
p	Pressure
q	Conduction heat flux
q''	Interfacial heat flux
R	Particle source/sink rate
\bar{u}'_t	Turbulence intensity
\bar{V}	Void-weighted area-averaged velocity
\mathbf{v}	Velocity field
V_r	Relative velocity = $\bar{V}_g - \bar{V}_f$
V_s^*	Ratio of min to max slug volume

Subscript

<i>f</i>	Liquid
<i>g</i>	Gas
<i>i</i>	Interface
<i>ph</i>	Phase change source/sink
<i>RC</i>	Random collision
<i>SI</i>	Surface instability
<i>SO</i>	Shearing-off
<i>TI</i>	Turbulent impact
<i>WE</i>	Wake entrainment

Superscript

<i>c</i>	Heat conduction
HZDR	HZDR reconstruction algorithm
μ	Viscous shear
syn	Synthetic bubble
<i>T</i>	Turbulence related

Abstract

Two-phase flow is ubiquitous in industrial, chemical and thermal plants alike. For analyses of Nuclear Power Plants, the current state-of-the-art model for predicting the behavior of two-phase flows is the two-fluid model. In the two-fluid model, balance equations for mass, momentum and energy are written separately for each phase, and are coupled together through transfer terms that depend on the area of the interface between liquid and gas. Research efforts in the past have been focused on the development of an interfacial area transport equation model (IATE) in order to eliminate the drawbacks of static flow regime maps currently used in best-estimate thermal-hydraulic system codes. The IATE attempts to model the dynamic evolution of the gas/liquid interface by accounting for the different interaction mechanisms (bubble break-up, coalescence and expansion) affecting gaseous phase transport.

The further development and validation of IATE models has been hindered by the lack of adequate experimental databases in regions beyond the bubbly flow regime. At the Helmholtz-Zentrum Dresden-Rossendorf, experiments utilizing wire-mesh sensors have been performed at the TOPFLOW test facility over a wide range of flow conditions, establishing a database of high resolution (in space and time) data covering all flow regimes encountered in vertical flows. The experimental database used in this work includes air-water measurements (at 0.25 MPa) performed at a test section characterized by a 52.3 mm diameter (DN50) vertical pipe with a 16 by 16 wire mesh sensor, and a test section characterized by a 198 mm diameter (DN200) vertical pipe with a 64 by 64 wire mesh sensor operating at 2.5 kHz. The objective of the dissertation is to evaluate and improve current interfacial area transport equation models using the high resolution TOPFLOW database and to assess the uncertainty in the reconstructed interfacial area measured using wire-mesh sensors.

An interfacial area reconstruction algorithm was used to obtain interfacial area concentration measurements from the wire-mesh sensors raw data. The uncertainty of the reconstruction algorithm was systematically evaluated before using the experimental data for the assessment of state-of-the-art IATE models.

The Fu-Ishii model, specifically developed for small-diameter pipes, was assessed against

the TOPFLOW DN50 data. The model was found to perform well (within the experimental uncertainty of $\pm 10\%$) for low void fractions. At high void fractions, the bubble interaction mechanism responsible for the poor performance of the model was identified. A genetic algorithm was then used to quantify the correct incidence of this mechanism on the overall evolution of the interfacial area concentration along the pipe vertical axis. A change in the parameters of the original model was suggested in order to improve the model performance across all applicable databases available in the literature.

The Smith-Schlegel model, specifically developed for large-diameter pipes, was assessed against the TOPFLOW DN200 data. This model was also found to perform well at low void fractions. At high void fractions, the good agreement between the model predictions and the experimental data were found to be due to a compensation of errors. Studies using the genetic algorithm indicated significant performance improvement for the DN200 data. However, the improvement in prediction capabilities could not be reproduced when the model was assessed against independent large-diameter databases available in the literature. Therefore, no quantitative suggestion could be made for the Smith-Schlegel model. As the independent databases were based on measurement techniques not well suited for high void fractions conditions such as churn turbulent flows, a need for additional experimental data remains.

Chapter 1

Introduction

This chapter discusses the relevance of two-phase flow modelling to guaranteeing the safe operation of nuclear power plants. Section 1.2 details the current state-of-the-art two-phase flow models that are used to simulate nuclear power plants. Section 1.2.3 introduces the interfacial area transport equation (IATE), a model anticipated to improve the current state-of-the-art. In Section 1.3 experimental methods typically used to study multiphase flows are presented. A novel high resolution experimental database for two-phase flow in vertical pipes is introduced in Section 1.3.3. Section 1.5 presents a literature review of the previous IATE evaluations. Lastly, Section 1.6 presents the thesis objectives.

1.1 Nuclear Plant Operation

As of 2016, there are 100 operating nuclear plants throughout the US that generate approximately 20% of the baseload US electricity demand. All of them are light-water reactors (LWR), where water is used both as coolant and as neutron moderator for the sustainment of the fission chain reaction. Of the 100 reactors, 65 are Pressurized Water Reactors (PWR) and 35 are Boiling Water Reactors (BWR). Water-cooled reactors are also prevalent in the rest of the world. There are significant operating differences between a BWR and a PWR; however, the aim of both systems is to harness nuclear energy through heating water.

In a BWR, the system operates at a lower pressure (typically 7 MPa) in comparison to a PWR (typically 15 MPa). In a BWR the aim is to generate steam. The steam is routed directly to a turbine which generates electricity. A depiction of the typical flow regimes observed in a BWR is presented in Fig. 1.2. The figure showcases the evolution of the coolant from single-phase flow to two-phase flow in small diameter vertical channels (note that the hydraulic diameter of a typical LWR lattice is in the order of 12 mm). The morphology of the liquid-gas interface becomes increasingly complex as the void fraction increases.

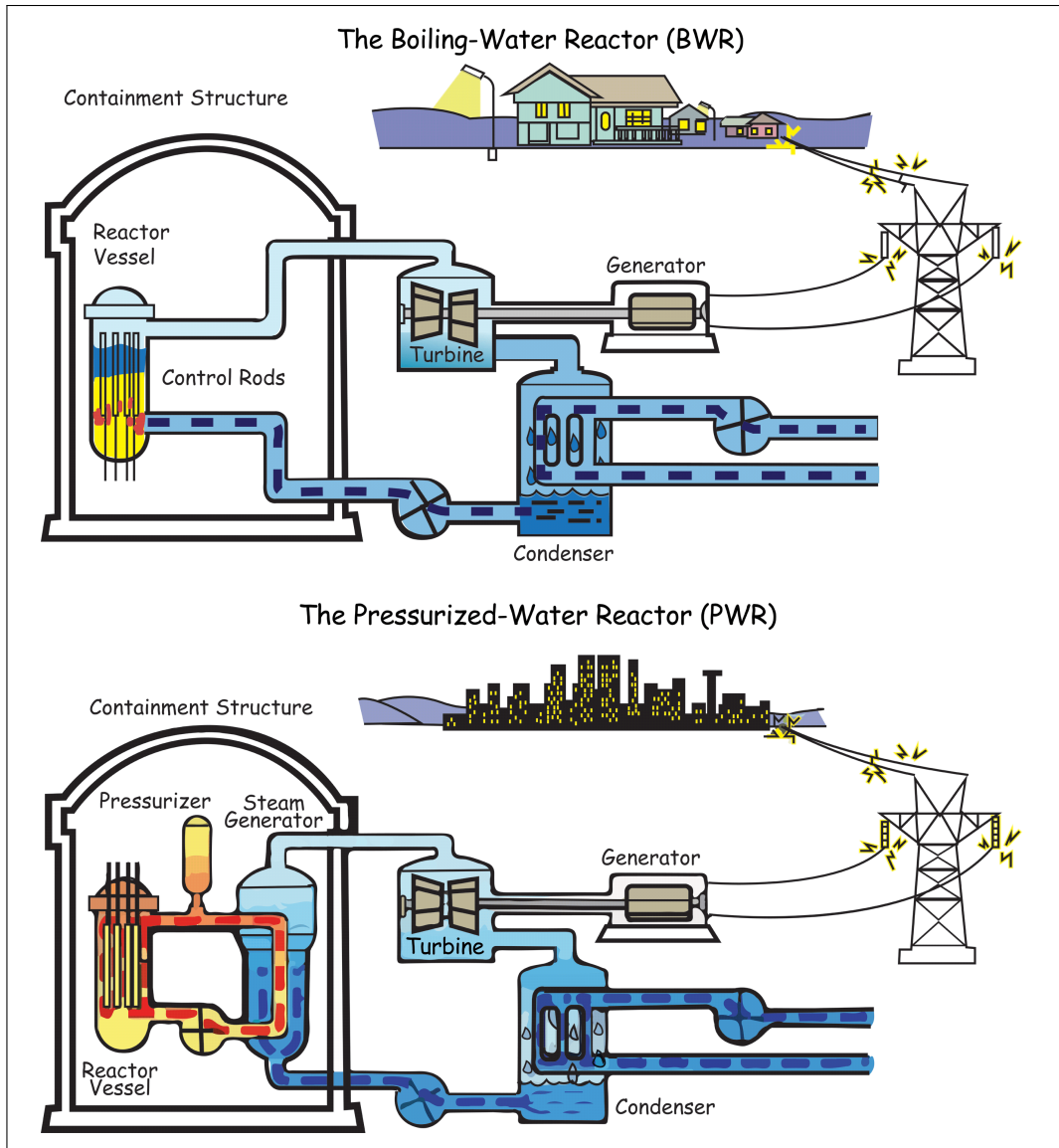


Figure 1.1: Generalized schemes for BWRs and PWRs [1].

Two-phase flow in a PWR is found on the secondary side of the steam generator. It is also observed in the PWR's core during normal operation, as the coolant remains in subcooled boiling conditions (steam bubble are generated at the fuel cladding surface, but the bulk of the fluid remains below saturation). However, steam production in a PWR core might occur during accident conditions, such as a loss-of-coolant accident (LOCA).

In the development and assessment of nuclear reactors, safety is a top priority. In order to determine operating margins for LWRs, accurate simulation of two-phase flow transport phenomena is essential. From a thermal-hydraulics standpoint, accurate predictions of two-phase flow characteristics are necessary to determine heat transfer processes and pressure changes throughout the core. From a neutronics standpoint, accurate predictions of two-

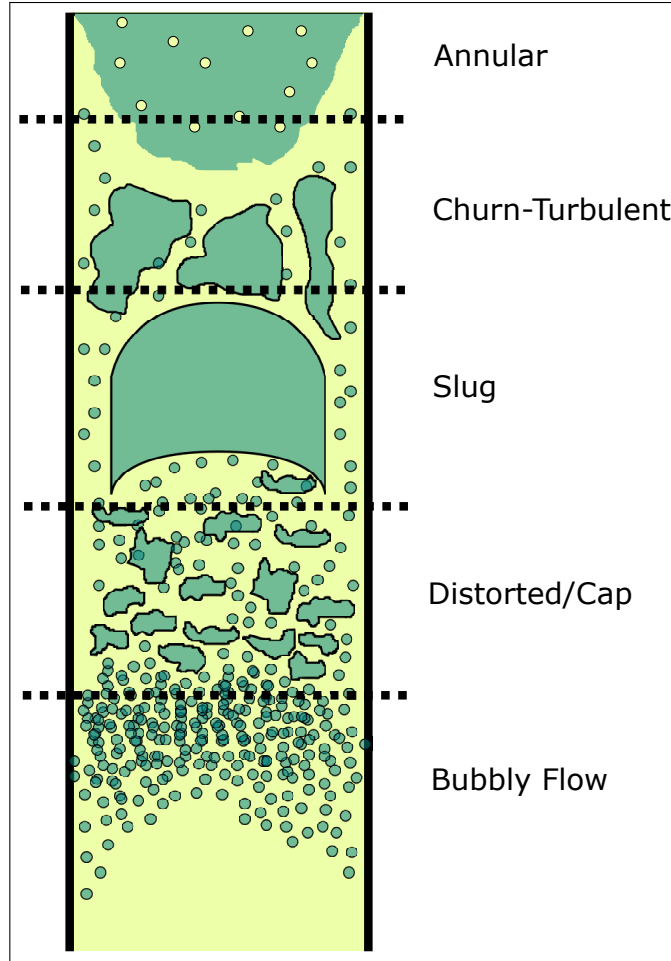


Figure 1.2: Generalized two-phase flow regimes that are typical for a vertical small diameter pipe. The dark green color represents steam, while the light green color represents water. Example of typical flow regimes observed experimentally are presented in Fig. 3.14.

phase flow characteristics are necessary to determine criticality and fuel burn-up. In LWRs a strong coupling exists between thermal-hydraulics and neutronics, as the amount of steam (void fraction) in the core, and the temperature of fuel and coolant affect the power production in the core. Heat transfer between fuel and coolant is strongly affected by the topology of the two-phase flow vapor-liquid interface. The interface topology also affects mass, momentum and energy transfer between the vapor and liquid phase. Modelling approaches for two-phase flows are introduced in Section 1.2.

1.1.1 Application to other plants

The importance of accurate multiphase modelling is not limited to the nuclear plant. Conventional power plants and pharmaceutical plants also experience multiphase transport in

their working fluid. For chemical processes and efficient heat transfer properties, the low void fraction regime has been attractive [64]. In chemical reactions a high interfacial area concentration (defined by Eq. (1.10)) provides greater yields; for heat transfer, nucleate boiling allows high heat transfer rates. High void fraction flows are also found in several industrial applications. Separation of gas and oil in the petrochemical industry occurs in the churn-turbulent flow regime.

1.2 Multiphase Modelling

There are several approaches that have been developed to model two-phase flows. Generally, they vary in complexity in terms of number of transport equations required and closure relationships needed. Greater accuracy is achieved at the cost of complexity. The difficulty in modelling multiple phases arises from the prediction of interactions at the interface. The usefulness of analytical models is poor for treatment of the interface and instead we require semi-empirical correlations. The models discussed hereafter, are numerically solved in one-dimensional system codes. Several high fidelity models exist for CFD-grade applications and are summarized in [63].

The simplest model is the homogeneous equilibrium model (HEM). In HEM, the two separate phases are modelled as a uniform mixture in thermodynamic equilibrium, assuming that pressure, velocity and temperature of the two phases are equal. In this case, only three balance equations (for the mixture mass, velocity and energy) need to be solved. The HEM model can be improved by allowing a relative velocity between the phases to exist (HEM drift flux model). It is important to highlight the assumption that the two-phase mixture is in equilibrium, indicating that such an approach is inappropriate for fast transient phenomena, such as rapid acceleration or pressure changes [12].

A more complete description of two-phase flow is achieved through the two-fluid model, in which mass, energy and momentum balance equations are written separately for each phase, resulting in a total of six transport equations. The two-fluid model is more accurate for transients in which flow conditions are rapidly changing and non-equilibrium exists between the phases. For example, the time lag of energy transfer at the interface may cause a temperature difference between the gas and liquid phase. However, several closure relationships are needed for the interfacial transfer terms, which couple the transport equations.

1.2.1 Two-fluid Model

The two-fluid model [29, 36, 37] is at the basis of so-called best-estimate thermal-hydraulic system codes, widely used for the safety analysis of LWRs. State-of-the-art thermal-hydraulic system codes include RELAP5 [3] and TRACE [2] developed by US NRC, CATHARE [7] developed by CEA in France and ATHLET [44] developed by GRS in Germany. In these codes, three transport equations for mass, momentum and energy are solved for each phase, resulting in a total of six transport equations¹. The equations for each phase are coupled through interface transfer terms for mass, momentum and energy exchange at the gas-liquid interface. The coupling between the gas and liquid to be taken into account in the two-fluid model formulation is schematically depicted in Fig. 1.3. Several constitutive relations are needed to achieve closure of the two-fluid model.

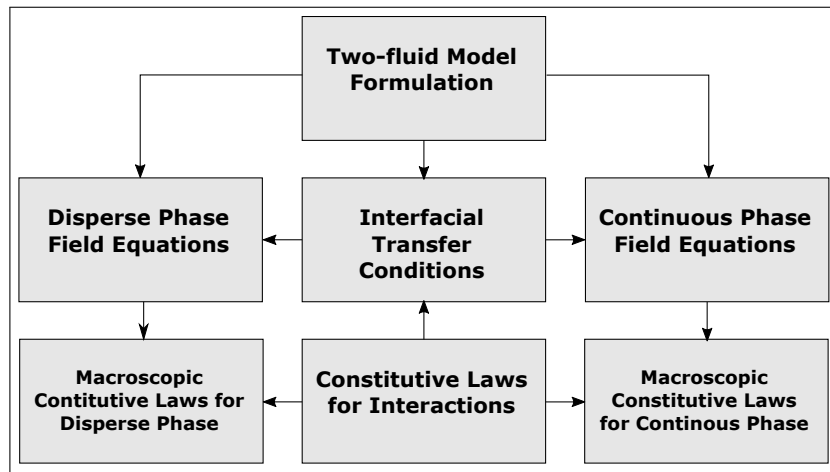


Figure 1.3: Diagram showcasing the dependencies of the two-fluid model [32].

The continuity equation for the gas and liquid phase is represented by Eq. (1.1) and Eq. (1.2) respectively with the interfacial jump condition Eq. (1.3). The conservation of momentum for the gas and liquid phase is represented by Eq. (1.4) and Eq. (1.5), respectively, with the interfacial jump condition Eq. (1.6). The conservation of energy for the gas and liquid phase is represented by Eq. (1.7) and Eq. (1.8), respectively, with the interfacial jump condition Eq. (1.9). In these equations ρ , \mathbf{v} , and H are density, velocity and enthalpy. The void fraction α is defined as the fraction of the flow area occupied by the disperse (gas) phase. In the mass conservation equations, the term Γ represents the source/sink term due to evaporation and condensation. In the momentum equations terms \mathbf{M}_{ik} , \mathbf{v}_{ki} , τ_{ki} , and p_{ki}

¹In general, the transport equations are averaged over the cross-sectional area of flow (see [32, Ch. 3]), resulting in one-dimensional transport equations. The one-dimensional transport equations are solved in system codes.

represent generalized interfacial drag, interfacial velocity, interfacial shear stress and interfacial pressure. In the energy equations terms H_{ki} , q''_{ki} , and ϕ represent interfacial enthalpy, interfacial heat flux and heat dissipation rate. In the following equations, the subscript k is g for gas (g) and f for liquid:

$$\frac{\partial [\alpha \rho_g]}{\partial t} + \nabla \cdot [\alpha \rho_g \mathbf{v}_g] = \Gamma_g , \quad (1.1)$$

$$\frac{\partial [(1 - \alpha) \rho_f]}{\partial t} + \nabla \cdot [(1 - \alpha) \rho_f \mathbf{v}_f] = \Gamma_f , \quad (1.2)$$

$$\Gamma_g + \Gamma_f = 0 , \quad (1.3)$$

$$\begin{aligned} \frac{\partial [\alpha \rho_g \mathbf{v}_g]}{\partial t} + \nabla \cdot [\alpha \rho_g \mathbf{v}_g \mathbf{v}_g] = & - \nabla [\alpha p_g] + \nabla \cdot [\alpha (\boldsymbol{\tau}_g^\mu + \boldsymbol{\tau}_g^T)] + \\ & + \alpha \rho_g \mathbf{g} + \Gamma_g \mathbf{v}_{gi} + \\ & + p_{gi} \nabla \alpha - \nabla \alpha \cdot \boldsymbol{\tau}_{gi} + \mathbf{M}_{ig} , \end{aligned} \quad (1.4)$$

$$\begin{aligned} \frac{\partial [(1 - \alpha) \rho_f \mathbf{v}_f]}{\partial t} + \nabla \cdot [(1 - \alpha) \rho_f \mathbf{v}_f \mathbf{v}_f] = & - \nabla [(1 - \alpha) p_f] + \\ & + \nabla \cdot [(1 - \alpha) (\boldsymbol{\tau}_f^\mu + \boldsymbol{\tau}_f^T)] + \\ & + (1 - \alpha) \rho_f \mathbf{g} + \Gamma_f \mathbf{v}_{fi} + p_{fi} \nabla (1 - \alpha) + \\ & + - \nabla (1 - \alpha) \cdot \boldsymbol{\tau}_{fi} + \mathbf{M}_{if} , \end{aligned} \quad (1.5)$$

$$\mathbf{M}_{ig} + \mathbf{M}_{if} = \mathbf{0} , \quad (1.6)$$

$$\begin{aligned} \frac{\partial [\alpha \rho_g H_g]}{\partial t} + \nabla \cdot [\alpha \rho_g \mathbf{v}_g H_g] = & - \nabla \cdot [\alpha (\mathbf{q}_g^c + \mathbf{q}_g^T)] + \\ & + \frac{D_g [\alpha p_g]}{Dt} + \Gamma_g H_{gi} + a_i q''_{gi} + \\ & + - p_{gi} \frac{D_g \alpha}{Dt} + \xi_g , \end{aligned} \quad (1.7)$$

$$\begin{aligned} \frac{\partial [(1 - \alpha) \rho_f H_f]}{\partial t} + \nabla \cdot [(1 - \alpha) \rho_f \mathbf{v}_f H_f] = & - \nabla \cdot [(1 - \alpha) (\mathbf{q}_f^c + \mathbf{q}_f^T)] + \\ & + \frac{D_f [(1 - \alpha) p_f]}{Dt} + \Gamma_f H_{fi} + a_i q''_{fi} + \\ & + - p_{fi} \frac{D_f (1 - \alpha)}{Dt} + \xi_f , \end{aligned} \quad (1.8)$$

$$(a_i q''_{gi} + \Gamma_g h_{gi}) + (a_i q''_{fi} + \Gamma_f h_{fi}) = 0 . \quad (1.9)$$

The majority of terms on the right-hand-side of the two-fluid model depend on interac-

tions at the interface between the gas and liquid phases. The interfacial area concentration, a_i , is the total surface area between phases per unit mixture volume,

$$a_i = \frac{\text{Interfacial area}}{\text{Mixture volume}} .$$

The constitutive modelling of the two-fluid model interfacial closure terms are out of the scope of this work and are detailed by Ishii [32]. The interfacial interaction terms are generalized by Ishii and Mishima [37] as

$$[\text{Interfacial transfer term}] \propto a_i \cdot [\text{Driving potential}] . \quad (1.10)$$

It is evident that, in order to achieve satisfactory modelling of two-phase flows, an accurate estimation of the interfacial area concentration is necessary. The interfacial area concentration is strongly dependent on the particular flow regime, therefore flow regime characterization as function of flow conditions (gas and liquid velocities, void fraction, etc.) is required as well. With reference to Fig. 1.3, the left and right branches of the model are represented by Eqs. (1.1) to (1.9). The central branch that couples the disperse (gas) phase with the continuous (liquid) phase, ‘Interfacial Transfer Conditions’, and ‘Constitutive Laws for Interactions’ is discussed next.

1.2.2 Regime Map

The current state-of-the-art thermal-hydraulic system codes, such as TRACE V5 [2], use a static regime map in conjunction with closure relationships to determine interfacial transfer terms. Regime maps for pre-critical heat flux and post-critical heat flux used in TRACE are presented in Fig. 1.4 and Fig. 1.5, respectively. A single geometric parameter, the void fraction, determines the regime of the two-phase flow. Once the flow regime is identified for the given flow conditions, algebraic correlations (closure relations) are used to determine the associated interfacial area concentration.

In order to demonstrate how the static regime maps are utilized within a best-estimate thermal-hydraulic system code (specifically, TRACE V5 [2]), the process for calculating the interfacial drag force per unit volume, M_i''' , is discussed. The drag force can be calculated by Eq. (1.11), where C_i is the interfacial drag coefficient and V_r is the relative velocity. The coefficient C_i will depend on the regime selected within pre-CHF or post-CHF maps (a stratified flow map also exists for horizontal pipes). M_i''' is given by

$$M_i''' = C_i V_r |V_r| . \quad (1.11)$$

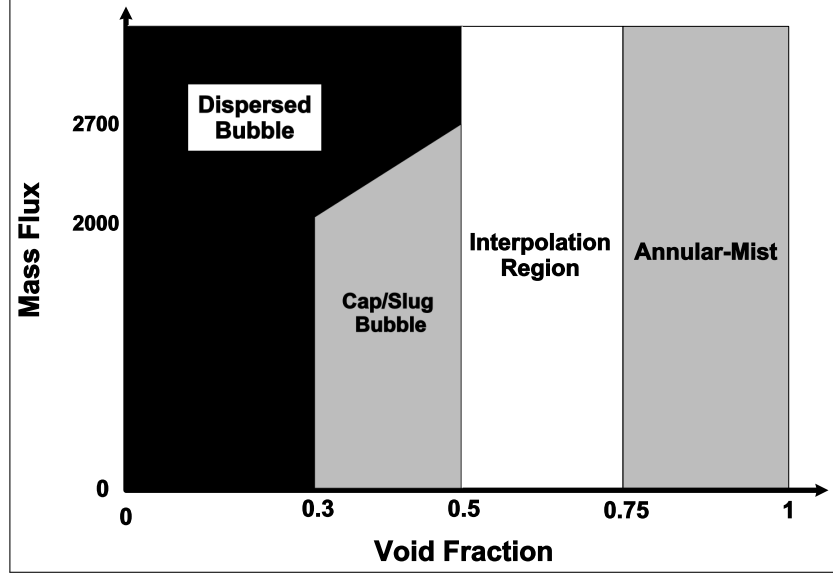


Figure 1.4: Example of pre-CHF flow regime map used by TRACE V5 [2].

For bubbly flow, the coefficient C_i is defined by Eq. (1.12), where v_{gj} is the drift flux velocity and P_s is a profile slip factor. Two parameters need to be specified in this case, v_{gj} and a distribution coefficient, C_0 (see Eq. (1.14)):

$$C_i = \frac{\alpha(1 - \alpha)^3 g \Delta \rho}{\bar{v}_{gj}^2} \cdot P_s, \quad (1.12)$$

$$P_s = \left(\frac{1 - C_0 \langle \alpha \rangle}{1 - \langle \alpha \rangle} \bar{V}_g - C_0 \bar{V}_l \right)^2 \frac{1}{V_r^2}, \quad (1.13)$$

$$C_0 = 1.2 - 0.2 \sqrt{\frac{\rho_g}{\rho_f}}. \quad (1.14)$$

The drift flux correlation for bubbly flows [30] is given by Eq. (1.15). The drift flux correlation for cap/slug flows [28] is given by Eq. (1.16), (where $N_{\mu f}$ is the liquid viscosity number). The drift flux for a transition from bubbly to slug flow regime is given by Eq. (1.18) where f_{CT} is a simple linear ramp that is function of the void fraction:

$$\bar{v}_{gj} = \sqrt{2} \left(\frac{\sigma g \Delta \rho}{\rho_f^2} \right)^{(1/4)}, \quad (1.15)$$

$$\bar{v}_{gj} = \left(0.0019 \left[\frac{D_h}{\sqrt{\sigma/g\Delta\rho}} \right]^{0.809} \left[\frac{\rho_g}{\rho_f} \right]^{-0.157} [N_{\mu f}]^{-0.562} \right) \left(\frac{\sigma g \Delta \rho}{\rho_f^2} \right)^{(1/4)}, \quad (1.16)$$

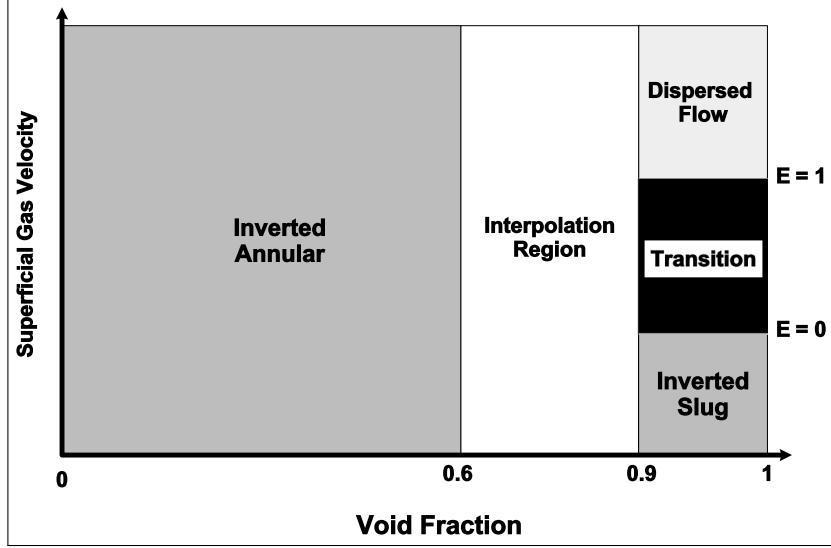


Figure 1.5: Example of post-CHF flow regime map used by TRACE V5 [2].

$$N_{\mu f} = \frac{\mu_f}{\sqrt{\rho_f \sigma \sqrt{\sigma / g \Delta \rho}}}, \quad (1.17)$$

$$\bar{v}_{gj} = f_{CT}(\bar{v}_{gj})_{\text{bubbly}} + (1 - f_{CT})(\bar{v}_{gj})_{\text{slug}} \text{ for } 0.2 \leq \alpha \leq 0.3, \quad (1.18)$$

$$f_{CT} = \frac{0.3 - \alpha}{0.3 - 0.2}. \quad (1.19)$$

The above correlations have been developed specifically for bubbly flows. The specific formulation of closure relationships will depend on the particular flow regime. The method of static flow regime maps and corresponding empirically determined constitutive relations present several drawbacks [32, Ch. 11]:

1. The flow-regime transition criteria are algebraic relations developed for steady-state fully-developed flows. Any dynamic evolution of the interfacial structure cannot be properly captured, e.g. entrance effects, downstream flow development, and transitioning between flow regimes.
2. The solution methodology requires both transition criteria and closure relationships depending on flow configurations, introducing the possibility of compounding two errors.
3. The closure relationships have parameters that have been developed through simple air–water experiments that are valid for specific operational conditions and geometries. When applied to high pressure steam–water transients these models may cause significant discrepancies, discontinuities and numerical instability.

In order to address these shortcomings, research efforts have been focused on the development of interfacial area transport equation (IATE) models. The model was originally proposed by Kocamustafaogullari and Ishii in 1995 [42]. Following the initial proposal, a one-group formulation was proposed by Wu in 1998 [82]. In 2001 a two-group model was proposed by Hibiki and Ishii [26], followed in 2003 by a more advanced two-group model by Fu and Ishii [22]. The differences between one-group and two-group models will be discussed in Section 3.1. In the following section, the derivation of the one-group transport equations will be provided and its differences and potential benefits with respect to the static flow regime map approach will be discussed.

1.2.3 Interfacial area transport equation

The derivation of the interfacial area transport equations starts with the one-dimensional Boltzmann transport equation. Bubble ‘particles’ are considered within a continuous medium (i.e. the liquid phase), and are described by the distribution $f(V, x, v, t)$. This is defined as the particle number density function per unit mixture and bubble volume (units of $1/\text{length}^6$), where V is the volume of the bubble, x is the position in the continuum, v is the velocity, at time t . The distribution $f(V, x, v, t)$ is assumed to be continuous. It is further assumed that the change of velocity between the time interval t and $t + \delta t$ is sufficiently small such that the distribution simplifies to $f(V, x, t)$. Eq. (1.20) can be written to express a differential change in particle distribution.

$$f(V + \delta V, x + \delta x, t + \delta t) = \left(\sum_j S_j + S_{ph} \right) \delta \mu \delta t \quad (1.20)$$

The left-hand side of Eq. (1.20) is expanded in a Taylor series about δt and then the equation is divided by $\delta \mu \delta t$ to form Eq. (1.21) (where $\delta \mu$ is a finite volume in space). In order to obtain the interfacial area transport equation, Eq. (1.21) is multiplied by the surface area of bubble particles of volume V , $A_i(V)$, and then integrated over the volume of all particles, resulting in Eq. (1.22). In this context, the definition of interfacial area concentration, volumetric gas fraction and interfacial velocity are Eqs. (1.23) to (1.25), respectively:

$$\frac{\partial f}{\partial t} + \nabla \cdot (fv) + \frac{\partial}{\partial V} \left(f \frac{dV}{dt} \right) = \sum_j S_j + S_{ph} , \quad (1.21)$$

$$\frac{\partial a_i}{\partial t} + \nabla \cdot (a_i v_i) + \left(\frac{\dot{V}}{V} \right) \int_{V_{min}}^{V_{max}} f V dA_i = \int_{V_{min}}^{V_{max}} \left(\sum_j S_j + S_{ph} \right) A_i dV , \quad (1.22)$$

$$a_i(x, t) \equiv \int_{V_{min}}^{V_{max}} f(V, x, t) A_i(V) dV , \quad (1.23)$$

$$\alpha_g(x, t) \equiv \int_{V_{min}}^{V_{max}} f(V, x, t) V dV , \quad (1.24)$$

$$v_i(x, t) \equiv \frac{\int_{V_{min}}^{V_{max}} f(V, x, t) A_i(V) v(V, x, t) dV}{\int_{V_{min}}^{V_{max}} f(V, x, t) A_i(V) dV} . \quad (1.25)$$

The third term on the left-hand side of Eq. (1.22) can be simplified further. The volumetric source term \dot{V}/V in Eq. (1.22) is defined as

$$\frac{\dot{V}}{V} = \frac{1}{V} \frac{dV}{dt} = \frac{1}{\alpha_g} \left(\frac{\partial \alpha_g}{\partial t} + \nabla \cdot (\alpha_g v_g) - \eta_{ph} \right) . \quad (1.26)$$

The integral of fV over the surface area of the particles is converted into an integral over the particles' volume,

$$\frac{V_{sphere}}{A_{sphere}} = \frac{\frac{4}{3}\pi \left(\frac{D}{2}\right)^3}{4\pi \left(\frac{D}{2}\right)^2} = \frac{1}{3} \left(\frac{D}{2}\right) , \quad (1.27)$$

$$\int_{V_{min}}^{V_{max}} fV dA_i = \int_{V_{min}}^{V_{max}} f \frac{1}{3} \left(\frac{D}{2}\right) \frac{4}{D} A_i dV = \frac{2}{3} \int_{V_{min}}^{V_{max}} f A_i dV = \frac{2}{3} a_i . \quad (1.28)$$

It is important to note that in this transformation, the bubbles are assumed to be spherical. While this is a good approximation for disperse bubbly flow, it is invalid for slug, distorted, churn-turbulent or annular flow.

The terms on the right-hand side of Eq. (1.22) represent source/sink terms due to bubbles interaction mechanisms which are responsible for changes in interfacial area density. The definition of the particle source and sink rate is given by

$$\int_{V_{min}}^{V_{max}} \sum_j S_j dV = \sum_j R_j = \text{particle source and sink rate}, \quad (1.29)$$

from which the source and sink rates for the interfacial area density can be defined,

$$\int_{V_{min}}^{V_{max}} \sum_j S_j A_i dV = \sum_j \phi_j = a_i \text{ source and sink rate}. \quad (1.30)$$

Substitution of Eqs. (1.23) to (1.26), (1.28) and (1.30) to Eq. (1.21) results in the one-group

interfacial area transport equation (IATE),

$$\frac{\partial a_i}{\partial t} + \nabla \cdot (a_i v_i) - \frac{2}{3} \left(\frac{a_i}{\alpha_g} \right) \left(\frac{\partial \alpha_g}{\partial t} + \nabla \cdot (\alpha_g v_g) - \eta_{ph} \right) = \sum_j \phi_j + \phi_{ph} . \quad (1.31)$$

There are significant differences between the IATE formulation and the approach based on static flow regime maps (Section 1.2.2). In the IATE formulation, a transport equation accounts for the evolution of the interfacial area density in time and space, while flow regime maps relies on algebraic correlations. There is no direct dependence of the transport equations on the particular flow regime (i.e. bubbly flow, slug flow, etc.); the model relies instead on the specification of bubble interaction mechanisms, ϕ_j .

1.2.3.1 Interaction mechanisms

The interaction mechanisms that are accounted for in the interfacial area transport equation model can be separated into two major categories: coalescence mechanisms and breakup mechanisms (see Fig. 1.6 for a schematic illustration). The mechanistic modeling of these interactions is detailed in Section 3.1.1.

- Coalescence mechanisms occur when two bubbles merge together, forming a larger bubble. These interactions generally constitute a sink for the interfacial area concentration, as the surface area to volume ratio decreases.
 - Random collision: occurs due to random movements of bubbles in the flow driven by turbulent eddies, causing two bubbles to collide and possibly coalesce.
 - Wake entrainment: occurs when a bubble enters the wake region of a leading bubble. The trailing bubble may accelerate and collide with the leading bubble, resulting in coalescence.
- Breakup mechanisms occur when a bubble breaks into smaller structures: these interactions generally constitutes a sink for the interfacial area concentration, as the surface area to volume ratio increases.
 - Turbulent impact: this is a disintegration mechanism that occurs when turbulent eddies in the flow impact a bubble. If the impact is strong enough to overcome surface tension, the bubble will break-up.
 - Shearing-off: this is a complex mechanism that occurs for large bubbles presenting a skirt at their base. The disruptive viscous forces pulling at the skirt overcome the cohesive surface tension, causing formation of small bubbles.

- Surface instability: this occurs when a bubble grows and reaches a limit at which the leading interface can no longer be sustained because of turbulence-induced instabilities. The instability propagates through the bubble surface, ultimately causing the bubble breakup.

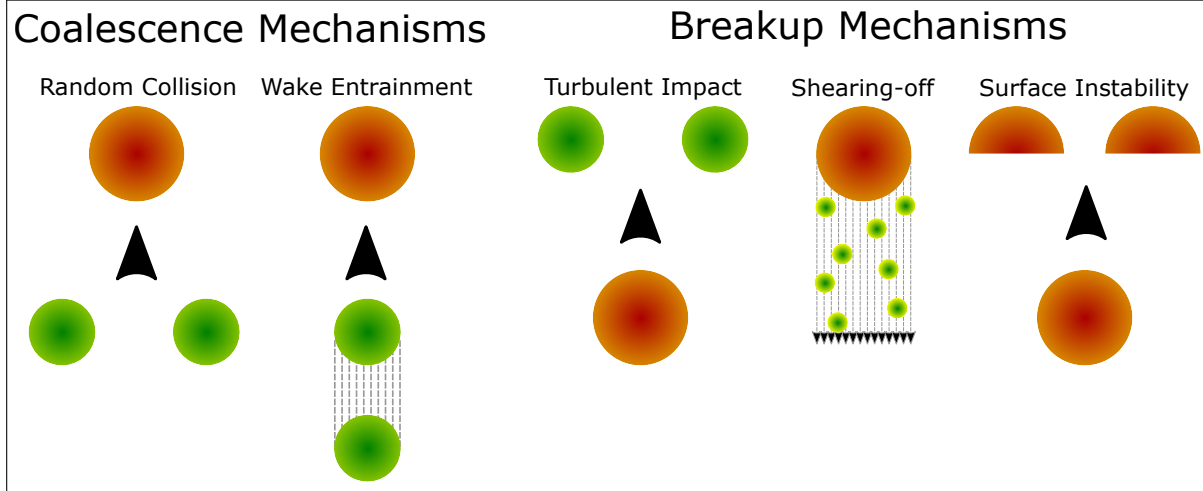


Figure 1.6: An overview of bubble interaction mechanisms that are considered by the interfacial area transport equation model. Vertical orientation indicates the upstream position of the bubbles during the interaction. Color indicates relative expected bubble size.

Recent detailed reviews on bubble break-up and coalescence mechanisms have been published by Lao and Lucas (see [45] and [46], respectively). The most recent review on bubble break-up and coalescence mechanisms relevant for the churn turbulent flow regime has been published by Montoya and co-workers [53].

1.2.3.2 Expected improvement

The interfacial area transport equation aims at addressing the drawbacks of the static nature of flow regime maps (Section 1.2.2). As expressed by Eq. (1.10), mass, momentum and energy transfers at the interface between liquid and gas are related to the interfacial area concentration and to local transfer mechanisms (e.g. the degree of turbulence near the interfaces, heat transfer between interface and the gas and liquid phases, etc.). The interfacial area concentration, defined as the interfacial area per unit volume of the mixture, is expected to characterize the *kinematic effects* related to the structure of the two-phase flow. The driving forces for the inter-phase transport characterize the *local transport* mechanism and are modelled independently. As the interfacial transfer term is considered proportional to the product of the interfacial flux and the available interfacial area, an accurate modelling of the interfacial area concentration is essential [32, Ch. 11].

In two-phase flow, the void fraction and the interfacial area concentration represent fundamental first-order geometrical parameters characterizing the gas-liquid interface. Therefore, they are closely related to two-phase flow regimes (Fig. 1.2). However, the concept of flow regimes is difficult to quantify mathematically at a local point, because it is often defined close to the system scale. This indicates a necessity for the modelling of the changes of the interfacial area concentration directly by a transport equation – leading to the development of the interfacial area transport equation model [32, Ch. 11]. Therefore, the model is expected to outperform the conventional regime map which relies on transition criteria and regime-dependent constitutive relations for interfacial area concentration.

1.3 Experimental Methods

Several experimental methods have been developed to understand and measure two-phase flows to support the development of models. There are two major categories of experimental methods: intrusive and non-intrusive methods. Intrusive methods are those in which the flow is disrupted by the presence of a detector or obstruction. Non-intrusive methods are those in which external detectors are used and have negligible impact on the flow.

1.3.1 X-ray and γ -ray tomography

Non-intrusive measurement techniques that can be used to characterize two-phase flows include X-ray and γ -ray tomography (refer to [69] and [43], respectively). A literature review of tomography and high speed camera experimental databases available for the interfacial area concentration measurements during subcooled boiling is given by Bartel [5].

γ -ray tomography

An example of a γ -ray tomograph is presented in Fig. 1.7. The large delay in measurement renders this method inappropriate for non-stationary measurements. In order to improve the temporal resolution, the complexity and cost of these methods significantly increase [21].

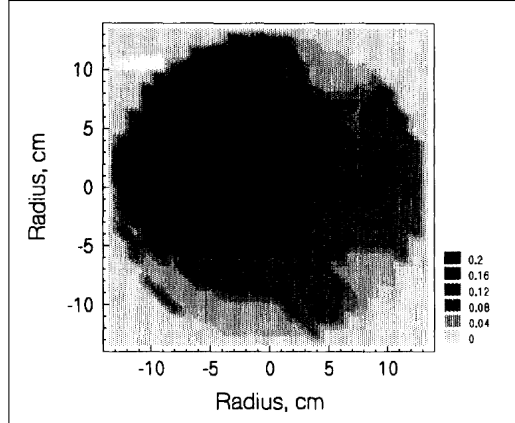


Figure 1.7: A γ -ray tomograph indicating void fraction distribution for a 26.35 cm pipe with $v_g = 5.0$ m/s [43].

Fast X-ray tomography

Fast X-ray tomography has been developed to capture frames at 1 kHz [9]. An example of a slug bubble reconstruction using fast X-ray tomographs is presented in Fig. 1.8. Note that the bubble is fairly isolated. Due to the fact that X-ray sources emit a continuous spectra, the reconstruction suffers from so-called beam hardening effects that preclude applicability to more complex flows.

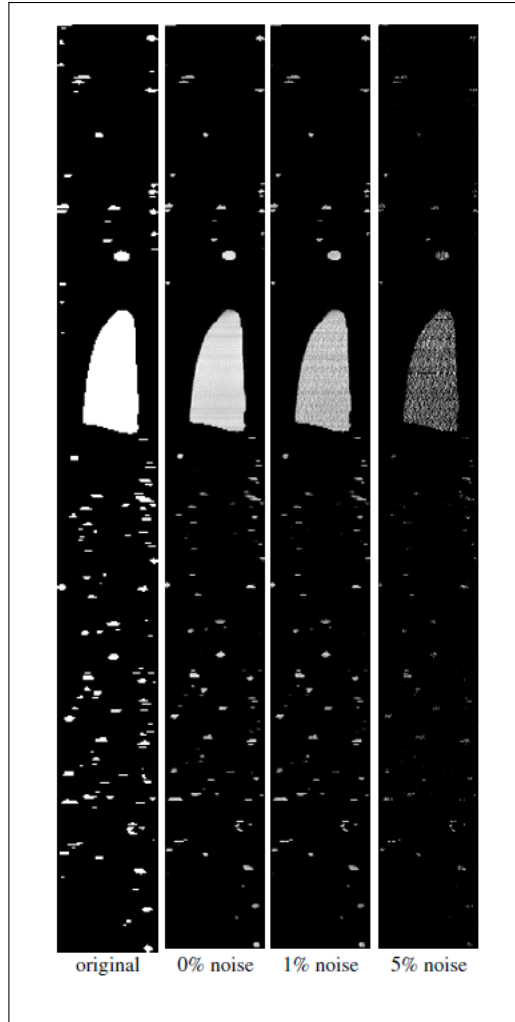


Figure 1.8: Slices of a reconstructed image for a single slug bubble with artificial noise [9].

1.3.2 Needle probe sensor

A widely used (intrusive) measurement technique to measure two-phase flow parameters is the needle probe sensor. Originally proposed by Neal and Bankoff [54], these sensors are used to measure the time-averaged local void fraction on the basis of local conductivity (conductivity needle probes) or optical properties of the gas/liquid phases (optical probes). Several designs have been proposed for this type of sensor: a two-sensor probe [81], a four-sensor probe [40], and a five-sensor probe [18] respectively. A double sensor probe allows the measurement of the interface velocity in addition to the local void-fraction. This type of sensor is mostly suitable for bubbly flows. Four- and five-sensor probes can be also applied to more complex high-void fraction conditions. They allow for the measurement of the inclination angle of the liquid-gas interface, which can be used for a direct measurement of

the interfacial area density. Diagrams of a double-sensor and a four-sensor probe are shown in Fig. 1.9.

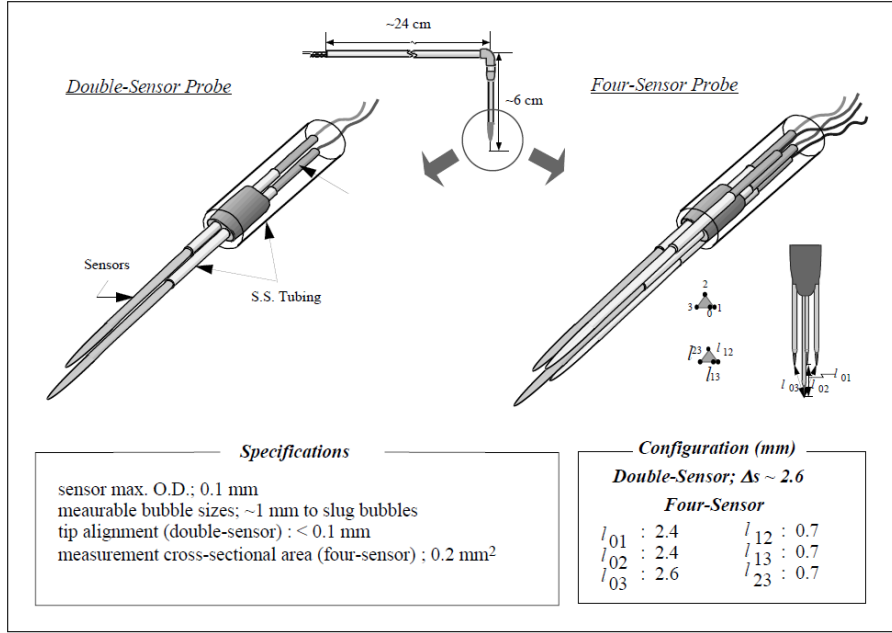


Figure 1.9: Diagram of double-sensor and four-sensor conductivity probes with typical dimensions [39]. The conductivity probes are an intrusive measurement technique.

Since the tip of a probe records the passage of a liquid-gas interface, when a multiple-tipped probe is used, the same interface will be recorded by multiple tips. By analyzing the time delay in the recorded signals, and knowing the distance between the tips, the interfacial velocity can be measured. If the bubbles in the flow can be assumed to be spherical, an average orientation angle can be determined as well. For a four-sensor probe, no such assumption is necessary, as multiple measurements downstream allow the orientation to be deduced. Using the interfacial velocity (\mathbf{v}_i), interfacial orientation (\mathbf{n}_i), and measurement time (ΔT), the interfacial area concentration is indirectly determined by

$$a_i = \frac{1}{\Delta T} \sum_j \left(\frac{1}{|\mathbf{v}_i \cdot \mathbf{n}_i|} \right) . \quad (1.32)$$

Conductivity probes can operate from 10 kHz to 30 kHz. The high acquisition frequency is needed to be able to detect the passage of a liquid-gas interface with sufficient time resolution to be able to measure the interface velocity. Needle-probes measurement need to be ensemble in time in order to achieve sufficient counting statistics (of individual bubbles) and be able to measure local void-fraction, gas velocity and interfacial area concentration. A single measurement takes typically in the range of 30 minutes. If a radial profile of the two-phase

characteristics (e.g. void fraction, interfacial area concentration, etc.) is needed, the sensor need to be transposed radially increasing considerable the necessary measurement time. When several axial locations are needed (essential for validation of any model evaluating interfacial area propagation), and several operating conditions are considered – the relatively long measurement times become a significant disadvantage of this measurement technique.

1.3.3 Wire-mesh sensor

Wire-mesh sensors (WMS) consist of two planes of parallel electrodes (typically 0.01 mm to 0.05 mm diameter wires) arranged perpendicular to each other, typically at an axial distance of 1.0 mm (a CAD is presented in Fig. 1.10). One plane of electrodes is used as the transmitter and the other as the receiver. At the crossing point between each set of wires, the instantaneous local fluid conductivity is measured, which is then converted into a local instantaneous void-fraction using a calibration procedure. Typical sensors range from 16-

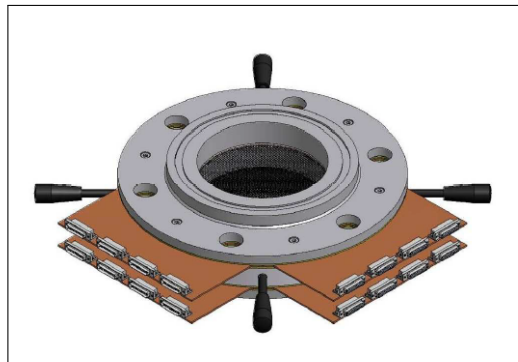


Figure 1.10: CAD of a wire-mesh sensor assembly that is placed into the vertical test section of the TOPFLOW DN200 assembly [8].

by-16 up to 128-by-128 electrodes for a total number of simultaneous measurement locations ranging from 256 to 16,384. This type of sensor allows for up to 10,000 images/s, resulting in high-resolution (both in time and space) void-fraction measurements. In three-layer wire-mesh sensors, a transmitter electrode plane is placed in between two receiver planes, allowing for the simultaneous measurement of the void-fraction distribution in two cross-section. In this way, using cross-correlation or bubble tracking techniques, a bubble’s velocity can be measured as well. Once the bubble velocity is available, a full three-dimensional reconstruction of the two-phase flow passing through the wire-mesh cross-section can be achieved. Examples of the measurement capabilities of a WMS are presented in Fig. 1.11. Details on how the wire-mesh sensor data can be used to extract distribution of the interfacial area concentration will be given in Chapter 2.

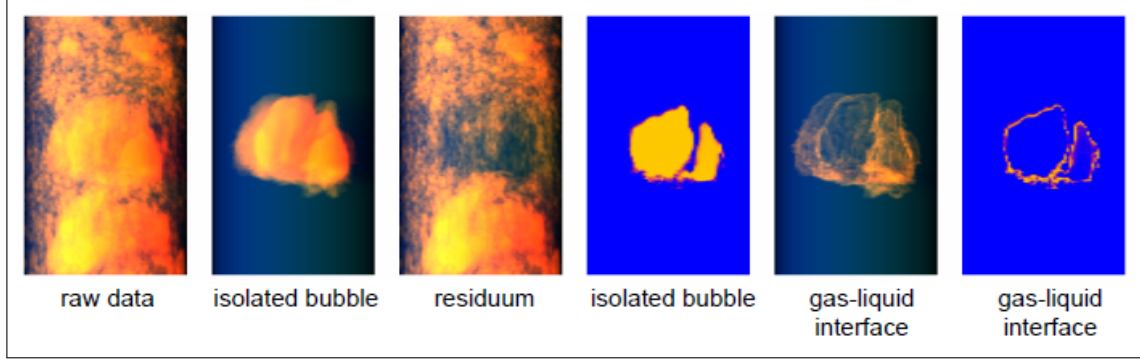


Figure 1.11: Examples of the high resolution capabilities of the wire-mesh sensor. Post processing methods can be used to carefully study the interfacial structure of complicated bubble structures [60].

Several studies have focused on the comparison between WMS and non-intrusive methods such as: high-speed camera [62], ultra-fast X-ray tomography [61, 83], and gamma densitometry [57, 49, 47, 70]. Comparisons with high-speed camera has shown that in case of air-water flows, WMS have a significant effect on the flow structure downstream of the sensor (bubbles are cut by the WMS electrodes), but the WMS signal is representative of the undisturbed flow. An example of such a comparison with X-ray tomography is presented in Fig. 1.12. The effect on the bubble shape disappears with decreasing surface tensions, as observed in applications involving steam-water flows [49, 47].

The quantitative comparisons between WMS and time-resolved X-ray tomography have shown good agreement for the measurement of both void fraction and gas velocity profiles. Good agreement with the void-fraction obtained with gamma densitometry has also been found. Quantitative studies of the impact of WMS in case of air-water mixtures at atmospheric pressure [80] indicate significant changes to the velocity profile downstream of the sensor particularly at low gas velocities. However, comparisons with ultra-fast X-ray tomography [61] have demonstrated that the velocity and void fraction profiles measured by the WMS is that of the undisturbed flow.

A comparison of WMS measurements to needle probe sensors has also been conducted by Manera [48]. The devices had good agreement (in measurement of a_i) at low void-fraction conditions, but appreciable disagreement was observed at higher void fractions. Fig. 1.13 exemplifies the discrepancy. For smaller bubbles ($D_b \leq 10$ mm), there is good agreement between WMS and the needle probe sensor. For higher void fraction, there is a large discrepancy towards the center of the pipe (larger bubbles/slugs aggregate towards the center of the pipe for small diameter pipes), where the measurement of the needle probe exhibits erratic behavior, probably due to the lack of sufficient counts (i.e. poor statistics).

The comparison of WMS with other experimental instruments indicate that while the

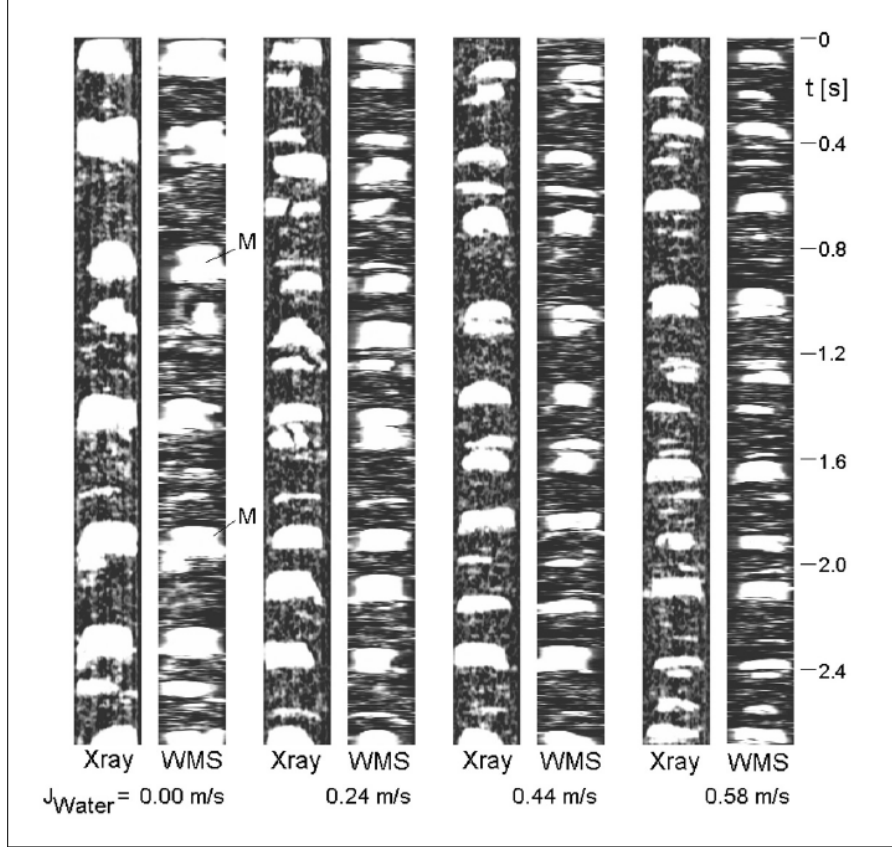


Figure 1.12: A comparison of void fraction distributions measured with X-ray tomography and wire-mesh sensor for $j_g = 0.3 \text{ m/s}$ [61].

WMS is intrusive, the measurement of void fraction distributions is accurate. Furthermore, the WMS provides several benefits. Since data is acquired at a high spatial resolution and high frequency, the duration of the experiments is significantly reduced. Approximately 10 s is required for the measurement at a given axial location (separate radial measurements, like the needle probe are not required). The WMS can easily operate at any orientation (horizontal or vertical). To summarize, there are qualitative benefits that the WMS provides: the acquired data allows for a full reconstruction of the two-phase flow passing through the sensor, and therefore three-dimensional visualization of the flow can be achieved. Lastly, the independence of WMS operation from the orientation of the liquid-gas interface is invaluable as it allows data to be measured in any flow regime.

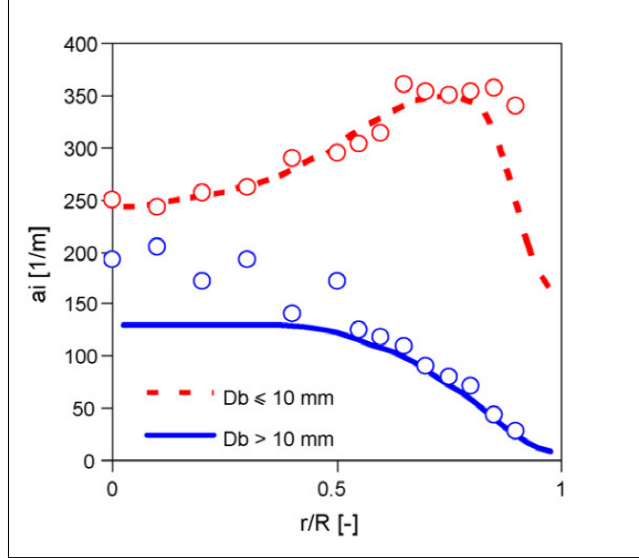


Figure 1.13: A comparison of interfacial area concentration measurements using wire-mesh sensor (continuous) and needle probe for $j_g = 2.1$ m/s and $j_f = 2.6$ m/s in a vertical 50.8 mm pipe [48]. The data is separated by bubble diameter.

1.4 Experimental Database

The development of interfacial area transport equation models involves mechanistic modelling of the interaction mechanisms (ϕ_j in Eq. (1.31)). Expressions for the interaction mechanisms are generally a function of several field variables (e.g. void fraction, gas phase velocity, etc.). The impact of a particular mechanism on the evolution of the interfacial area concentration in space and time is adjusted by means of multiplying coefficients that need to be empirically determined. The development of the IATE model requires an extensive experimental database. The databases that have been published in the literature for vertical-upward small and large diameter pipes are presented in Tables 1.1 and 1.2, respectively. All existing IATE models have been developed on the basis of experimental database using needle probe sensors. Both Fu-Ishii and Smith-Schlegel models (IATE models that are evaluated in Chapter 3) had evaluated their coefficients using a database obtained with the needle probe sensor. In order to validate both models, it is important to assess their performance against an external database using an alternative experimental method (i.e. wire-mesh sensors).

As discussed previously (in Section 1.3.3), the wire-mesh sensors perform on par with needle probes at low void fractions and outperform the needle-probes at high void fraction conditions. Qualitative benefits provided by the wire-mesh sensor have also been discussed previously. There are other benefits provided by the wire-mesh sensor *databases* that can

Table 1.1: Summary of existing experimental database suitable for vertical small diameter interfacial area transport equation development. Regimes: (1) bubbly, (2) slug, (3) churn-turbulent, (4) annular.

Database	Sensor	Diameter [mm]	Tests	Measurement L/D	Regimes
Ishii [34]	Needle probe	12.7	9	17, 120, 217	(1)
Fu [23]	Needle probe	48.3	19	5, 30, 55	(1), (2)
Prasser [60]	Wire-mesh	52.3	37	2, 31, 59, 151	(1), (2)

Table 1.2: Summary of existing experimental database suitable for vertical large diameter interfacial area transport equation development. Regimes: (1) bubbly, (2) cap-turbulent, (3) churn-turbulent, (4) annular.

Database	Sensor	Diameter [mm]	Tests	Measurement L/D	Regimes
Sun [78]	Needle probe	102	5	3, 18, 33	(1)
Smith [75]	Needle probe	102	19	5, 20, 30	(1), (2), (3)
Smith [75]	Needle probe	152	12	5, 20, 30	(1), (2)
Shen [71]	Needle probe	200	5	11, 57	(1)
Beyer [8]	Wire-mesh	198	48	1, 3, 7, 13, 23, 39	(1), (2), (3), (4)

be noted upon further inspection of Tables 1.1 and 1.2, in comparison to their needle probe counterparts. First, there are significantly more tests that have been conducted. Also, the experiments adopted a structured test matrix (Tables 3.2 and 3.3), allowing analysis of incremental changes in either superficial gas or superficial liquid velocity (while keeping the other constant). Secondly, there are more axial measurement locations, which allows a better assessment of the qualitative prediction of interfacial area. Lastly, the database covers both low and high void fraction regimes (and also annular flows in the case of the larger diameter pipe). The experiments using wire-mesh sensors conducted by Prasser and Beyer are discussed in Sections 3.2.1 and 3.2.2, respectively.

1.5 Previous Evaluations

Initially, the Fu-Ishii two-group (2G) model was evaluated with air-water experiments for a vertical 48.3 mm diameter² pipe [23]. The coefficients for group-1 were consistent with those of the one-group IATE model [82]. New group-2 coefficients were determined. The measured bubble velocities were used for the IATE calculations. The experimental data on local void-fraction, bubble velocity and interfacial area were measured using four-sensor conductivity probes at 5, 30 and 55 L/D. The experiments covered the bubbly, slug and churn-turbulent flow regime. Across the three flow regimes, the average error of the Fu-Ishii

²Database of Fu, 48.3 mm in Table 1.1

2G IATE model for the prediction of interfacial area concentration was found to be 10%, 15% and 11%, respectively.

In an attempt to improve the predictive capability of the 6-equation two-fluid model, the IATE model has been implemented in a development branch of the best-estimate thermal-hydraulics system code TRACE, developed by the US Nuclear Regulatory Commission. Initially, the one-group (1G) IATE model was implemented by Talley [79] in TRACE v4.291b. The experimental dataset contained bubbly flow regime air-water experiments for 25.4 mm and 48.3 mm diameter vertical pipes. The study concluded that the 1G IATE improved the prediction of a_i in TRACE from an average of $\pm 48\%$ to $\pm 8\%$. The 2G IATE model was implemented in TRACE v5.0p3 by Bernard [6]. The performance was validated against air-water experiments for the same 48.3 mm diameter pipe. Since the two-group model is implemented, the study evaluated bubbly and slug flow regime. The study concluded that the 2G IATE improved the prediction of a_i in TRACE from an average of $\pm 42\%$ to $\pm 19\%$ for all tests. For bubbly flow the average error was $\pm 10\%$, which is similar to the error cited in the 1G IATE TRACE study by Talley. However, Bernard’s study noted that the prediction of a_i in the churn-turbulent flow and high void fraction regimes remained challenging.

The performance of the 1G Fu-Ishii IATE model was evaluated by Sun [78] against air-water flow data recorded for a larger 101.6 mm diameter³ pipe. Sun concluded that a two-group approach was essential to adequately account for bubble interactions in larger diameter pipes. In order to develop a mechanistic IATE model for large diameter pipes, a larger experimental database was required. The Smith-Schlegel mechanistic model was evaluated against 102 mm and 152 mm diameter⁴ pipes with average interfacial area concentration error of 10.2% and 6.5%, respectively. Smith concluded that further work was necessary to model bubble-induced two-phase turbulence in larger diameter pipes and that *additional data* in pipes larger than 152 mm should be evaluated.

³Database of Smith, 102 mm in Table 1.2

⁴Database of Smith, 152 mm in Table 1.2

1.6 Objectives

The aim of this dissertation is to **evaluate and improve current interfacial area transport equation models using a high resolution database**. The new contributions are:

- Assessing the uncertainty in the reconstruction of interfacial area from wire-mesh sensors data,
- Assessing the performance of current IATE models against the novel high-resolution database based on wire-mesh sensor measurements,
- Exploring the use of generic algorithms to improve the performance of current IATE models across all experimental databases available in the literature.

1.6.1 Outline

The organization of the dissertation is presented in Fig. 1.14. As reconstruction algorithms are needed to extract interfacial area concentration from the wire-mesh sensor raw data, efforts in the present dissertation have been dedicated to the evaluation of the accuracy of such algorithms. A systematic evaluation of the error introduced by the interfacial reconstruction algorithm is presented in **Chapter 2**. The implementation of a convex hull algorithm for the surface reconstruction has been investigated as well.

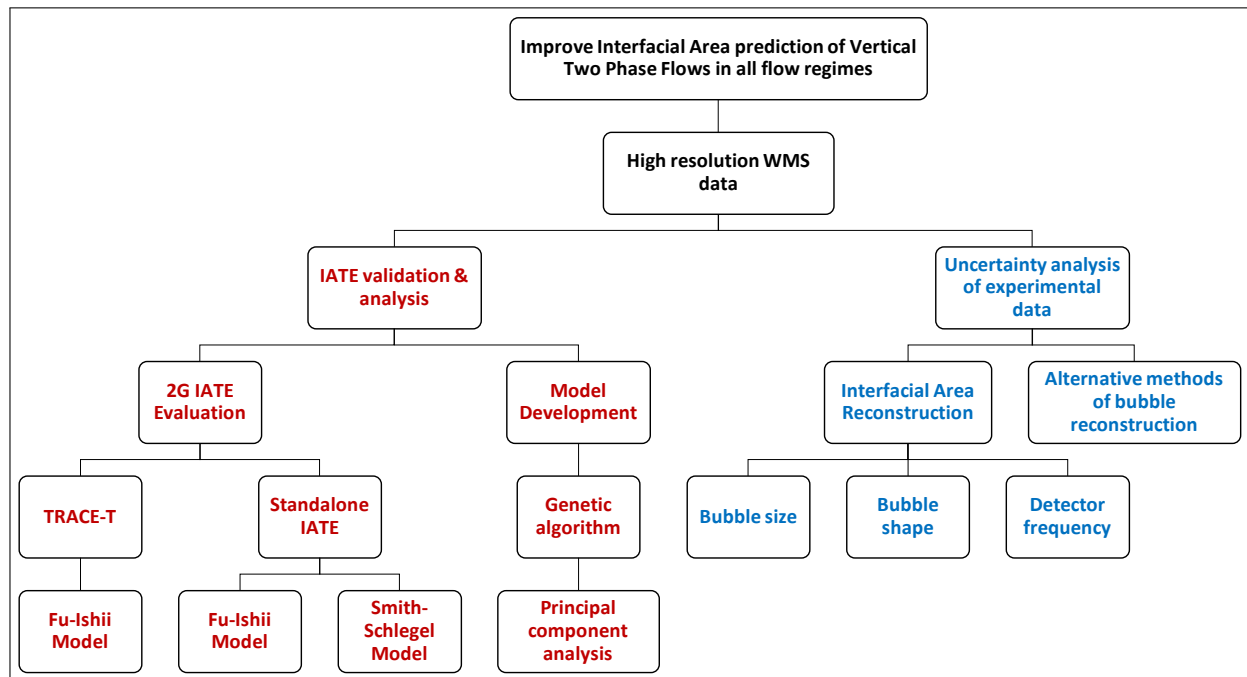


Figure 1.14: An overview of the dissertation organization.

A primary objective of this dissertation is to evaluate existing interfacial area transport equation models, using the TOPFLOW experimental dataset as a basis for the evaluation. The assessment of the Fu-Ishii model and the Smith-Schlegel model is discussed in **Chapter 3**. The implementation of the Fu-Ishii model in a development branch of the US NRC code TRACE (TRACE-T) is also validated against TOPFLOW data. In the same chapter, weaknesses of the models and needs for improvement are identified. A systematic approach towards improving the performance of current IATE models using genetic algorithms is presented in **Chapter 4**. The Purdue dataset using conductivity probes will be utilized to assess the universality of any improvements. Conclusions from this dissertation research effort and suggestions for future work are summarized in **Chapter 5**.

Chapter 2

Wire-mesh Sensors

2.1 Background

The wire-mesh sensor (WMS) was briefly introduced in Section 1.3.3. Even though this is an intrusive measurement technique, studies have shown that void-fraction distributions measured by WMS are that of the unobstructed flow. Wire-mesh sensors provide high-resolution measurements of two-phase flow characteristics in both time and space. In this dissertation the high-resolution TOPFLOW database from Helmholtz-Zentrum Dresden-Rossendorf [60, 8] is utilized to assess the prediction capabilities of current interfacial area transport equation (IATE) models for two-phase flows in small and large diameter pipes. This chapter will discuss the operating principles of the wire-mesh sensor and the algorithm developed to reconstruct the interfacial area concentration on the basis of the WMS raw data. The original work presented in this chapter is the uncertainty analysis of the interfacial area reconstruction algorithm, presented in Section 2.2.

2.1.1 Wire-mesh Sensor Operation

The wire-mesh sensor consists of two arrays of electrodes that are separated axially by a small distance (typically 1.5 mm) and placed perpendicular to one another. One plane of electrodes acts as a transmitter and another plane acts as the receiver. Through the usage of two multiplex circuits, staggered signals are sent to each transmitter electrode and are then recorded by the receiver electrodes [59]. The circuit layout and associated signal processing for a simplified 4-by-4 electrodes WMS are shown in Fig. 2.1 and Fig. 2.2 respectively. In these diagrams, the switches S1, S2, S3 and S4 correspond to individual transmitters. An alternating pulse is used to drive the transmitter voltage in order to avoid any electrolysis. If a conductive phase exists between the electrodes (eg. water), a current is generated in

the receiver. The sample/hold circuit (S/H) measures the current after a quasi-steady-state value is reached.

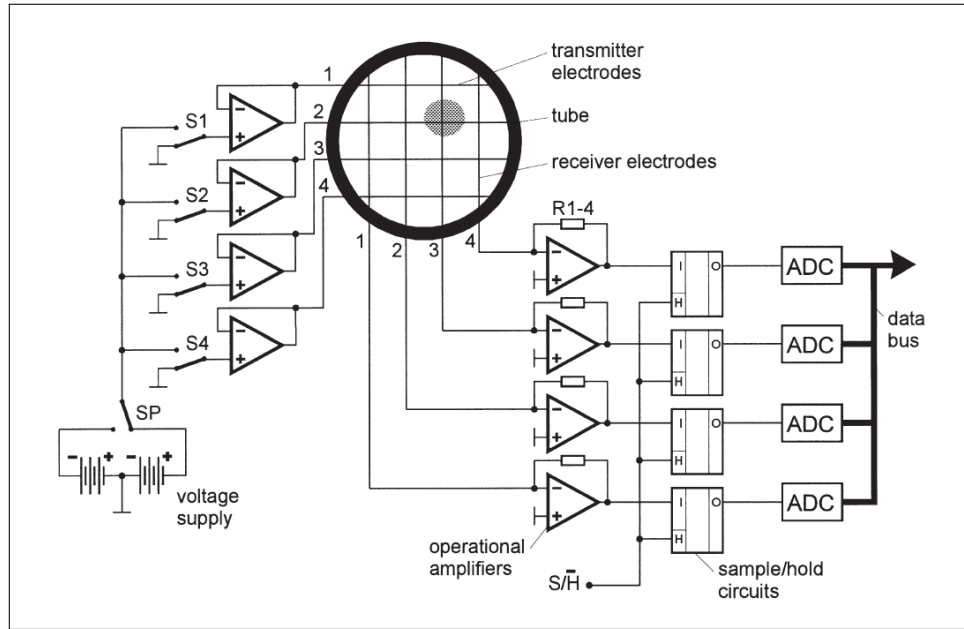


Figure 2.1: Simplified diagram of circuits used in the operation of the wire-mesh sensor [57].

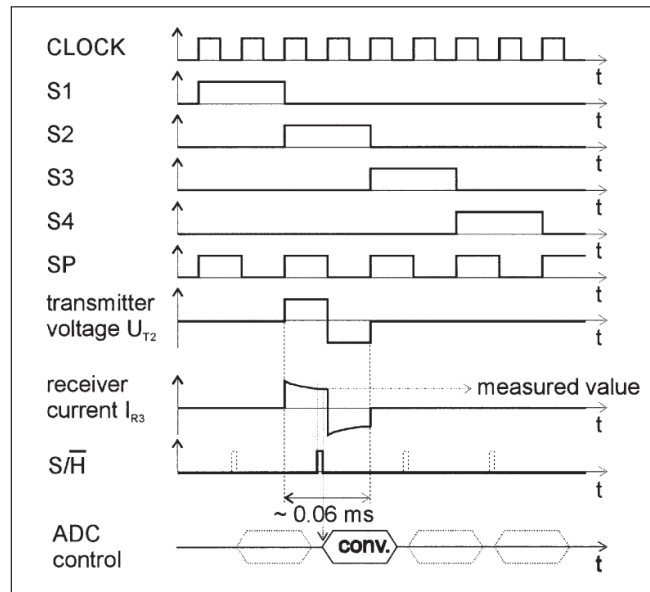


Figure 2.2: Diagram of control signals [57].

The electronic circuits enable data acquisition for N by M grid points (where N is the number of transmitter and M is the number of receivers) at a frequency of f_{wms} . The frequency of measurement is primarily limited by the capability of analog to digital converters

(ADC) that are used, as well as the RAM capacity available. The TOPFLOW DN50 tests used in this dissertation have been performed using a 16-by-16 array, operated at 2.5 kHz. The TOPFLOW DN200 tests used in this dissertation have been performed using a 64-by-64 array, operated at 2.5 kHz for 10s. This acquisition records 25000 frames containing $16 \times 16 = 256$ and $64 \times 64 = 4096$ measurements each, respectively for DN50 and DN200. The raw measurement provided by the ADC needs to be converted into usable void fraction values by calibration.

Several methods of calibration are available. A simple method is to measure the voltage that is recorded when the test section is filled with water and assume that the voltage transmitted through gas is negligibly small. Therefore, any local void fraction recorded at one of the N -by- N measured locations can be calculated by,

$$\alpha = 1 - \frac{V_{\text{meas}}}{V_{\text{water}}}, \quad (2.1)$$

where V_{meas} represents the measured local voltage during any given time, and V_{water} represents the voltage measured by the sensor when the pipe is completely filled with water.

As an alternative, the histogram of the voltage measurements during the tests itself can be used for calibration. An example is presented in Fig. 2.3. The histograms will usually have two maxima, one close to zero for the gas and another indicating the water value. Therefore, the second maximum is simply V_{water} . The histogram analysis of all frames and measurement

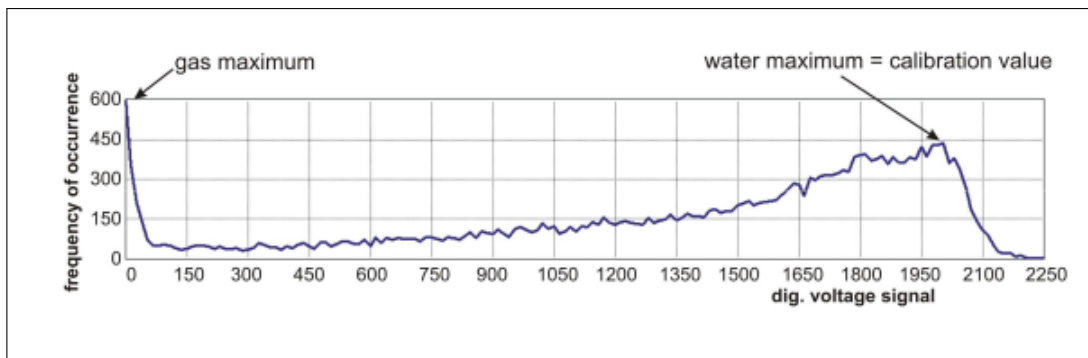


Figure 2.3: Histogram of the raw voltage measured for mesh (43,43), test 140, for the large diameter TOPFLOW test [8].

points will therefore allow a determination of temporally averaged, radial calibration values, $V_{\text{water}}(r)$. Unfortunately, for tests in which very high void fractions persist, i.e. annular flows, a separate calibration test (using only water) is required, as a maxima for water is harder to distinguish. For all other tests, the histogram calibration is utilized.

The calibration of the wire-mesh sensor also needs to account for intersections that are close to the edge of the pipe, Fig. 2.4. The pipe is electrically grounded, and hence a part

of the transmitter current is lost during transmission. Secondly, the zone of influence away from the pipe is well defined due to the formation of faraday cages in nearby intersections. However, close to the pipe, the zone of influence is irregular and dependent on intersection position. The calibration process accounts for both losses due to the grounding of the pipe and the decrease in region of influence.

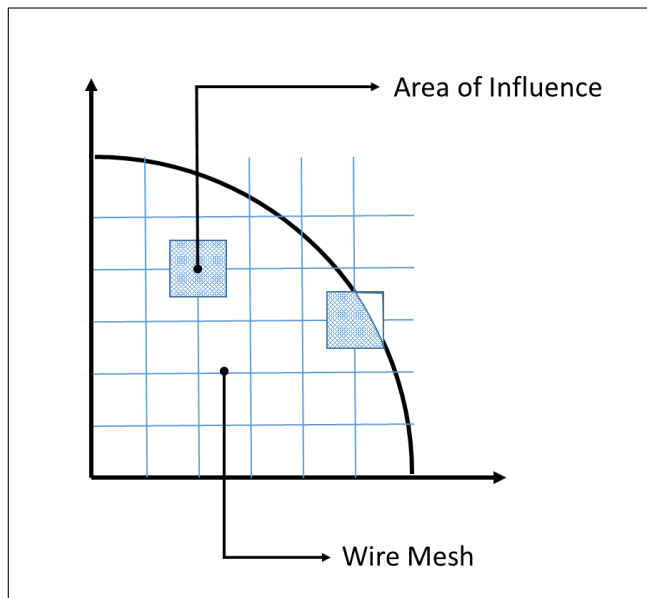


Figure 2.4: Wire intersections measure local conductivity. Intersections at the edge need to account for a smaller area of influence.

2.1.2 Post-processing Algorithms

Once the calibration is complete, the raw data can be converted into a three dimensional matrix of void fraction measurements, α_{ijk} (the subscript j , k represents spatial dimension and subscript i indicates frame number). Several post-processing algorithms have been previously established to utilize wire-mesh sensor data for the validation of thermal hydraulic system code or CFD codes.

2.1.2.1 Bubble velocity

The velocities of bubbles are not directly measured by the two-layer wire-mesh sensor (superficial gas and liquid velocities are known due to instrumentation at injection ports). In order to estimate the gas velocity from α_{ijk} , an assembly of two wire-mesh sensors can be used, or a so-called three layer sensors, where an intermediate transmitter layer is sandwiched between two receiver layers, so that the void fraction distribution can be measured simultaneously on

two separate pipe cross-sections . A typical schematic is presented in Fig. 2.5. The recorded void fraction distributions from both wire-mesh sensors (or from a three-layer WMS) are then cross-correlated [50] in order to estimate velocity. The fluctuation in void fraction is

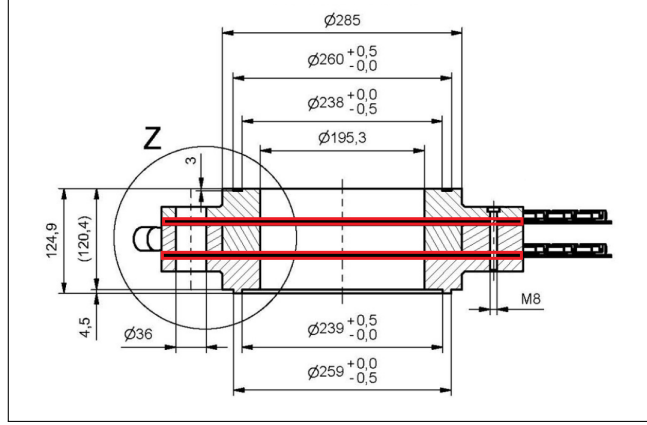


Figure 2.5: Schematic of a two-level wire-mesh sensor assembly. The separate wire-mesh sensors are highlighted in red [8].

defined by

$$\alpha'_{ijk} = \alpha_{ijk} - \bar{\alpha}_{jk} . \quad (2.2)$$

The fluctuating components are then cross-correlated by

$$F_{\Delta i, jk} = \frac{\sum_k \alpha'_{1,ijk} \alpha'_{2,(i+\Delta i)jk}}{\sqrt{\sum_k \alpha'^2_{1,ijk}} \sqrt{\sum_k \alpha'^2_{2,ijk}}} , \quad (2.3)$$

where Δi corresponds to a time-shift of $\Delta t = \Delta i / f_{\text{wms}}$. The cross-correlation is carried out using a Fast Fourier Transformation (FFT). The gas velocity can then be estimated by

$$v_g(j, k) = \frac{\Delta L}{\Delta i_{jk, \max}} f_{\text{wms}} , \quad (2.4)$$

where $\Delta i_{jk, \max}$ corresponds to $F_{\Delta i_{jk, \max}, jk} = \max(F_{\Delta i, jk})$. The axial distance between the two wire-mesh sensors is ΔL and the operating frequency f_{wms} .

2.1.2.2 Bubble identification

In order to evaluate characteristics of individual bubble structures, an algorithm was proposed by Prasser [62] to evaluate α_{ijk} and identify structures (bubbles) of interconnected non-zero void-fraction voxels. The goal of the identification is to determine a new matrix, b_{ijk} , that contains unique bubble numbers corresponding to the void fraction distributions.

In α_{ijk} , the central regions of the bubble will reflect a void fraction measurement of 100%. However, close to the edge of a bubble, an intermediate void fraction value between 0 and 100% will be recorded by the sensor. An even more complex situation arises when the void fraction contributions from two adjacent bubbles, influence the recording at a particular (j, k) intersection. In light of this, Prasser proposed the introduction of a threshold. The determination of a threshold is important, as a low value will cause unrealistic coalescence, and a high value will cause unrealistic breakup. The recursive algorithm begins by accumulating adjacent void fraction values that are above the threshold. The associated group of α_{ijk} are then assigned a unique bubble identification number, b .

2.1.2.3 Interfacial area reconstruction algorithm

The surface reconstruction algorithm aims to determine the interfacial area of the bubble structures measured by the wire-mesh sensor. Hereafter, the interfacial area reconstruction algorithm will be referred to as ‘HZDR algorithm’. The HZDR algorithm uses α_{ijk} as part of its input, along with the bubble identification matrix b_{ijk} , and the temporally averaged bubble velocity matrix v_{jk} .

The reconstruction begins by iterating over each unique bubble number, b . Thus, each bubble that has been identified previously, by the bubble identification algorithm, is treated separately. The HZDR algorithm loops through α_{ijk} , sweeping through j , k then moving to the next frame i . Since the location of the bubble is known, only the (i, j, k) values associated with bubble b are considered. Fig. 2.6 displays the hexahedral domain of analysis for each element in α_{ijk} . For each (i, j, k) , the seven neighboring void fraction values are considered.

The hexahedral domain is further distributed equally into four prisms, each containing four void fraction values (one such prism is shown in Fig. 2.6). The top and bottom horizontal planes of the prism are analyzed separately. This results in analysis of two isosceles triangles, displayed in Fig. 2.7. The corners of the prism reflect the measured void fraction values (corners of the cube). The internal void fraction value (located virtually at the geometric centroid of the cube’s horizontal surface) is an average of the four void fraction values recorded in the current i plane. A linear interpolation between the internal void fraction and two outer void fraction values determines the coordinates of the liquid-gas interface. The interpolation is repeated for the lower triangle.

Once the top and bottom coordinates of the liquid-gas interface are known, a skew quadrilateral can be formed, i.e. Fig. 2.8. The area of the quadrilateral is estimated by summing the area of 20 triangles. This process is repeated for the next three prisms within the hexahedral domain of analysis. It should be noted that the algorithm has considerations for several orientations of the interface, including an absence of any interface. Once all α_{ijk} for

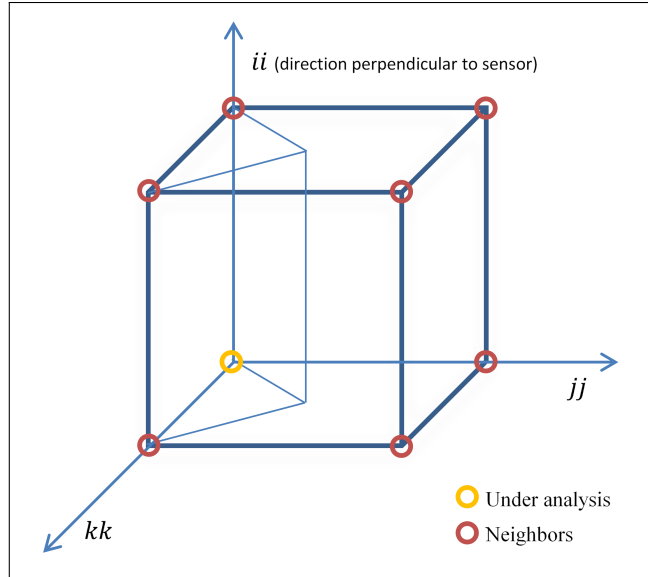


Figure 2.6: A hexahedral domain about a void fraction point under analysis and its neighbors; the spatial dimensions are indicated by the axis kk and jj , temporal dimension is indicated by axis ii .

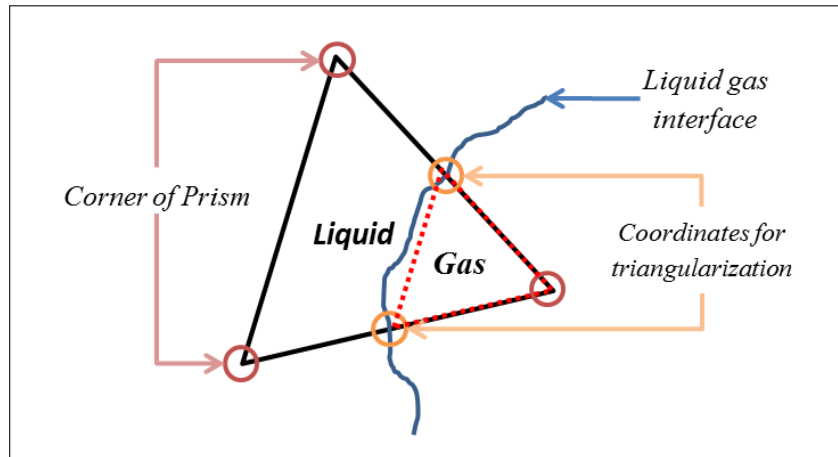


Figure 2.7: Detection of liquid-gas interface at the horizontal faces of prisms formed within the hexahedral domain.

a bubble have been analyzed, the estimated values of the interfacial area is available through summation of all quadrilateral areas. Therefore, the average interfacial area concentration, a_i , can also be determined by considering the total interfacial area of all bubbles recorded during a measurement.

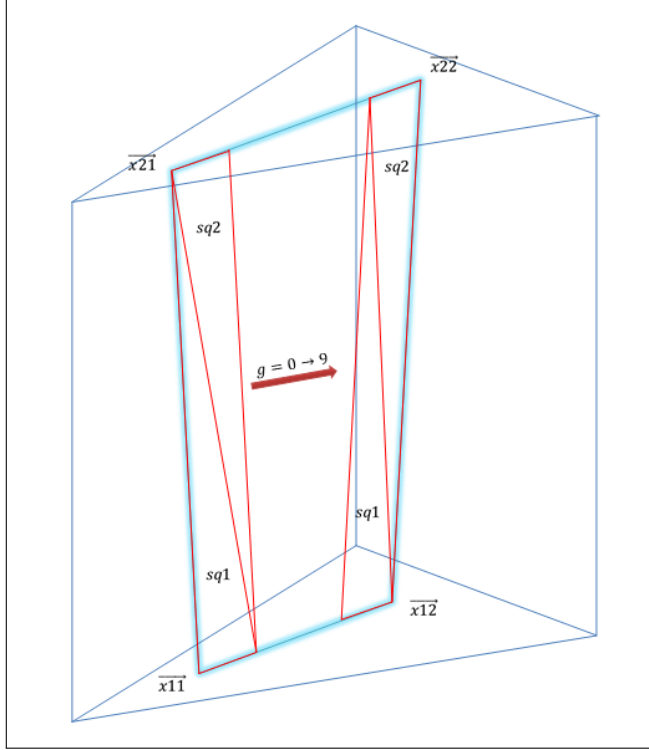


Figure 2.8: Triangularization of a skew quadrilateral in order to determine the area of the liquid-gas interface. There are 10 groups of $g(0 \rightarrow 9)$ that consist of two triangles each ($sq1$ and $sq2$). Areas of the triangles are calculated by vectors ($\vec{x}11, \vec{x}21, \vec{x}12$ and $\vec{x}22$).

2.2 Uncertainty Analysis

The HZDR algorithm (Section 2.1.2.3) estimates the bubble interfacial area concentration for any experimental measurement using wire-mesh sensors. The measurements of interfacial area concentration (a_i) are particularly useful for developing closure relationships for the two-fluid model (Section 1.2.1). However, in order for a meaningful validation of any closure relationships/model (such as the interfacial area transport equation model, Section 1.2.3), it is necessary to estimate the error introduced by the HZDR algorithm in calculating values of a_i . The objective of this section is to arrive at a prescription of error bars for interfacial area concentration that is indirectly measured by the wire-mesh sensor.

Several scripts are written in order to generate a synthetic void fraction distribution, $\alpha_{ijk}^{\text{syn}}$. The distribution is synthetic in the sense that the WMS signal has been generated numerically on the basis of a user-defined bubble distribution. The user defines the speed, radius, and injection location for each bubble. Bubbles may also be randomly distributed in both size and location. In order to test the surface reconstruction algorithm, the speed of all bubbles was selected to be uniform (as will be shown later, this too has an effect on the

error). At synthetic frame k , the bubble will have radius $R(k)$. At a particular (i, j, k) , the intersection is either completely filled by void or partially filled,

$$\begin{aligned} \alpha_{ijk}^{\text{syn}} &= 1 && |i \pm 1/2, j \pm 1/2| \leq R(k) \\ &= \frac{1}{\delta x \delta y} \iint_{i \pm 1/2, j \pm 1/2}^{R(k)} dA && \text{else.} \end{aligned} \quad (2.5)$$

In the case that the intersection is partially filled, an integral from the boundaries of the zone of influence (i.e. $(i \pm 1/2, j \pm 1/2)$) to the boundary of the bubble is used. The spacing of the wire-mesh sensor in the x and y direction is δx and δy .

Since the void fraction associated with a particular bubble is known, an accompanying bubble identification matrix b_{ijk}^{syn} is also generated concurrently. Thus, after generation of the synthetic matrices, they are used to mimic a measurement file to test the HZDR surface reconstruction algorithm. In the proceeding sections, several different cases for generation of synthetic bubbles will be considered. The figure of merit to evaluate the reconstruction algorithm is the relative error on the reconstructed interfacial area density, defined by

$$\text{Relative Error [\%]} \equiv \frac{a_i^{\text{HZDR}} - a_i^{\text{syn}}}{a_i^{\text{syn}}} . \quad (2.6)$$

2.2.1 Convex Hull Algorithm

In order to assess the accuracy of the triangulation method that is used in the HZDR algorithm, a convex hull algorithm from a third party computational geometry library, CGAL [11], is utilized. A convex hull algorithm considers all input coordinates and attempts to create a closed polytope surface that all coordinates. An example of using a convex hull algorithm is presented in Fig. 2.9. The convex hull algorithm allows a secondary estimation of the interfacial area concentration. The concurrent evaluation of both ‘HZDR’ algorithm and ‘CGAL’ estimations of interfacial area will justify efficacy of the reconstruction algorithm.

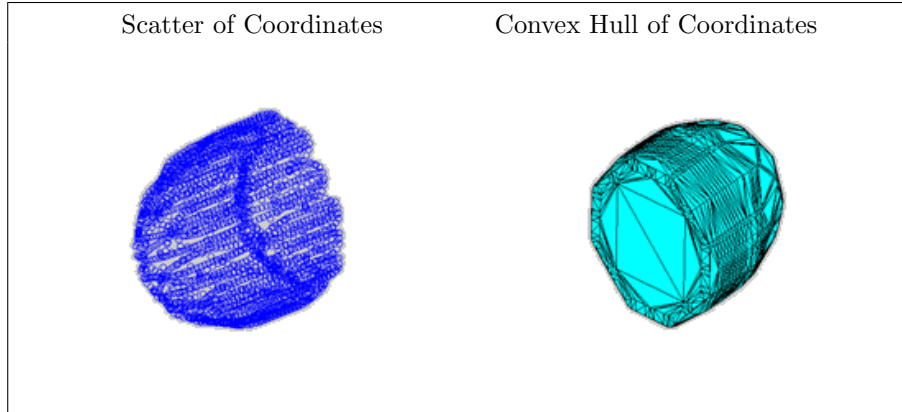


Figure 2.9: A 3D scatter plot of a bullet bubble’s coordinates generated by the HZDR algorithm (left). The convex hull of the coordinates generated by CGAL (right).

2.2.2 Multiple Spherical Bubbles

A preliminary test consisted of error evaluation for multiple synthetic spherical bubbles. Fig. 2.10 presents results for 1000 bubbles that are randomly distributed in the pipe cross section and randomly sized between 3 and 10 mm. It is assumed that the bubbles move at a velocity of 1 m/s and that the acquisition frequency of the WMS is 2500 Hz. A visual of the synthetic bubbles generated for this case is displayed on the right hand side of Fig. 2.10. The x-axis of the graph in Fig. 2.10 indicates the amount of white noise that is artificially added. The noise perturbs the void fraction distribution by a percentage about its nominal value. The results indicate that with no noise added, there is very little error introduced by the HZDR algorithm. Typical WMS noise level on the void fraction measurement is about 2%, for which the HZDR surface integration algorithm provides very accurate results (even at 5% noise added, the error remains below 2%). The CGAL algorithm slightly underestimates the interfacial area concentration. Fig. 2.11 presents results for larger number of bubbles generated. As the number of frames is kept constant (and thus the total flow volume), this represents a tighter packing of bubbles. The magnitude of error remains the same. The CGAL algorithm consistently underestimates the bubbles surface area for the typical experimental noise values of about 2%.

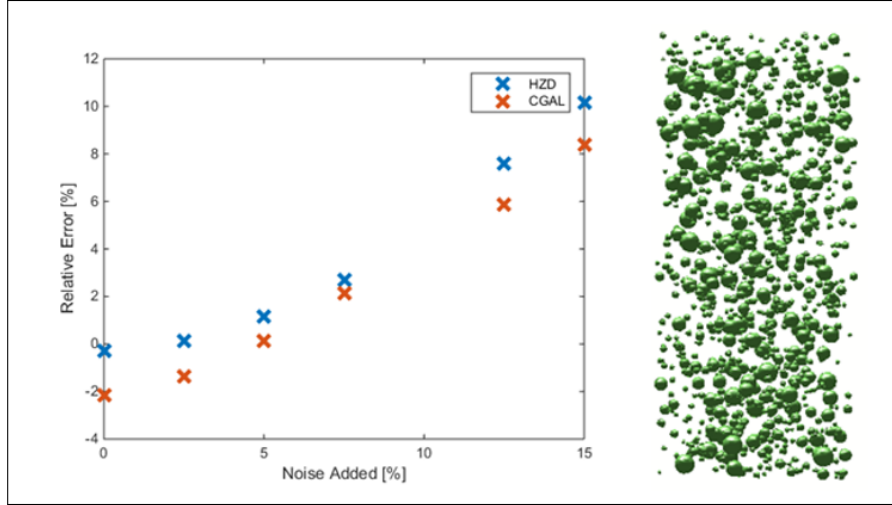


Figure 2.10: Error on interfacial area concentration for a set of 1000 Spherical bubbles ranging between 3 mm to 10 mm in diameter, with velocity of 1 m/s.

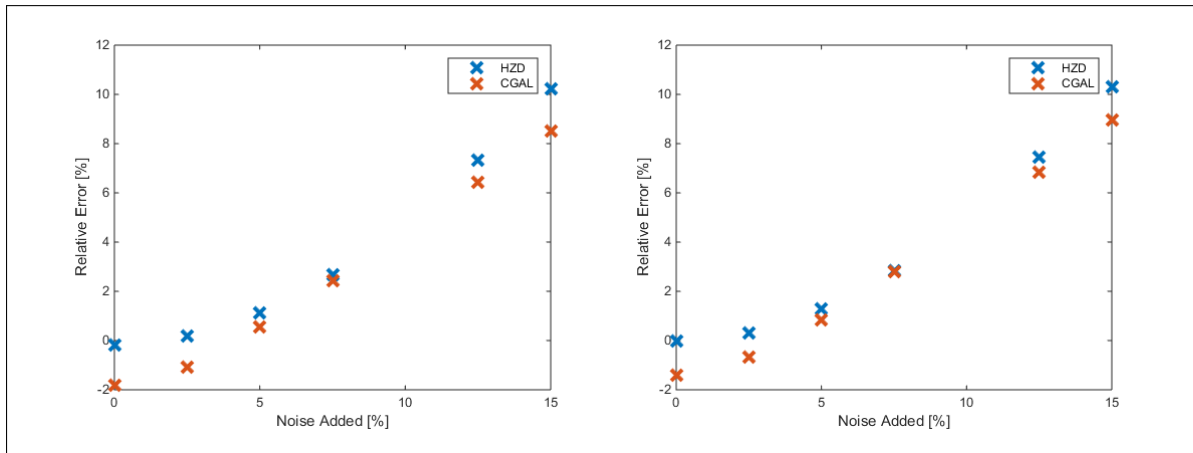


Figure 2.11: Error for 2000 (left) and 4000 (right) Spherical bubbles between between 3 mm to 10 mm in diameter, with velocity of 1 m/s.

2.2.3 Sensor Operating Frequency

Figs. 2.13 and 2.14 present the error in reconstructing the interfacial area as the operating frequency is manipulated for a spherical bubble of 3 mm, 5 mm and 10 mm diameter respectively. The x-axis indicates the bubble displacement that occurs between frames of measurement (this is determined by dividing the bubble velocity by the operating frequency. The higher the acquisition frequency, the lower the displacement of the bubbles between successive frames). In order to concurrently present error introduced by bubble location on the wire-mesh grid, 350 bubbles of equivalent size are randomly distributed in the pipe cross section. The error bars indicate one standard deviation of the error distribution about the

mean.

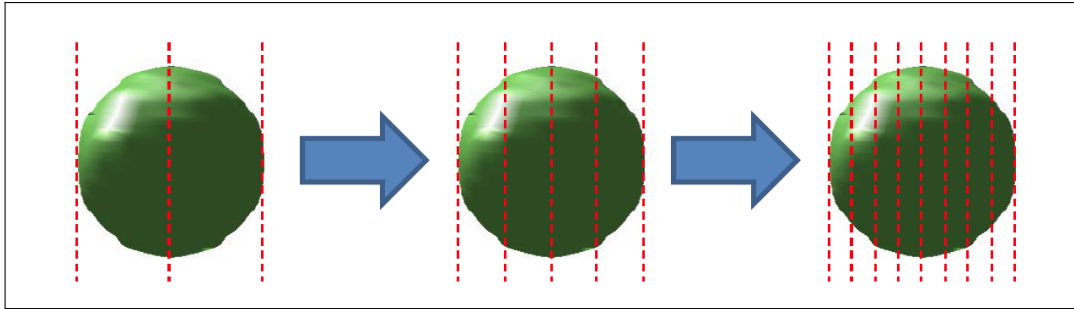


Figure 2.12: Illustration of the impact of increasing operating frequency on capturing data.

The error on the interfacial area introduced by the HZDR algorithm increases slightly for frequencies above 2.5 kHz (below a displacement of 0.4 mm). At high frequencies, there is a larger spread in the error due to varying bubble locations. This result indicates that operating at a high frequency is not necessarily beneficial. A similar result is noted for the 5 mm bubble. The 10 mm spherical bubble benefits from its larger size and has a lower error at low operating frequencies. On the other hand, the 10 mm bubble experiences significantly larger error at high operating frequencies (displacement below 0.4 mm). In all cases, the CGAL algorithm performs more poorly than the HZDR algorithm.

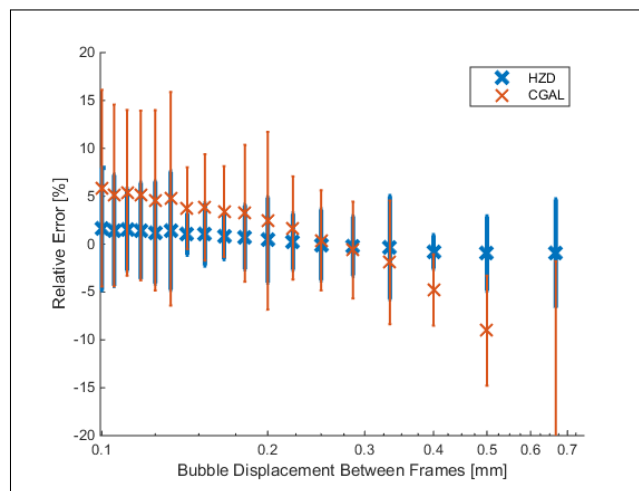


Figure 2.13: Error for varying operating frequencies for a 3 mm spherical bubble at 1 m/s.

It is important to note that in general, the optimal operating frequency depends on the bubble size and bubble velocity. Fig. 2.15 presents the error for bubble of various sizes moving at a velocity of 1 m/s, assuming an acquisition frequency of 2.5 kHz. The error for the HZDR algorithm is low for 2.5 mm to 7.5 mm bubbles. However, error begins to increase

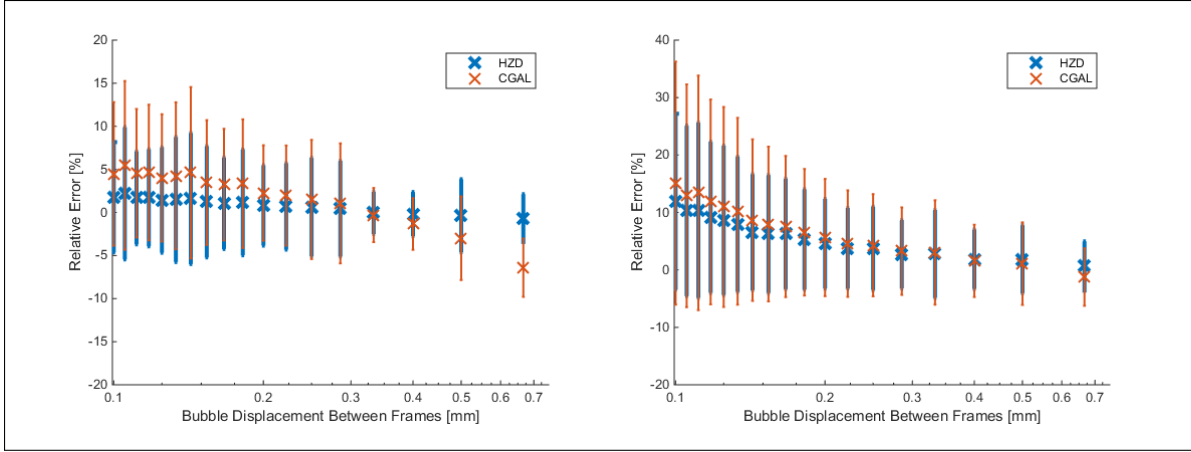


Figure 2.14: Error for varying operating frequencies for 5 mm (left) and 10 mm (right) spherical bubbles at 1 m/s

for larger bubbles. For more complicated structures in two phase flow, it would be important to consider the average radius of curvature.

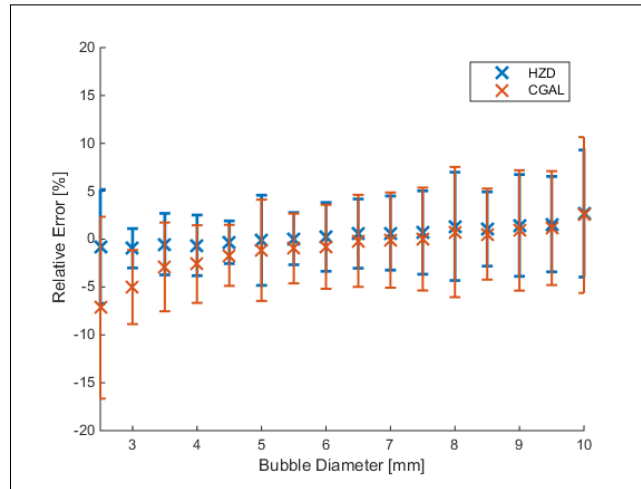


Figure 2.15: Error for varying bubble diameter at a constant operating frequency of 2.5 kHz (0.4 mm bubble displacement between frames) at 1 m/s.

2.2.4 Ideal Bullet Bubble

In addition to spherical bubbles, a bullet-shaped bubble was also tested, representative of Taylor bubbles encountered in slug flows in small diameter pipes. The shape of the ideal bullet bubble is designed to have a hemispherical head and a cylindrical tail. The length of the tail is modified in multiples of the radius. The results for this shape are presented in Fig. 2.16. The HZDR algorithm performs well, decreasing in error as the length of the

tail increases. This indicates that the HZDR algorithm calculates objects with a simple curvature (such as a cylinder) more accurately, and thus a majority of the error originates from surface area reconstruction of the hemispherical head. The CGAL algorithm is mostly outperformed by the HZDR algorithm, but however has a consistent error.

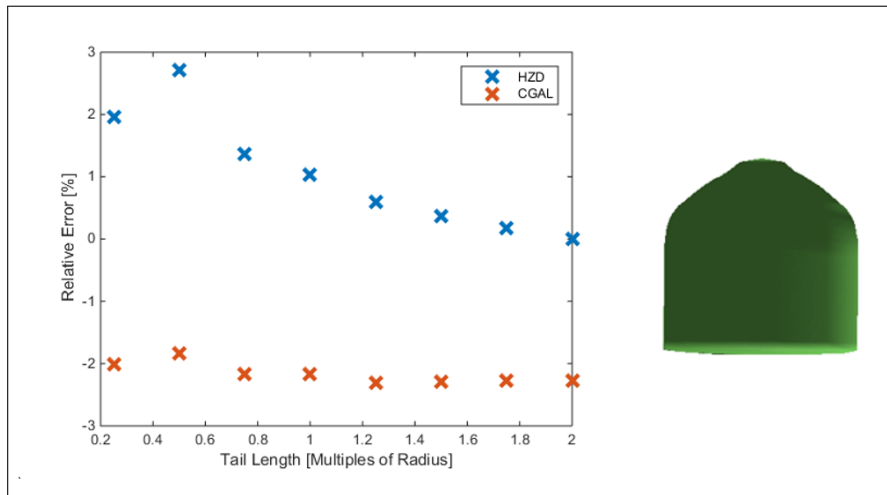


Figure 2.16: Error for a 10 mm ideal bullet shaped bubble with varying tail lengths at at 1 m/s.

2.2.5 Ideal Bullet Bubble with Internal Cavity

In order to complicate the geometry of the bullet bubble, an internal cavity at the tail end was introduced. The internal cavity is assumed to have the same geometry as the head, i.e. hemispherical. The right hand side of Fig. 2.17 provides a visualization of the bubble’s vertical cross-section. It was expected that since the algorithm handles the hemispherical head of the bullet bubble, it would be capable of addressing the internal cavity. However, as indicated by the magnitude of errors in Fig. 2.17, both algorithms tested have been unsuccessful.

The notion that the internal cavity is introducing a large error can be inferred upon further analysis of Fig. 2.17. Firstly, as displayed in Fig. 2.16, the ideal bullet bubble without the internal cavity and equivalent specifications has an error less than 3%. Furthermore, as the length of the tail increases (i.e. the proportion of total surface area contribution from the cylindrical body increases) the error decreases. As discussed previously, the algorithms are capable of handling simple cylindrical surfaces. As the CGAL algorithm follows the error propagation of the HZDR algorithm, the source of the error stems from the generation of coordinates for triangularization. Upon debugging the HZDR algorithm, it was found that the algorithm ignored void fraction values that comprised the ‘skirt’ of the bubble.

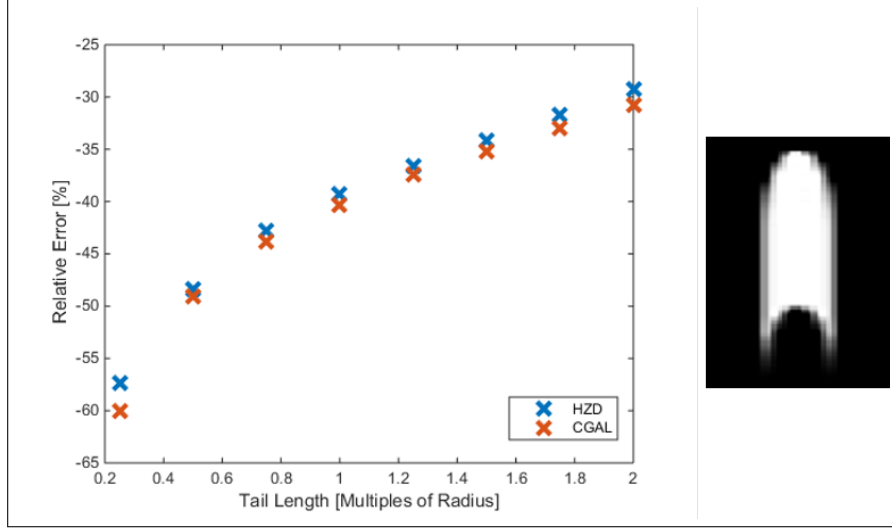


Figure 2.17: Error for a 10 mm ideal bullet shaped bubble with an internal cavity and varying tail lengths at at 1 m/s.

Fig. 2.18 presents visualizations of three frames that comprise the bubble. The actual edges of the bubble are presented by continuous lines (blue indicating an outer edge, red indicating an inner cavity edge). The coordinates that are generated by the HZDR algorithm for interfacial area reconstruction are also presented (red crosses). At frame 6, the coordinates successfully wrap around the hemispherical head of the bubble. At frame 16, coordinates are successfully generated for the outer and inner edge, though with less accuracy for the inner edge. However, at frame 20, no coordinates are generated. This occurs because the code is designed to overlook isolated low void fraction values in the 2D void fraction matrix. There is a constant threshold for each bubble that determines when a local void fraction value is sufficiently low to be ignored.

A modification of the HZDR algorithm to improve cavity detection has been made. The modified algorithm attempts to identify bubbles that have an internal cavity by comparing neighboring void fraction values. The bubbles that have been identified as containing a cavity are subject to a varying threshold for isolated void fraction values; all other bubbles will have a constant threshold, as in the original HZDR algorithm. The rationale behind such a modification is to retain the performance of the original algorithm for successfully analyzed shapes and attempt to improve performance for bubbles with irregular shapes. A varying threshold would allow the algorithm to include lower void fraction values in its analysis and therefore account for isolated void fractions, such as those at the skirt of the slug bubble.

The results of the modified HZDR algorithm are presented in Table 2.1. The test cases consist of a mix of spherical ('SPH') and bullet bubbles with internal cavity ('CAV'); an example is presented in Fig. 2.19. The bubble locations are randomly generated; bubble

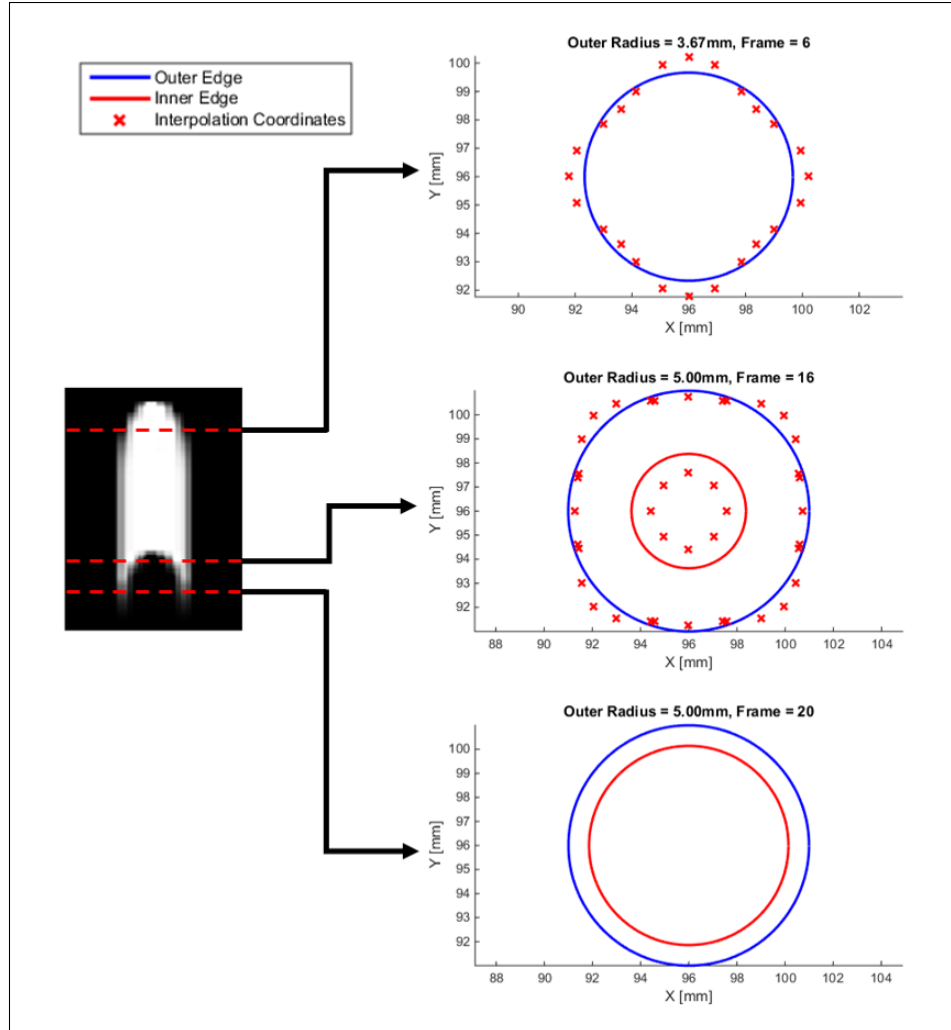


Figure 2.18: Three separate frames during the computational analysis of the bullet bubble with cavity. The continuous lines indicate the synthetic shape's inner and outer edge. Discrete data represent points that have been interpolated by the HZDR algorithm.

diameters may be constant or randomly distributed within a range. The first case tests whether spherical bubbles are analyzed equivalently by both algorithms. The result is noteworthy as it indicates that the analysis of spherical bubbles is exactly retained. Cases 5-7 focus on only analyzing CAV bubbles. The result is significant as an improvement of above 10% is realized. Tests 2-4 are interesting as they mix SPH and CAV bubbles. In all three cases the improvement is lower than 4%. This is due to the fact that two thirds of the bubbles are spherical and will have the exact same error for both versions of the algorithm (as SPH bubbles are treated equally in both algorithms). Thus, when an average is taken of the error of all bubbles, the benefits of the modified HZDR algorithm is concealed. However, with regards to experimental data for validation, the average interfacial area density

recorded over a physical test is of interest. Thus, the improvement in CAV bubbles will play a significant role as the total area of CAV bubbles are substantially larger than SPH bubbles (e.g. CAV bubbles had 16 times the area of SPH bubbles on average for case 6).

Table 2.1: Improvement of cavity detection in the HZDR algorithm.
Error is calculated by Eq. (2.6).

Case	HZDR Algorithm Error [%]	Cavity Detect Error [%]	Improvement [%]
1. 1000 of 3-10 mm SPH	1.622	1.622	Equal
2. 200 of 10 mm SPH 100 of 20 mm CAV	4.482	3.889	0.59
3. 200 of 7-5 mm SPH 100 of 14-30 mm CAV	5.416	4.810	0.61
4. 200 of 7.5 mm SPH 100 of 22.5 mm CAV	13.99	10.67	3.33
5. 200 of 10-20 mm CAV	25.69	14.47	10.21
6. 200 of 20 mm CAV	25.82	14.45	11.37
7. 200 of 10-20 mm CAV	24.69	13.34	11.35

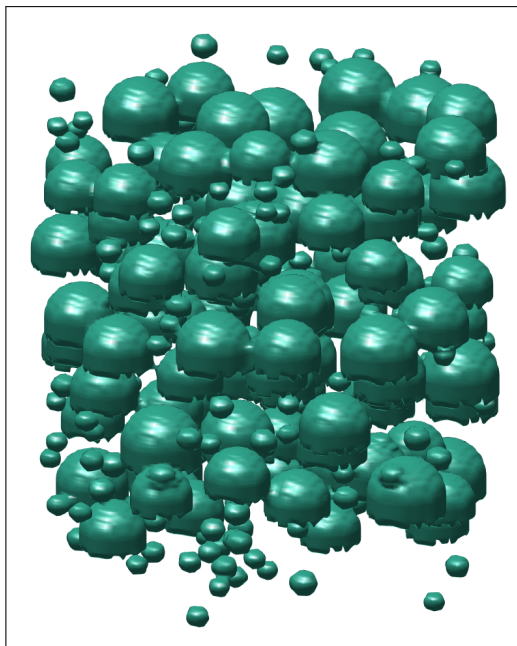


Figure 2.19: A 3D representation of the void fraction distribution generated for analysis in Case 3, Table 2.1.

2.2.6 Bubbles Approaching Coalescence

In typical two-phase flows, bubbles are subject to break-up and coalescence. In this section we analyze the accuracy of the interfacial area reconstruction algorithm when two bubbles

are merged together or very close to each other. Two spherical bubbles are modeled, one of 15 mm and the other of 20 mm. The process of coalescence is visualized in Fig. 2.20. The primary objective for this case is to determine if the HZDR algorithm is capable of calculating the area of a complex shape. Fig. 2.21 presents the error for this case, where the x-axis represents the normalized distance between the centroids of the bubbles. As experienced with the ideal bullet bubble, it is expected that the error will be greatest when the shape being analyzed is complex – this would occur at the onset of coalescence. The propagation of the error supports this expectation. However, the error remains low for all configurations. The CGAL algorithm performs better than the HZDR algorithm for this case.

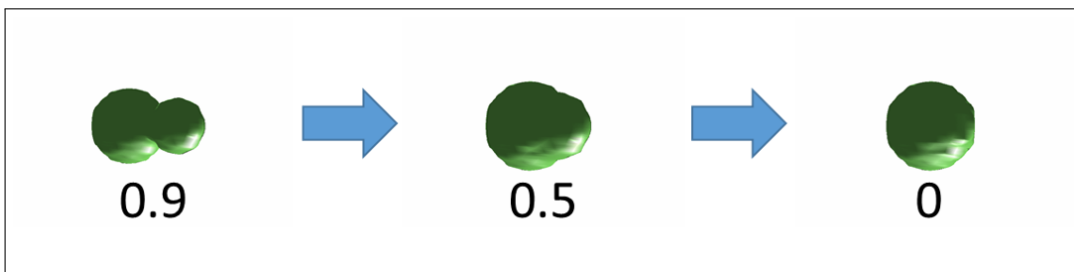


Figure 2.20: Visual of a 15 mm bubble coalescing into a 20 mm bubble traveling vertically at 1 m/s. The numeric values indicate the normalized proximity of the bubble centroids.

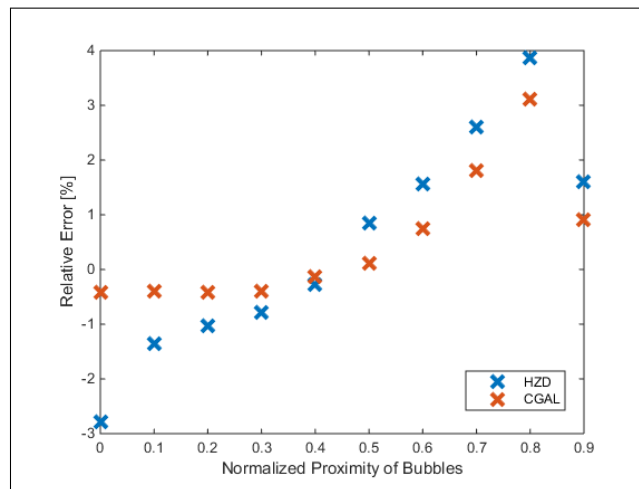


Figure 2.21: Error for bubbles approaching coalescence.

2.3 Remarks

As wire-mesh sensors indirectly obtain interfacial area concentration (through a reconstruction algorithm developed by other authors, Section 2.1.2.3), the dissertation work is focused on quantifying introduction of any error (presented in Section 2.2).

It is found that while a 2.5 kHz acquisition frequency is optimal for 1 m/s bubbles, it can be deduced that for a wider velocity range the error will be bounded within 10% given the interchangeability between frequency and velocity. Significantly higher or lower frequencies adversely impacts the reconstruction process. Slug bubbles are successfully analysed with varying tail lengths causing no impact on the reconstruction. However, when an internal cavity is artificially added to the tail of the slug bubble, a significant error ($\leq \pm 25\%$) is introduced. In order to address this issue, a marking process is suggested to modify the thresholds used for reconstruction in bubbles with internal cavities. The modified algorithm reduces average error to $\leq \pm 15\%$. In most experimentally observed flows, a very concave internal cavity is not expected. A conservative estimate of $\pm 10\%$ is suggested for the uncertainty associated with interfacial area concentration measurements using wire-mesh sensors.

Chapter 3

Two-group Interfacial Area Transport Equation

The interfacial area transport equation model introduced in Section 1.2.3 is specifically known as the one-group model. The denotation one-group reflects the fact that all bubbles in the flow are grouped together and accounted for by a single interfacial area transport equation. A similarity with bubble groups can be found in neutronics, in which the solution of the neutron transport equation, even in its simpler diffusion approximation, requires multiple groups (and associated population balance equations) to reflect varying microscopic cross sections with respect to energy. In multiphase flows, the forces that act on a bubble (such as drag) and bubble interaction mechanisms (break-up and coalescence) depend strongly on the bubble shape. In general, five bubble shapes can be identified: spherical, distorted, cap, Taylor and churn-turbulent structure respectively. Empirically [33], it is noted that the drag coefficient and bubble interaction mechanisms for small spherical bubbles behave quite differently with respect to larger bubbles. Because of these considerations, in the most advanced IATE formulation, two bubble groups are proposed, as schematically illustrated in Fig. 3.1. The first group (referred to as ‘group-1’) considers smaller bubbles and contains spherical and distorted shapes. The second group (referred to as ‘group-2’) considers larger structures such as cap bubbles, slugs (or Taylor) and churn-turbulent structures. Two separate population balance (or interfacial area transport) equations are formulated to model the dynamics of the interface associated to each group. The original work presented in this chapter is the evaluation of two-group interfacial area transport models for a novel experimental database (reported in Section 3.2).

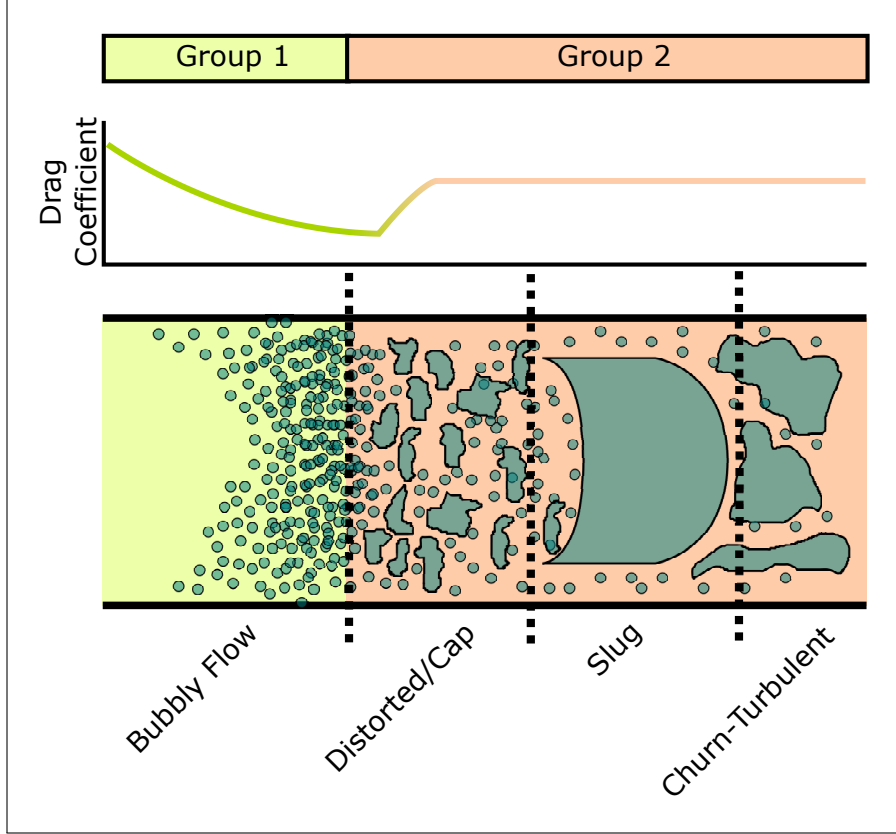


Figure 3.1: Classification of bubbles and variation in interfacial drag in group 1 and group 2.

3.1 Formulation

In the one-group IATE formulation, the bubble distribution is integrated over all sizes (Eq. (1.28)). However, for the two-group formulation, a criterion to separate the two groups needs to be identified. The largest bubble shape in group-one corresponds to the distorted bubble. Ishii and Zuber have estimated that the maximum distorted bubble size can be expressed by [38]

$$D_c = 4\sqrt{\frac{\sigma}{g\Delta\rho}}. \quad (3.1)$$

Therefore, bubbles of equivalent diameter given by Eq. (3.1) are considered to be the upper limit for group-1 bubbles. Bubbles with equivalent diameters above the value in Eq. (3.1), will fall into group-two. Therefore the integration limits are V_{\min} to V_c and V_c to V_{\max} . The Boltzmann equation, Eq. (1.21), is again multiplied by $A_i(V)$ ¹, but integrated over the

¹Defined as the surface area of bubbles with volume V .

respective group limits. The resulting equations are:

$$\frac{\partial a_{i1}}{\partial t} + \nabla \cdot (a_{i1} v_{i1}) + \int_{V_{\min}}^{V_c} \left[A_i \frac{\partial}{\partial V} \left(f \frac{dV}{dt} \right) \right] dV = \int_{V_{\min}}^{V_c} \left(\sum_j S_j + S_{ph} \right) A_i dV, \quad (3.2)$$

$$\frac{\partial a_{i2}}{\partial t} + \nabla \cdot (a_{i2} v_{i2}) + \int_{V_c}^{V_{\max}} \left[A_i \frac{\partial}{\partial V} \left(f \frac{dV}{dt} \right) \right] dV = \int_{V_c}^{V_{\max}} \sum_j S_j A_i dV, \quad (3.3)$$

where the average interfacial velocity is given by:

$$v_{i1}(x, t) \equiv \frac{\int_{V_{\min}}^{V_c} f(V, x, t) A_i(V) v(V, x, t) dV}{\int_{V_{\min}}^{V_c} f(V, x, t) A_i(V) dV}, \quad (3.4)$$

$$v_{i2}(x, t) \equiv \frac{\int_{V_c}^{V_{\max}} f(V, x, t) A_i(V) v(V, x, t) dV}{\int_{V_c}^{V_{\max}} f(V, x, t) A_i(V) dV}. \quad (3.5)$$

The third term in Eqs. (3.2) and (3.3) represents the change in interfacial area due to the bubble volume change and can be simplified further:

$$\int_{V_{\min}}^{V_c} \left[A_i \frac{\partial}{\partial V} \left(f \frac{dV}{dt} \right) \right] dV = \left(\frac{\dot{V}}{V} \right) \left(-\frac{2}{3} a_{i1} + A_{ic} f_c V_c \right), \quad (3.6)$$

$$\int_{V_c}^{V_{\max}} \left[A_i \frac{\partial}{\partial V} \left(f \frac{dV}{dt} \right) \right] dV = \left(\frac{\dot{V}}{V} \right) \left(-\frac{2}{3} a_{i2} - A_{ic} f_c V_c \right), \quad (3.7)$$

In contrast to the one-group volumetric expansion term, an intergroup transfer term $A_{ic} f_c V_c$ appears in the two-group transport equations. This term is determined by assuming that the bubble size distribution is linear² [32, Ch. 10] with respect to the bubble volume V_c ,

$$A_{ic} f_c V_c = a_{i1} \chi \left(\frac{D_c}{D_{sm1}} \right)^2, \quad (3.8)$$

where χ is a distribution parameter bounded by $0 \leq \chi \leq 2$. Good agreement with experimental data is obtained when χ is one. The Sauter mean diameter, D_{sm} , is defined as $6\alpha_g/a_i$. Thus using the definitions Eqs. (1.26) and (3.6) to (3.8), the Eqs. (3.2) and (3.3) form the

²The distribution for Fu-Ishii model is presented in Fig. 3.4.

two-group interfacial area transport equations:

$$\begin{aligned} \frac{\partial a_{i1}}{\partial t} + \nabla \cdot (a_{i1} v_{i1}) &= \frac{2}{3} \frac{a_{i1}}{\alpha_{g1}} \left[\frac{\partial \alpha_{g1}}{\partial t} + \nabla \cdot (\alpha_{g1} v_{g1}) - \eta_{ph} \right] - \\ &\quad - \chi \left(\frac{D_c}{D_{sm1}} \right)^2 \frac{a_{i1}}{\alpha_{g1}} \left[\frac{\partial \alpha_{g1}}{\partial t} + \nabla \cdot (\alpha_{g1} v_{g1}) - \eta_{ph} \right] + \\ &\quad + \sum_j \phi_{j1} + \phi_{ph} , \end{aligned} \quad (3.9)$$

$$\begin{aligned} \frac{\partial a_{i2}}{\partial t} + \nabla \cdot (a_{i2} v_{i2}) &= \frac{2}{3} \frac{a_{i2}}{\alpha_{g2}} \left[\frac{\partial \alpha_{g2}}{\partial t} + \nabla \cdot (\alpha_{g2} v_{g2}) \right] + \\ &\quad + \chi \left(\frac{D_c}{D_{sm1}} \right)^2 \frac{a_{i1}}{\alpha_{g1}} \left[\frac{\partial \alpha_{g1}}{\partial t} + \nabla \cdot (\alpha_{g1} v_{g1}) - \eta_{ph} \right] + \\ &\quad + \sum_j \phi_{j2} , \end{aligned} \quad (3.10)$$

where interaction source terms are simplified using Eq. (1.30). For one-dimensional, steady-state, adiabatic air-water flows the two-group equations simplify to:

$$\frac{\partial}{\partial z} (a_{i1} v_{i1}) = \frac{2}{3} \frac{a_{i1}}{\alpha_{g1}} \left[\frac{\partial}{\partial z} (\alpha_{g1} v_{g1}) \right] - \chi \left(\frac{D_c}{D_{sm1}} \right)^2 \frac{a_{i1}}{\alpha_{g1}} \left[\frac{\partial}{\partial z} (\alpha_{g1} v_{g1}) \right] + \sum_j \phi_{j1} , \quad (3.11)$$

$$\frac{\partial}{\partial z} (a_{i2} v_{i2}) = \frac{2}{3} \frac{a_{i2}}{\alpha_{g2}} \left[\frac{\partial}{\partial z} (\alpha_{g2} v_{g2}) \right] + \chi \left(\frac{D_c}{D_{sm1}} \right)^2 \frac{a_{i1}}{\alpha_{g1}} \left[\frac{\partial}{\partial z} (\alpha_{g1} v_{g1}) \right] + \sum_j \phi_{j2} , \quad (3.12)$$

Both Eqs. (3.11) and (3.11) have similar structures. The left-hand side represents advection of interfacial area concentration. The first term on the right-hand side represents interfacial area changes due to volumetric expansion (mainly attributed to changes in pressure head along the pipe axis). The second term on the right-hand side is equivalent and opposite for both group-1 and group-2 and represents intergroup transfer due to volumetric expansion. The last term on the right-hand side represents the source/sink terms associated with bubble interaction mechanisms (break-up and coalescence).

This system of first order PDEs requires group-wise boundary condition specification for interfacial area concentration a_{i1} and a_{i2} , and values for group-wise interfacial velocity (v_{i1} and v_{i2}) and void fraction (α_{g1} and α_{g2}). For the sake of simplicity, the fluid phase velocities (v_{g1} and v_{g2}) are assumed to equal the interfacial velocity. Finally, closure of the IATE model requires correlations for the group-wise interaction mechanisms (ϕ_{j1} and ϕ_{j2}).

To close group-wise properties (a_{i1} , a_{i2} , α_{g1} , α_{g2} , v_{g1} , v_{g2}), a modified two-fluid model was proposed by Sun [76]. Instead of three transport equations for the entirety of the disperse

phase, three transport equation would be used for each group³. There are obvious challenges to using such a model, as additional complexity in modelling the inter-group closure terms arise. Ishii proposed to use a gas mixture momentum equation instead, in combination with a drift flux correlation for the estimation of the relative group-wise velocities [30].

3.1.1 Existing Two-group Models

Several models based on the two-group IATE formulation have been proposed in the literature. They differ with regards to their range of applicability and in the degree of complexity. As is the case for many thermal-hydraulic phenomena, a more complex model does not necessarily guarantee better predictive capabilities. IATE models specific to two-phase flows in vertical pipes are summarized in Table 3.1. Earlier models tend to be simpler in terms of interaction mechanisms covered, such as the Hibiki-Ishii model. The Fu-Ishii model is considered the state-of-the-art model for two-phase flows in small diameter vertical pipes. Differences in flow dynamics between flows in small and large diameter pipes (discussed further in Section 3.4.1) have motivated the development of the Smith-Schlegel model. The Sun model was developed specifically for rectangular vertical channels instead.

Table 3.1: Availability of existing models that are applicable to vertical two-phase flows.

Model	Applicability	Mechanism Exclusion	Parameters
Hibiki-Ishii [26]	Vertical small diameter Bubbly to slug flow	Shearing-off, surface instability, intergroup expansion	12
Fu-Ishii [23, 22]	Vertical small diameter Bubbly to churn-turbulent	Intergroup expansion	11
Smith-Schlegel [74, 65]	Vertical large diameter Bubbly to annular	Intergroup expansion	17
Sun [77]	Vertical rectangular channel Bubbly to annular	None	15

In addition to the IATE formulations listed in Table 3.1, other models can be found in the literature for flows involving phase change, including boiling. Kocamustafaogullari and Ishii [41] included the modeling of active nucleation site density of the heated surface. Hibiki and Ishii [27] modelled nucleation site density using size and angle distribution of cavities present on the heated surface. Bubble departure size was modeled by Situ [72], and bubble departure frequency by Euh [17]. Furthermore, the sink term due to condensation has been

³This results in 9 total transport equations. The liquid phase is modelled by 3 equations, and two gaseous phase groups are modelled by 3 equations each.

modeled by Park [56]. The present study focuses on adiabatic air-water flows and thus does not employ any of these models.

While the two-group interfacial area transport equations Eqs. (3.11) and (3.12) are common among all two-group IATE formulations, the interaction mechanisms (ϕ_{j1} and ϕ_{j2}) are formulated differently depending on the specific application. However, the prototypical formulation for the interaction source terms are similar. Kocamustafaogullari and Ishii [42] proposed the following formulation for bubble number density coalescence rate,

$$S(V) = \int_{V_{\min}}^{V/2} \lambda(V - V', V')h(V - V', V')f(V - V')f(V')dV' , \quad (3.13)$$

where:

$$\begin{aligned} \lambda(V - V', V') &\equiv \text{coalescence efficiency of bubbles of volume } V - V' \text{ and } V' , \\ h(V - V', V') &\equiv \text{coalescence frequency of bubbles of volume } V - V' \text{ and } V' , \\ f(V - V') &\equiv \text{number density distribution of bubbles of volume } V - V' \text{ or } V' . \end{aligned}$$

Similarly the break-up rate is formulated as,

$$S(V) = \int_V^{V_{\max}} \beta(V', V)n(V')g(V')f(V')dV' , \quad (3.14)$$

where:

$$\begin{aligned} \beta(V', V) &\equiv \text{distribution of daughter bubbles from parent bubble } V' , \\ n(V') &\equiv \text{number of daughter bubbles produced from parent bubble } V' , \\ g(V') &\equiv \text{break-up frequency of bubble having volume } V' . \end{aligned}$$

With the above definitions, expressions for the coalescence/break-up kernels need to be formulated in order to close the two-group IATE model. Unlike the one-group formulation where only one interaction per mechanism is possible (e.g. random collision, wake entrainment, etc.), several interactions per mechanism are possible in the two-group model. The possible interaction mechanisms are outlined graphically in Fig. 3.2.

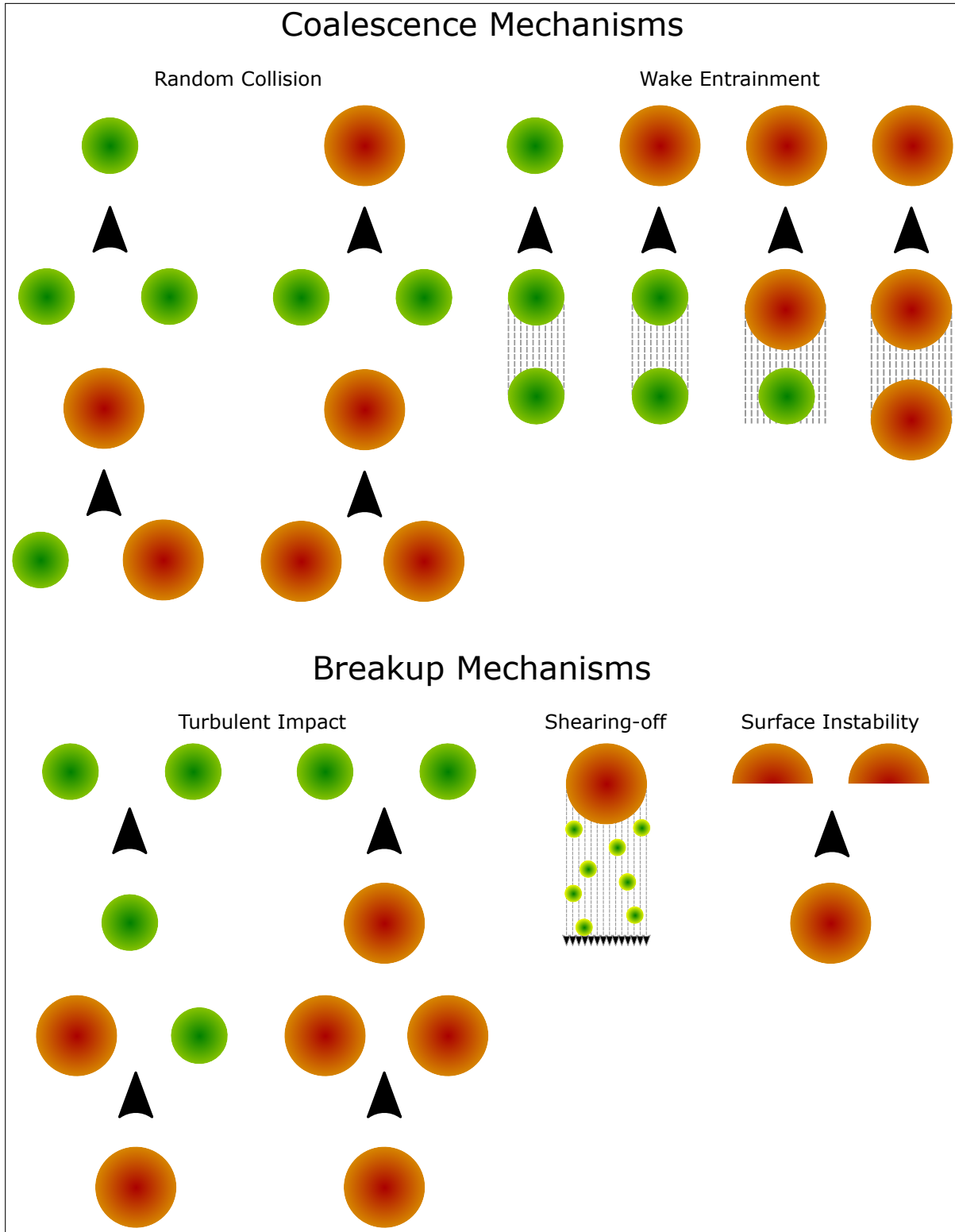


Figure 3.2: A diagram of various interaction mechanisms that are considered in the two-group model. Vertical orientation indicates the upstream position of bubbles during the interaction. Green bubbles belong to group-1 and orange bubbles belong to group-2.

3.2 Experimental Database

The experimental database is obtained from the TOPFLOW facility at the Helmholtz-Zentrum Dresden-Rossendorf [8, 60], and is based on the employment of wire-mesh sensors for the characterization of two-phase flow parameters. The TOPFLOW facility has a vertical 8.0 m long, 52.3 mm and 195.3 mm diameter test section. A visual of the TOPFLOW facility test section is presented in Fig. 3.3. The small diameter test section is referred to as ‘DN50’, while the larger test section is referred to as ‘DN200’.

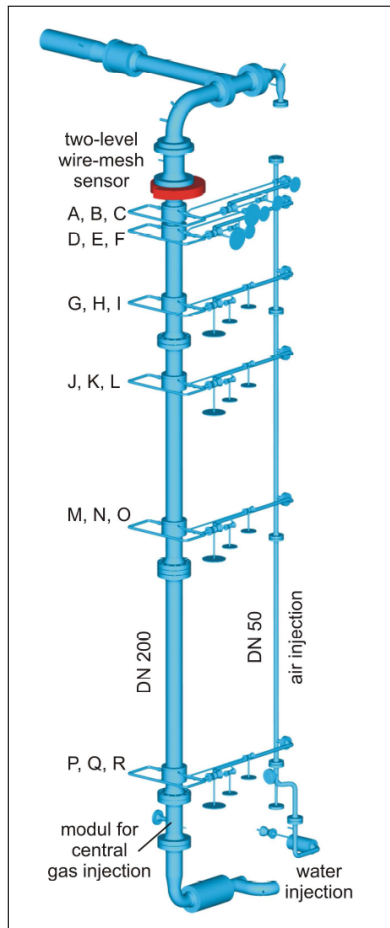


Figure 3.3: A visual of the TOPFLOW DN50 and DN200 test sections [8].

3.2.1 TOPFLOW DN50

The DN50 test section includes a gas sparger located at the center of the test section entrance and is characterized by eight isotropically distributed 4 mm orifices. Wire-mesh sensor measurements are performed at four axial locations downstream of the gas injection, namely at

1.91, 30.6, 59.3, and 151 L/D respectively. In this way, the axial development of the air-water flow over 8.0 m can be experimentally characterized. The rate at which both air and liquid are injected can be varied, allowing measurements to be performed over all possible flow regimes encountered in a vertical pipe. Table 3.2 presents the experimental test matrix of available data and the corresponding flow regimes observed. The DN50 test section is fitted with a 16 by 16 array wire-mesh sensor with a spatial resolution of 3.2 mm that is operated at a frequency of 2.5 kHz.

Table 3.2: Experimental test matrix for the DN50 TOPFLOW tests. Tests that have been executed and have available data are colored. The colors indicate flow regime.

		Superficial gas velocity [m/s]																
		0.0025	0.0040	0.0062	0.0096	0.0151	0.0235	0.0368	0.0574	0.0898	0.140	0.219	0.342	0.534	0.835	1.305	2.038	
Superficial liquid velocity [m/s]	4.047	11	22	33	44	55	66	77	88	99	110	121	132	143	154	165	176	
	2.554	10	21	32	43	54	65	76	87	98	109	120	131	142	153	164	175	
	1.611	9	20	31	42	53	64	75	86	97	108	119	130	141	152	163	174	
	1.017	8	19	30	41	52	63	74	85	96	107	118	129	140	151	162	173	
	0.641	7	18	29	40	51	62	73	84	95	106	117	128	139	150	161	172	
	0.405	6	17	28	39	50	61	72	83	94	105	116	127	138	149	160	171	
	0.255	5	16	27	38	49	60	71	82	93	104	115	126	137	148	159	170	
	0.161	4	15	26	37	48	59	70	81	92	103	114	125	136	147	158	169	
	0.102	3	14	25	36	47	58	69	80	91	102	113	124	135	146	157	168	
	0.0641	2	13	24	35	46	57	68	79	90	101	112	123	134	145	156	167	
	0.0405	1	12	23	34	45	56	67	78	89	100	111	122	133	144	155	166	
			Bubbly Flow								Slug Flow							

3.2.2 TOPFLOW DN200

The larger DN200 is a 195.3 mm diameter test section which is characterized by a fixed measurement location for the wire-mesh sensor, mounted at the exit of the DN200 vertical pipe (in DN50 the wire-mesh sensor was moved to various L/D for new axial measurements). The DN200 wire-mesh sensor is a 64 by 64 array with a spatial resolution of 3.0 mm that is operated at a frequency of 2.5 kHz).

Six air injection hubs are located upstream of the WMS, at a distance of 1.1, 2.5, 7.4, 12.7, 22.6 and 39.4 L/D, respectively. Each hub consists of three discs, which can be operated independently, each presenting a series of orifices uniformly distributed along the pipe circumference. Two of the discs that have 1 mm injection orifices (located at the top and

bottom of each hub), while the middle disc that has 4 mm injection orifices. In this way, experiments characterized by different initial bubble size distributions can be carried out. Each disc is able to operate individually or in conjunction with others. In the present dissertation only the data using the 1 mm injection hubs are presented. The absolute pressure at the air injection is set at 0.25 MPa. By varying the injection location with respect to the WMS, the evolution of the air-water flow along the 8.0 m vertical pipe can be characterized. As for the DN50 experiments, the rate at which both air and water are injected can be varied over a wide range of flow conditions. Table 3.3 presents the experimental test matrix for available data and the corresponding flow regimes observed.

Table 3.3: Experimental test matrix for the DN200 TOPFLOW tests. Tests that have been executed and have available data are colored. The colors indicate flow regime.

		Superficial gas velocity [m/s]															
		0.0025	0.0040	0.0062	0.0096	0.0151	0.0235	0.0368	0.0574	0.0898	0.140	0.219	0.342	0.534	0.835	1.305	2.038
Superficial liquid velocity [m/s]	4.047	11	22	33	44	55	66	77	88	99	110	121	132	143	154	165	176
	2.554	10	21	32	43	54	65	76	87	98	109	120	131	142	153	164	175
	1.611	9	20	31	42	53	64	75	86	97	108	119	130	141	152	163	174
	1.017	8	19	30	41	52	63	74	85	96	107	118	129	140	151	162	173
	0.641	7	18	29	40	51	62	73	84	95	106	117	128	139	150	161	172
	0.405	6	17	28	39	50	61	72	83	94	105	116	127	138	149	160	171
	0.255	5	16	27	38	49	60	71	82	93	104	115	126	137	148	159	170
	0.161	4	15	26	37	48	59	70	81	92	103	114	125	136	147	158	169
	0.102	3	14	25	36	47	58	69	80	91	102	113	124	135	146	157	168
	0.0641	2	13	24	35	46	57	68	79	90	101	112	123	134	145	156	167
	0.0405	1	12	23	34	45	56	67	78	89	100	111	122	133	144	155	166
		Bubbly Flow					Churn-turbulent Flow					Annular Flow					

3.2.3 Application of TOPFLOW Data

The following sections assess the performance of the Fu-Ishii (Section 3.3) and Smith-Schlegel (Section 3.4) two-group interfacial area transport equation models against TOPFLOW data. In a system code, the model would be implemented coupled to a two-fluid model. In this case, however, the IATE solution is affected by the uncertainty of the two-fluid model predictions of void-fraction and bubble velocities. To have a sound assessment of the prediction of IATE models, in the present work, the field variables required to close the IATE model are interpolated from experimental data. In particular, the void fraction and bubble velocities measured at different axial locations in the respective pipes are interpolated and directly used

for the solution of the interfacial area transport equations. The IATE model performance for several flow conditions is evaluated using the error estimator defined by

$$\delta(x) \equiv \frac{1}{N-1} \sum_{n=2}^N \left| \frac{x_{n,calc} - x_{n,meas}}{x_{n,meas}} \right|, \quad (3.15)$$

where $x_{n,meas}$ is a quantity of interest measured at the n -th axial location, and $x_{n,calc}$ is the corresponding computed variable using the IATE model.

3.3 Fu-Ishii Model

The Fu-Ishii model has been developed for bubbly, slug, and churn-turbulent flows in small diameter vertical pipes. The mechanistic modelling of the Fu-Ishii model is detailed by Fu [22]. The evaluation of closure terms in the model were conducted for a 50.8 mm pipe at Purdue University [23]. The next section will summarize the principles behind mechanisms considered (forgoing a thorough derivation). Section 3.3.2 will discuss key results of validating the Fu-Ishii model against TOPFLOW DN50 (Section 3.2.1) experimental data.

3.3.1 Interaction Mechanisms

The Fu-Ishii model considers several interaction mechanisms that are summarized in Table 3.4. In order to group all possible interactions, experimental observations were used to determine if specific intergroup interactions dominate. In particular, wake entrainment and shearing-off accounted for the most number of intergroup interactions. For group-2, the wake entrainment between group-2 bubbles ($\phi_{WE}^{(2)}$) governed its population. The surface instability mechanism was found to be insignificant and was therefore absorbed into the turbulent impact mechanism for group-2 ($\phi_{TI}^{(2)}$). The random collision of group-1 bubbles into group-2 bubbles was small and absorbed into the wake entrainment ($\phi_{WE}^{(12,2)}$) due to their similar nature. Random collision of two group-2 bubbles was negligible due to the small pipe diameter. Additionally, the distribution parameter χ is set to zero, as few bubbles are expected to transfer across groups simply due to expansion.

In order to assess Eqs. (3.13) and (3.14), assumptions regarding the bubble size distribution are proposed. The assumptions in the Fu-Ishii model are reflected by Fig. 3.4. Bubbles are classified into three separate categories. Group-1 bubbles have $V_{1,min} \leq V \leq V_{1,max}$. Cap bubbles have $V_{c,min} \leq V \leq V_{c,max}$, and slug bubbles have $V_{c,max} = V_{s,min} < V \leq V_{s,max}$. Both cap and slug bubbles belong to group-2 and have a number distribution of f_c and f_s , respectively. In order to simplify modelling, it is assumed that $f_c = f_s$, and any deviation from

Table 3.4: List of various interaction mechanisms accounted for in the Fu-Ishii model. All parameters used by the model are listed in the last column [32, Ch. 11].

Symbols	Mechanisms	Interaction	Parameters
$\phi_{RC}^{(1)}$	Random collision	(1)+(1)→(1)	$C_{RC} = 0.0041, C_T = 3.0$
$\phi_{RC}^{(11,2)}$	Random collision	(1)+(1)→(2)	$\alpha_{1,max} = 0.75$
$\phi_{WE}^{(1)}$	Wake Entrainment	(1)+(1)→(1)	$C_{WE} = 0.002, C_{WE}^{12,2} = 0.015$
$\phi_{WE}^{(11,2)}$	Wake Entrainment	(1)+(1)→(2)	$C_{WE}^{(2)} = 10.0$
$\phi_{WE}^{(12,2)}$	Wake Entrainment	(1)+(2)→(2)	$C_{TI} = 0.0085, W_{e,crit} = 6.0$
$\phi_{WE}^{(2)}$	Wake Entrainment	(2)+(2)→(2)	$C_{SO} = 0.031, \gamma_{SO} = 0.032$
$\phi_{TI}^{(1)}$	Turbulent Impact	(1)→(1)+(1)	$\beta_{SO} = 1.6$
$\phi_{TI}^{(2)}$	Turbulent Impact	(2)→(2)+(2)	
$\phi_{SO}^{(2,12)}$	Shearing-off	(2)→(1)+(2)	

the real bubble size distribution is considered to manifest in an adjustment of empirically determined coefficients. Therefore, two number density distribution values are used in the mechanistic modelling; one for each bubble group.

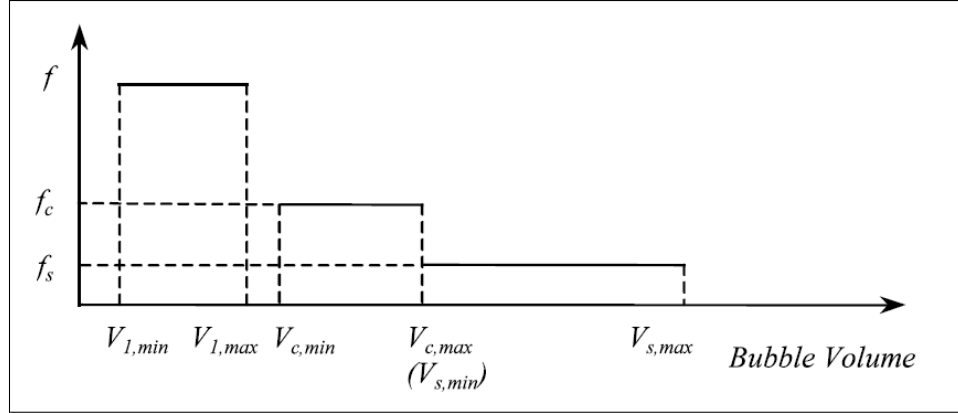


Figure 3.4: Assumption of bubble population distributions in Fu-Ishii model [22].

3.3.1.1 Random Collision

Coalescence due to random collisions is driven by random motions driven by turbulent eddies. Wu [82] estimated the collision frequency by relating the mean distance between collisions and the turbulent fluctuation velocity. The expression for the coalescence rate is,

$$R_{RC}^{(1)} = C_{RC} \left[\frac{u_t n_1^2 D_{sm1}^2}{\alpha_{1,max}^{1/3} (\alpha_{1,max}^{1/3} - \alpha_1^{1/3})} \right] \left[1 - \exp \left(-C \frac{\alpha_{1,max}^{1/3} \alpha_1^{1/3}}{\alpha_{1,max}^{1/3} - \alpha_1^{1/3}} \right) \right], \quad (3.16)$$

where the group-1 number density, $n_1 = a_{i1}^3 / (36\pi\alpha_1^2)$. The interfacial area sink rates are defined as

$$\phi_{RC}^{(1)} = \langle \delta A_{i1}^{(11,1)} \rangle R_{RC}^{(1)} , \quad (3.17)$$

$$\phi_{RC}^{(11,2)} = \langle \delta A_{i1}^{(11,2)} \rangle R_{RC}^{(1)} , \quad (3.18)$$

where $\langle \delta A \rangle$ represents a change in surface area due to an assumed binary interaction between two bubbles; the shape of the bubble is assumed in order to develop an explicit formulation.

3.3.1.2 Wake Entrainment

Wake entrainment is a coalescence mechanism with four different groups of interactions accounted for in the Fu-Ishii model.

Group 1 wake entrainment

This interaction considers the coalescence of among two group-1 bubbles. It is modelled by considering the average time required for trailing bubbles inside a wake region to collide. This mechanism was adapted from the one-group formulation by Wu [82]. The group-1 coalescence rate due to wake entrainment is

$$R_{WE}^{(1)} = C_{WE}^{(1)} C_D^{1/3} n_1^2 D_{sm1}^2 v_{r1} , \quad (3.19)$$

where $C_{WE}^{(1)}$ is an empirically determined coefficient. The drag coefficient, C_D , and the relative velocity, v_{r1} , was modelled by Ishii and Chawla [31]. The formulation for $R_{WE}^{(1)}$ is used to model both $\phi_{WE}^{(1)}$ and $\phi_{WE}^{(11,2)}$:

$$\phi_{WE}^{(1)} = \langle \delta A_{i1}^{(11,1)} \rangle R_{WE}^{(1)} , \quad (3.20)$$

$$\phi_{WE,1}^{(11,2)} = \langle \delta A_{i1}^{(11,2)} \rangle R_{WE}^{(1)} , \quad (3.21)$$

$$\phi_{WE,2}^{(11,2)} = \langle \delta A_{i2}^{(11,2)} \rangle R_{WE}^{(1)} . \quad (3.22)$$

Group 1 into 2 wake entrainment

Group-1 bubbles can swarm in the wake region of the larger group-2 bubbles and eventually coalesce. The small bubbles experience rapid velocity fluctuation due to the high turbulence intensity generated in the wake of the larger bubble. Fernandes [20] proposed that the coalescence frequency of group-1 bubbles into the rear of leading group-2 bubbles is proportional

to wake turbulence intensity and area of the slug tail,

$$\lambda h(V - V', V') \propto A_c \cdot \bar{u}'_t . \quad (3.23)$$

The turbulence intensity has been related to the relative liquid film velocity by Schlichting [68] as $\bar{u}'_t \approx (1/4)v_r$. Thus,

$$\lambda h(V - V', V') \propto \frac{\pi}{4} D^2 \cdot \frac{1}{4} v_r . \quad (3.24)$$

The corresponding change to group-1 and group-2 interfacial area concentration is:

$$\phi_{WE,1}^{(12,2)} = -C_{WE}^{(12,2)} \pi \left(\frac{2g\Delta\rho}{\rho_f} \right)^{1/2} D^{1/2} V_s^{*1/2} \frac{\alpha_1 \alpha_2}{1 - \alpha_2} \kappa_{fr} \left(\frac{3}{D_{sm1}} \right) , \quad (3.25)$$

$$\phi_{WE,2}^{(12,2)} = C_{WE}^{(12,2)} \pi \left(\frac{2g\Delta\rho}{\rho_f} \right)^{1/2} D^{1/2} V_s^{*1/2} \frac{\alpha_1 \alpha_2}{1 - \alpha_2} \kappa_{fr} \left(\frac{2}{D\alpha_m^{1/2}} \right) , \quad (3.26)$$

where κ_{fr} is a coefficient determining the liquid film velocity reduction due to friction [22].

Group 2 wake entrainment

The wake entrainment of group-2 bubbles is expected to dominate. The interaction occurs when a group-2 bubble forms a wake as it advects upwards. If a trailing group-2 bubble is within a critical distance, it may accelerate towards the leading bubble and cause coalescence to occur. The critical distance was identified by Dukler [16]. With reference to Fig. 3.5, the rise velocity of the trailing bubble remains constant until it comes to within $2D$, and begins accelerating towards the leading bubble. No theoretical formulation for the rise velocity exists due to a lack of understanding of the complex fluid-dynamics in the wake region. Empirical correlations are used instead.

The rise velocity for a slug bubble was developed by Moissis and Griffith [52], from which the average time required for coalescence to occur can be estimated - leading to an approximation for the collision frequency. Based on Eq. (3.13), the entrainment rate between group two bubbles is represented by

$$S_{WE}^{(2,2)}(V) = \int_{V_{c,\min}}^{V_{s,\max}/2} h(V - V', V') f_{2L}(V - V') f_{2T}(V') dV' , \quad (3.27)$$

where f_{2T} and f_{2L} are the leading and trailing density distributions respectively, and h is the collision frequency. In order to proceed further, the interaction is simplified as a binary process, and thus $f_{2T} \approx f_2$. The possibility of entrainment is experimentally shown to follow

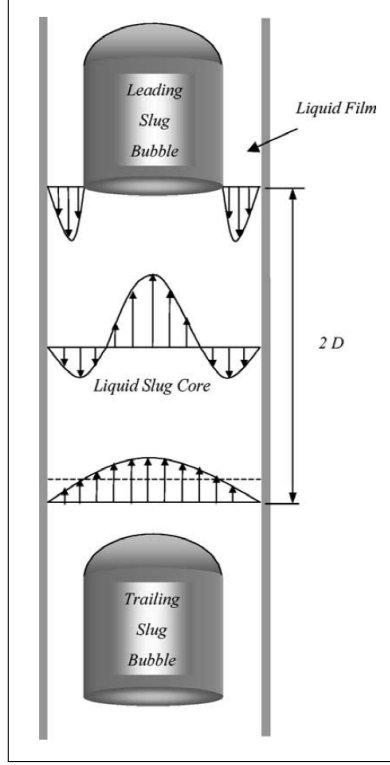


Figure 3.5: Wake entrainment of large group-2 bubbles [22].

a Poisson distribution. Thus, the probability of having a trailing bubble is modelled after a Poisson process, $f_{2L} \approx f_{2T}^{\text{Poisson}}$. The entrainment rate is simplified,

$$S_{WE}^{(2,2)}(V) \approx \int_{V_{2,\min}}^{V_{2,\max}} h(V - V', V') f_2 f_{2T}^{\text{Poisson}} dV', \quad (3.28)$$

and is integrated over the entire group-2 bubble population to determine the sink rate of group-2 bubbles due to wake entrainment [22]:

$$\begin{aligned} \phi_{WE}^{(2)} = & -10.24 C_{WE}^{(2)} D^{3/2} \alpha_2 \left[1 - \exp\left(\frac{-2331 \alpha_2 V_s^{*2}}{D^5}\right) \right] \times \\ & \times \left[\exp\left(\frac{0.06 C_l (\alpha_{2m}/\alpha_2 - 1)}{V_s^*}\right) - 1 \right]^{-1}. \end{aligned} \quad (3.29)$$

A coefficient, $C_{WE}^{(2)}$, is introduced to adjust the rate of wake entrainment. This coefficient will need to be evaluated experimentally. In Eq. (3.29), V_s^* represents the ratio of maximum to minimum slug volume, α_{2m} represents the maximum possible group-2 void fraction (determined to be 0.81 experimentally), and C_l is a coefficient used in modelling collision frequency (determined to be 0.1).

3.3.1.3 Turbulent Impact

Group 1 turbulent impact

This mechanism predominantly occurs for bubbly flows at high superficial velocities. The modelling of group-1 breakup by turbulent eddies is adopted through the one-group formulation by Wu [82]. The turbulent impact source is

$$\phi_{TI}^{(1)} = C_{TI} \left(\frac{\bar{u}_t' a_{i1}^2}{\alpha_1} \right) \exp \left(-\frac{We_{cr}}{We} \right) \left(1 - \frac{We_{cr}}{We} \right)^{1/2} \quad \text{when } We > We_{cr}, \quad (3.30)$$

where the Weber number is defined as,

$$We = \frac{\rho_f u_t^2 D_{sm1}}{\sigma}, \quad (3.31)$$

and where u_t is the turbulent fluctuation velocity that is determined by both isotropic turbulence and turbulence caused by wall jets formed by movement of large slug bubbles. C_{TI} is an empirically determined coefficient. The Weber number represents a ratio of the inertial and surface-tension-induced pressures. The critical Weber number, We_{cr} , determines the occurrence of a bubble disintegration (and therefore imposes a conditional occurrence of the turbulent impact mechanism for group-1).

Group 2 turbulent impact

Breakup of larger bubbles by turbulent eddies are thought to occur most in slug or churn-turbulent flows. The maximum size of a cap bubble is given by Ishii and Kojasoy [35] as

$$D_{s,\max} = 40 \sqrt{\frac{\sigma}{g\Delta\rho}}, \quad (3.32)$$

which is approximately 100 mm for air-water flows. When bubbles sizes are above this limit, they are subject to surface instability and breakup. Therefore, when pipes are smaller than this diameter, it is expected that cap/slug bubbles are able to sustain their shape. Therefore, the breakup of these larger bubbles is associated with impact of turbulent eddies upon the leading surface during advection. Only sufficiently large eddies will cause this breakup to occur. The frequency of collision is expressed as

$$h(V, d_e) \propto \frac{v_{re}}{V_B}, \quad (3.33)$$

where d_e is the eddy length scale, v_{re} is the relative velocity between the eddy and the bubble, and V_B is the volume available for collision. The total break up rate is then expressed as

$$S_{TI}^{(2)}(V) = \int_{d_e}^{D_{e,\max}} h(V, d_e) f_2(V) f_e(d_e) dd_e, \quad (3.34)$$

where $D_{e,\max}$ is the maximum eddy size. D_e , the lower limit, is taken as the critical bubble diameter, D_c , Eq. (3.1). The resulting expression is

$$\begin{aligned} \phi_{TI}^{(2)} = & C_{TI}^{(2)} \frac{\alpha_2 \varepsilon^{1/3} V_s^*}{D} \frac{1 - \alpha_g}{1 - \alpha_2} \left[1 - \left(\frac{D_c}{\alpha_{2m}^{1/2} D} \right)^{5/3} \right] \times \\ & \times \left[14.38 + 1.57 \alpha_{2m}^{-2/3} \left(\frac{D_c}{D} \right)^{4/3} - 15.95 \alpha_{2m}^{-1/6} \left(\frac{D_c}{D} \right)^{1/3} \right], \end{aligned} \quad (3.35)$$

where an empirically determined constant $C_{TI}^{(2)}$ is introduced. The turbulence dissipation rate, ε , is determined using a two-phase friction factor, f_{TW} , and the average mixture velocity v_m [31], $\varepsilon = f_{TW} v_m^3 / 2D$.

3.3.1.4 Shearing-off

The shearing-off mechanism occurs for large bubbles (cap/slug) that form a skirt as they advect. In highly viscous flows, it is postulated that turbulence about the edge of the skirt overcomes the local surface tension and causes small bubbles to form. However, for air-water flows, the shear effects tend to be negligible due to the low viscosity of water [22]. An alternative mechanism is suggested whereby the bulk velocity inside the large bubble structures is significantly higher than the velocity at the liquid-gas interface. Towards the skirt of the bubble, the local gas penetrates into the film forming smaller bubbles. The thickness of the boundary penetrating boundary layer is estimated by turbulent gas flow over a flat plate by Schlichting [68] (δ_{eff} in Fig. 3.6). The sheared-off bubble size (d_s) is estimated through studies of plunging liquid jets [19, 10]. Estimating the total sheared-off volume and the size of sheared off bubbles allows a formulation for the generation rate:

$$S_{SO}^{(2,1)}(V) \propto f_2(V) \frac{\pi D_C \delta_{eff} v_r}{\pi d_s^3 / 6}, \quad (3.36)$$

$$\phi_{SO,1}^{(2,1)} = 0.5257 C_{SO} \alpha_2 v_g^{1/5} \left(\frac{\rho_f}{We_c \sigma D} \right)^{3/5} \left(\frac{2g\Delta\rho}{\rho_f} \right) V_s^{*-4/5} \xi_{SO} (1 - 0.667 \kappa_{bl}) \kappa_{fr}^2, \quad (3.37)$$

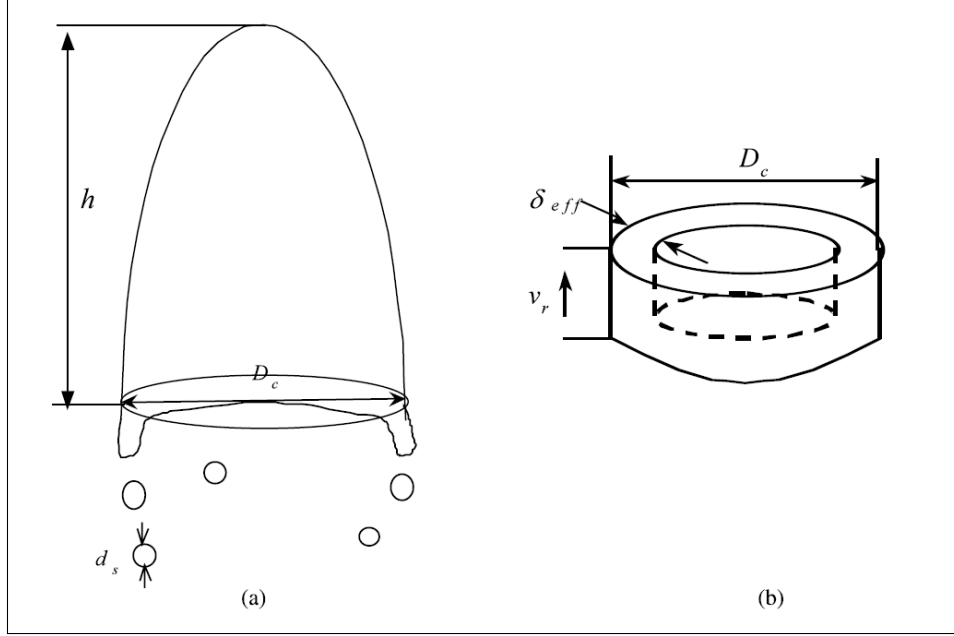


Figure 3.6: Assumed geometry for modelling shearing-off (a) and volume of gas sheared off (b) [22].

$$\phi_{SO,1}^{(2,1)} = -4.4332C_{SO}\alpha_2v_g^{1/5}D^{-9/5}\alpha_{2m}^{1/2}\left(\frac{2g\Delta\rho}{\rho_f}\right)^{2/5}V_s^{*-1/5}(1 - 0.667\kappa_{bl})\kappa_{fr}^{4/5}, \quad (3.38)$$

where κ_{bl} is a factor affecting boundary layer profile, and C_{SO} is, again, a coefficient that is determined experimentally.

3.3.2 Evaluation

The performance of Fu-Ishii two-group IATE model is evaluated against the TOPFLOW DN50 experimental database (Section 3.2.1). An overview of the IATE performance is presented in Section 3.3.2.1, highlighting flow conditions that challenge the model. A detailed discussion of mechanisms that contribute to successful and poor performance of IATE is given in Section 3.3.2.2. Finally, the performance of the IATE model coupled to a two-fluid 6-equation code (TRACE) is analyzed in Section 3.3.2.3. The regime maps used have been adapted from the studies by Mishima and Ishii [51], presented in Fig. 3.7.

3.3.2.1 Overview of Performance

In order to provide a holistic assessment of IATE performance, the error in predicting interfacial area concentration, calculated using Eq. (3.15), is presented for the entire DN50 TOPFLOW database in Fig. 3.8. In the figure, the error in prediction of group-1, group-2 and total interfacial area are presented separately. Tests that have no large group-2 bubbles

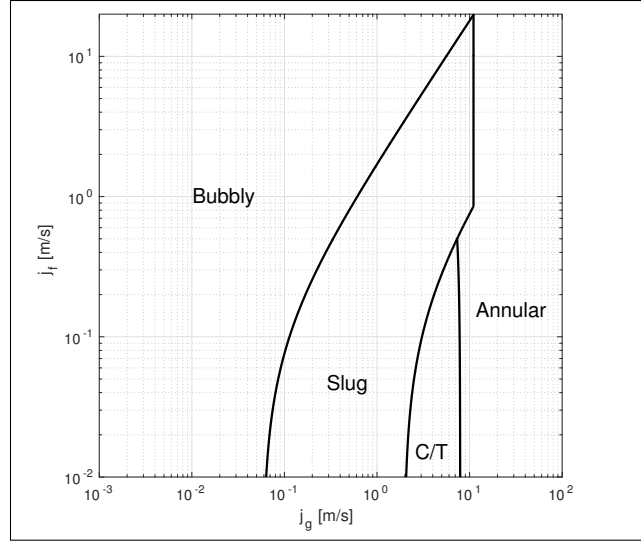


Figure 3.7: Anticipated flow regimes in DN50 TOPFLOW tests.

are omitted in presentation of group-2 error. The prediction of group 1 a_i is generally good in the bubbly flow regime and deteriorates towards the slug flow regime. A similar trend is noted for group-2 a_i error, however, the magnitude is significantly higher, with most cases being well above 80%. The error for the prediction of total a_i follows a similar qualitative trend. Due to the poor performance of group-2 a_i in the slug flow regime, the error in total a_i can be larger than $> 30\%$.

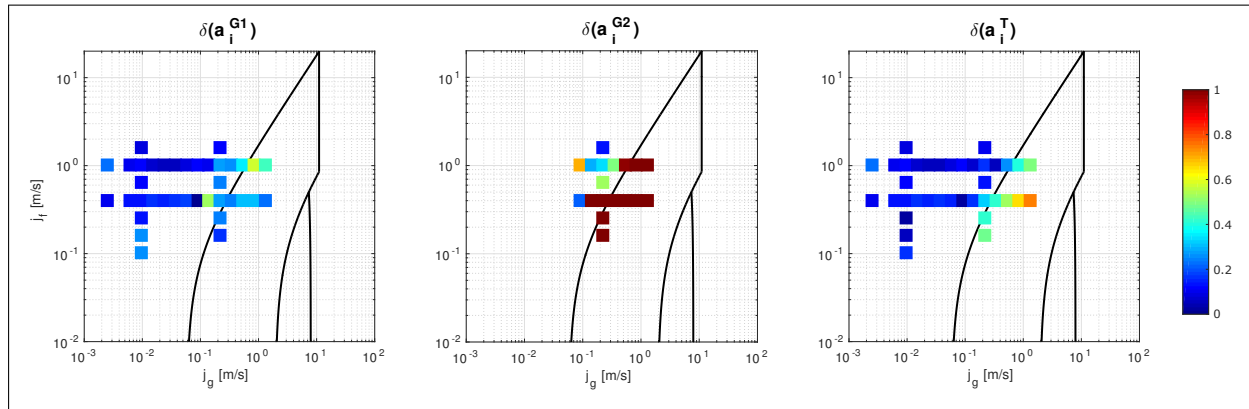


Figure 3.8: A comparison of performance for DN50 TOPFLOW data. Left column indicates error for group 1 interfacial area concentration and right column indicates error for group 2 interfacial area concentration. The third column indicates error for prediction of total interfacial area.

It can be concluded that, in general, the IATE model struggles in high void fraction regimes. The propagation of group-2 a_i is incorrect in the majority of the tests. For group-1, further investigation is necessary to determine the impact of varying superficial velocities on

the incidence of interaction mechanisms. Isolating sources of error may provide insight into how to improve IATE performance.

3.3.2.2 Discussion

Detailed comparison of the IATE models against experimental data is presented for selected tests in Figures 3.9 to 3.12. In the figures, the results of the IATE model are indicated with continuous lines, the experimental values are indicated with cross symbols. Group-1 interfacial area and void fractions values are reported in red, group-2 values in blue, and total in black. Cumulative source term contributions from IATE interaction mechanisms (ϕ_{j1} , ϕ_{j2}) are also presented. To provide further insight, the experimental axial development of bubble size distributions is also reported.

At low superficial gas and liquid velocities, the flow is strictly in the bubbly flow regime. The results for Test 30, corresponding to the bubbly flow regime, is presented in Fig. 3.9. The qualitative propagation of the interfacial area concentration, a_i , is good. Quantitatively, the a_i predicted downstream is within the $\pm 10\%$ measurement uncertainty. No large group-2 bubbles are present in these conditions. The group-1 bubble interaction mechanism source terms are negligible, as indicated by their absence in Δa_i^{G1} . The dominating source term is the group-1 bubble expansion term (first term on the right hand side of Eq. (3.11)). In steady state adiabatic air-water flows this term simplifies to

$$\phi_{EXP} = \frac{2}{3} \left(\frac{a_i}{\alpha_g} \right) \nabla \cdot (\alpha \vec{v}_g) . \quad (3.39)$$

The bubble expansion term relies on good prediction of void fraction and gas phase velocity. As both these field values are directly interpolated from experimental data, the predicted a_i value is expected to be accurate. This result suggests that for simple volumetric expansion and no bubble interaction mechanisms, the dynamics of two-phase flow is correctly captured. The bubble size distribution does not change significantly along the axis of the pipe. The width of the distribution contracts at 59 L/D then shifts towards higher diameters at 151 L/D – further supporting the predicted propagation of bubble expansion.

Test 94, presented in Fig. 3.10, corresponds to moderate superficial gas and liquid velocities, and is close to the transition to slug flow regime. In this regime, both group-1 and group-2 bubbles are present in the flow and several bubble interaction mechanisms play a role in the propagation of the interfacial area concentration. The IATE model accurately predicts propagation of both group-1 and group-2 a_i values. The development of the bubble size distribution for group-1 tends to spread towards smaller bubble sizes and accounts for a majority of the entire bubble population. This indicates that break-up should be a dominant

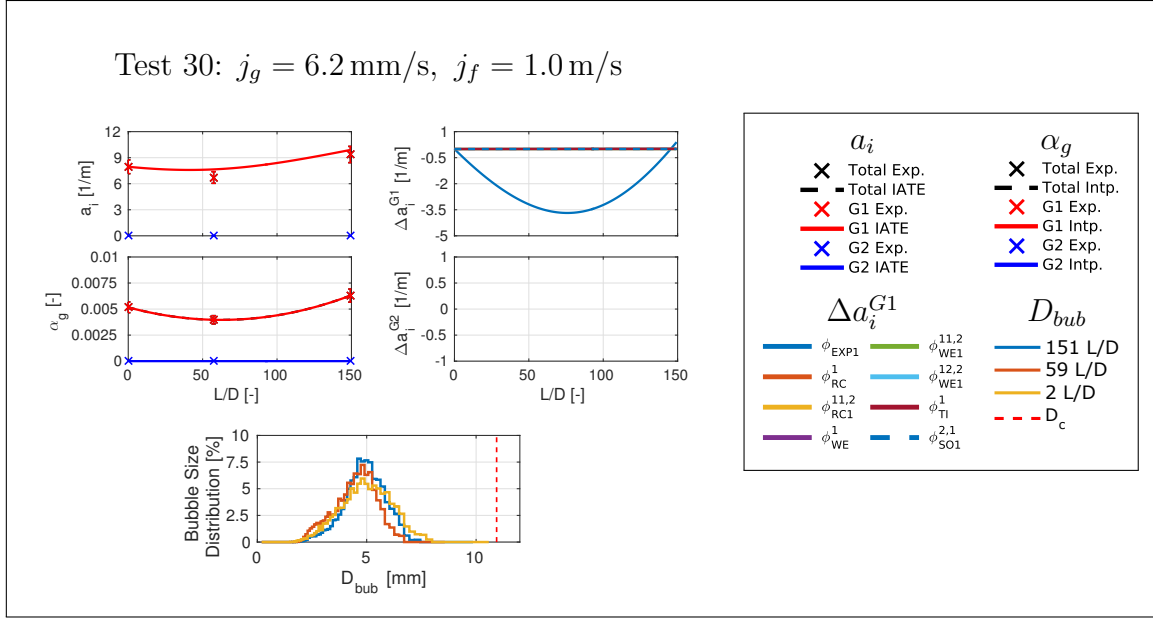


Figure 3.9: Results for Test 30 using the 2G IATE model.

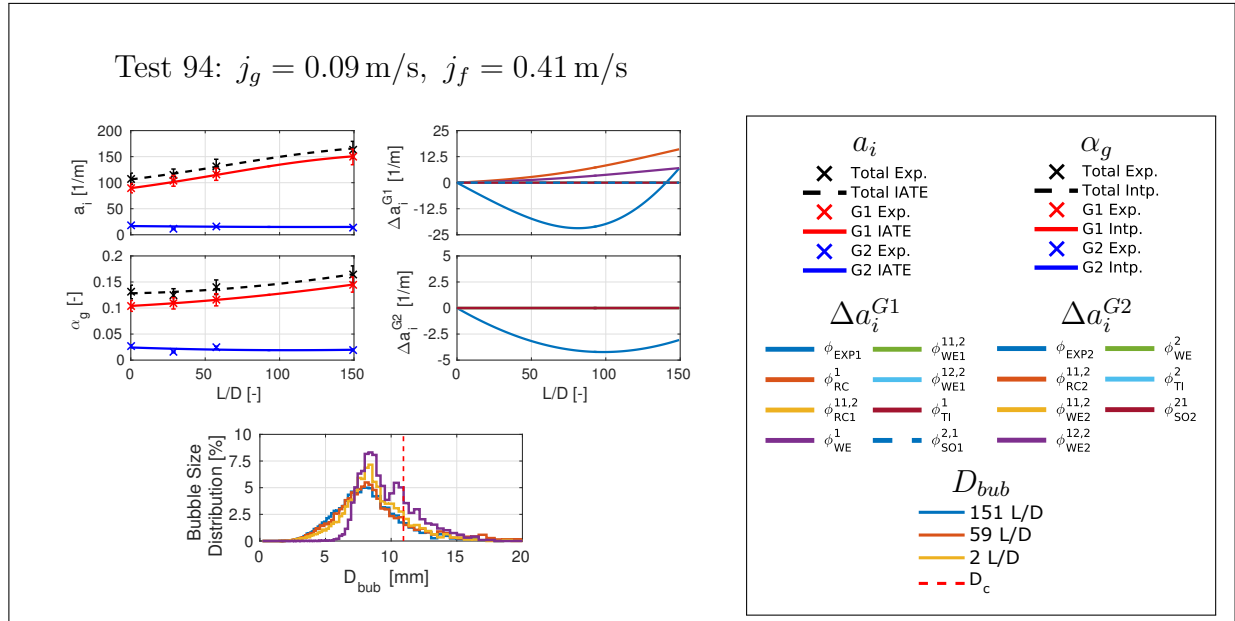


Figure 3.10: Results for Test 94 using the 2G IATE model.

ing mechanism for group-1 bubbles and a greater fraction of total a_i should be accounted for by smaller bubbles. For group-2, little change is noted in the shape of the bubble size distribution, indicating a relatively neutral a_i propagation. This is consistent with the evolution of a_i for group-2 shown in Fig. 3.10.

As discussed in discussed in Section 3.3.2.1, the IATE performance increasingly deteriorates when approaching the transition to slug flow regime. To gain more insight in the reasons

of the performance deterioration, Tests 115 to 119 corresponding to a constant $j_g = 0.22$ m/s and varying superficial liquid velocities are presented in . Fig. 3.11. For $j_f = 1.6$ m/s, the group-wise a_i values are predicted well. As noted in previous successful tests, the bubble expansion is the major source/sink – further supported by the experimental bubble size development.

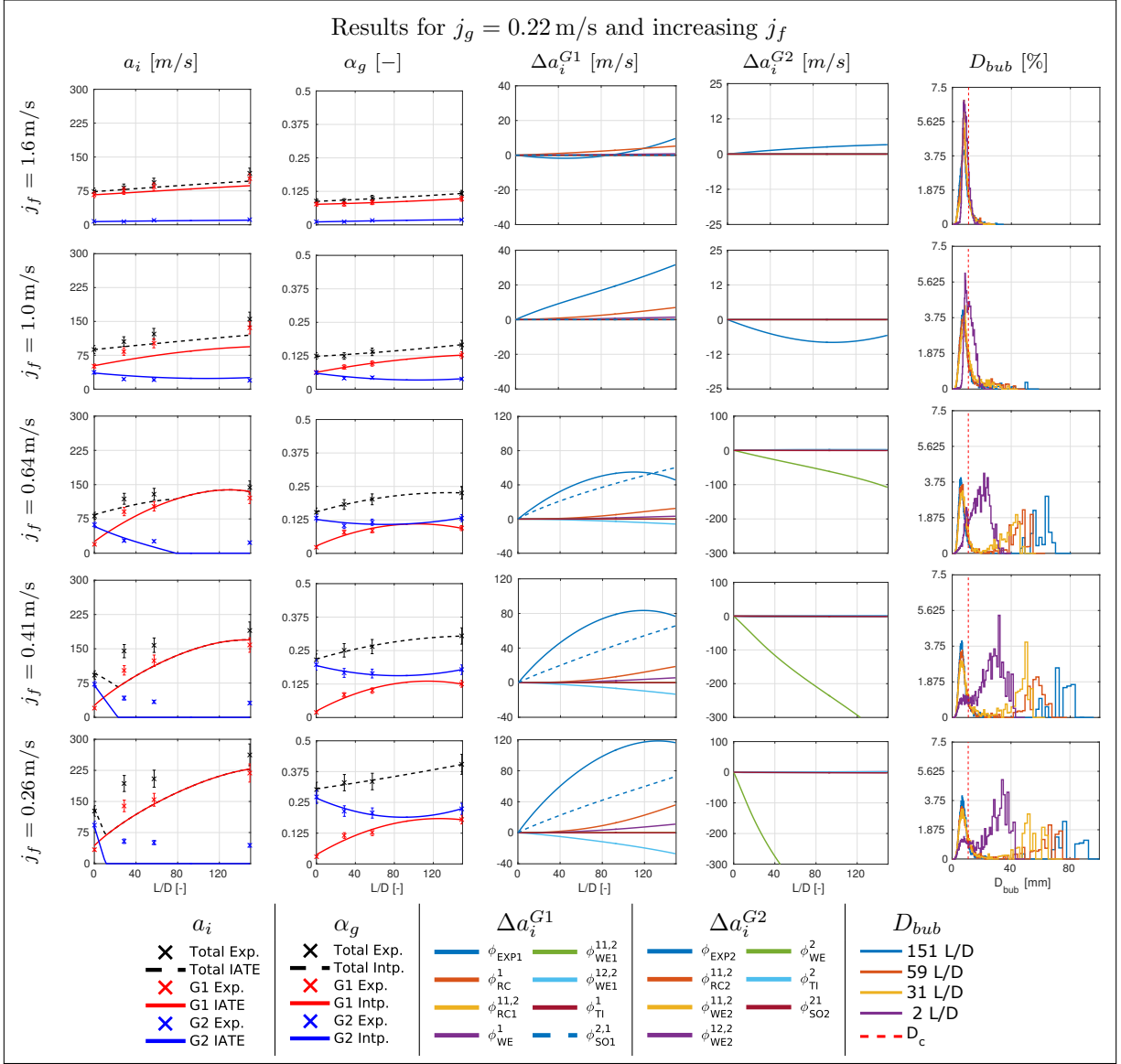


Figure 3.11: Results for Tests 115 to 119 using the 2G IATE model.

At $j_f \leq 0.64$ m/s, there are several interaction mechanisms that are invoked for group 1 a_i transport. The summation of the interaction mechanisms $\phi_{SO1}^{2,1}$, ϕ_{RC}^1 , ϕ_{WE}^1 , $\phi_{WE1}^{12,2}$ together with bubble expansion results in a successful prediction of group 1 a_i both qualitatively and quantitatively. Meanwhile, the propagation of group 2 a_i is dominated by a single interaction

mechanism, ϕ_{WE}^2 – the wake entrainment of group-2 bubbles. The ϕ_{WE}^2 term causes a strong over-prediction of group 2 bubble coalescence and nullifies its a_i value. The experimental bubble size distribution of group-2 bubbles ($D_{bub} > D_c$) tends to smear and increase in mean value to higher diameters; this indicates that there may indeed be significant coalescence occurring among group-2 bubbles.

The $j_f = 1.0$ m/s test has been neglected in the discussion above. The test has interesting implications as it only has bubble expansion as dominating a_i source/sink yet achieves poor quantitative prediction. This result is in contrast to the tests discussed thus far. This may be indicative of IATE failing to completely capture the transition from a j_g-j_f space that is purely pressure-head driven to regimes involving a combination of bubble expansion and bubble interaction mechanisms.

The wake entrainment of group-2 bubbles is expected to be a major coalescence mechanism in the Fu-Ishii model [22]. It is mechanistically modelled by simplifying the interaction to be one-dimensional (in the axial direction), which is a valid assumption for small diameter pipes. Experimentally, a trailing bubble is observed to accelerate when it enters the wake formation of a leading bubble. Empirical correlations for the acceleration velocity of a Taylor bubble [52] are used to estimate the average entrainment collision frequency. The total entrainment rate between group-2 bubbles, S_{WE}^2 is proportional to the number density distribution, f_2 , of group-2 bubbles. The number density distribution is estimated as a flat distribution, which is proportional to α_2 , therefore $S_{WE}^2 \propto \alpha_2$. This relation is realized in the results; with decreasing j_f , the void fraction of group-2 increases, accompanied by an increase in the sink term due to wake entrainment, ϕ_{WE}^2 . Since the implementation of the IATE model (see Section 3.2.3) utilizes experimental data for void fraction, the impact of wake entrainment (or any other mechanisms) has no effect on void fraction propagation. Due to the decoupling of a_i and α_g , a strong insertion of wake entrainment sink for group-2 is still noted after group-2 a_i nullifies.

Analyzing the results obtained for a fixed liquid superficial velocity and different gas superficial velocities, it is evident that problems arising from wake entrainment of group-2 are not isolated to a single region in the j_g-j_f space. In Fig. 3.12, results are shown for a series of tests characterized by constant $j_f = 1.0$ m/s and increasing j_g .

The prediction of a_i is good both qualitatively and quantitatively for $j_g \leq 0.14$ m/s. Similar to the discussion above, at high superficial gas to liquid velocity ratios ($j_g \geq 0.34$ m/s) there is poor prediction of group-2 a_i caused by an over-prediction of the sink term ϕ_{WE}^2 . Furthermore, a similar transitional region is noted for $j_g = 0.22$ m/s, where an expansion dominating sink/source is inaccurate in quantitatively predicting a_i propagation.

The prediction of group-1 interfacial area concentration is overall in good agreement

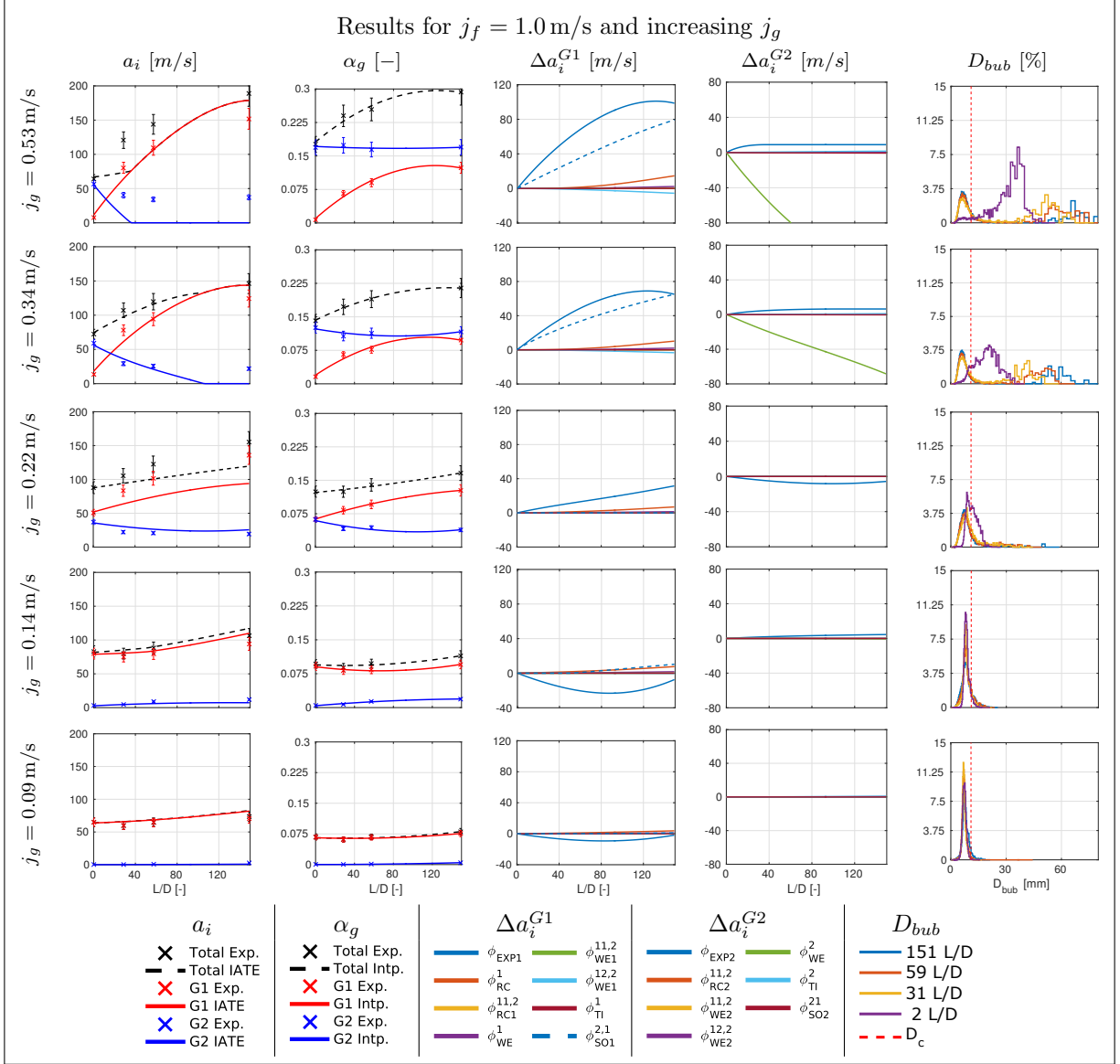


Figure 3.12: Results for Tests 96, 107, 118, 129, and 140 using the 2G IATE model.

with the experimental data, both quantitatively and qualitatively. Aside from the bubble expansion source/sink, the dominating group-1 interaction mechanism (for both Figs. 3.11 and 3.12) is the shearing-off mechanism. This mechanism is expected to be a major a_i source for group-1 bubbles, if there exists large group-2 bubbles in the flow. Therefore the term $\phi_{SO1}^{2,1}$ is proportional to the group-2 void fraction, α_g^{G2} . The usage of experimental void fraction values allows access to accurate group-2 void fraction values and therefore the magnitude of shearing-off. Two empirically determined coefficients γ_{SO} and β_{SO} (Table 3.4) control the average size of group-1 bubbles that are generated through this mechanism. Under the assumption that the magnitude of other minor group-1 interaction mechanisms are predicted

well, the mechanistic and empirical modelling of shearing-off is successful.

A brief discussion of total a_i prediction is also warranted. As noted in Fig. 3.8, the total a_i performance is a blend of group-wise a_i performance. Through observations of tests in Figs. 3.11 and 3.12 this occurs due to two reasons. In tests where group-1 a_i is dominating the total a_i , there tend to be few active interaction mechanisms and the propagation of a_i is expansion driven. In tests where there is a high initial group-2 a_i , the group-2 contribution tends to decrease and reach an equilibrium fast, where as the group 1 a_i sees an exponential increase. As discussed previously, since there is a good prediction of group-1 a_i , this leads to a relatively good prediction of total a_i . This distinction in group-wise and total performance is important as typical best-estimate thermal-hydraulic system codes only require total a_i , while newly proposed formulations of the two-fluid models [76] require group-wise a_i values.

3.3.2.3 Standalone vs. Two-fluid

The results presented previously are from a ‘standalone’ implementation of the IATE model. Standalone refers to the fact that all independent field values for the IATE model are closed using interpolated experimental data (i.e. void fraction and gas velocities). In this section, the beta implementation (TRACE-T [6]) of the Fu-Ishii model in the state-of-the-art thermal-hydraulic system-code, TRACE, is discussed. In TRACE-T, only the experimental values are only used to define the boundary conditions. TRACE-T transports field values through the coupled two-fluid and IATE model. This means that TRACE-T results do not provide an isolated evaluation of IATEA, since errors in prediction of void fraction and gas-velocity will impact results of the implemented IATE model.

The error in predicting total a_i for both standalone and two-fluid models is presented in Fig. 3.13. As expected, the TRACE-T results show higher errors in the high void fraction regions. However, the magnitude of the error in the TRACE-T results is significantly higher than what was obtained with the standalone IATE analysis. Tabulated values of error are presented in Table 3.7. It is interesting to note that the two-fluid model predictions present a significantly higher error for $j_f \geq 5 \cdot 10^{-1}$ m/s. In the discussions of standalone IATE, it was noted that higher superficial gas-to-liquid velocity ratios led to degradation in performance. This discrepancy is due to the two-fluid model having a separate transport equation for α_g . Since the shearing-off mechanism is $\propto \alpha_g^{G2}$, poor prediction of group-2 void fraction will lead to poor prediction of group-1 a_i propagation.

In Fig. 3.13, the experimental void fraction contribution of group-2 bubbles is also presented. Through a visual comparison to the error in prediction of total interfacial area (for both standalone and two-fluid systems), it is apparent that poor performance stems from the prominence of large bubbles. There is an important implication for this strong correlation

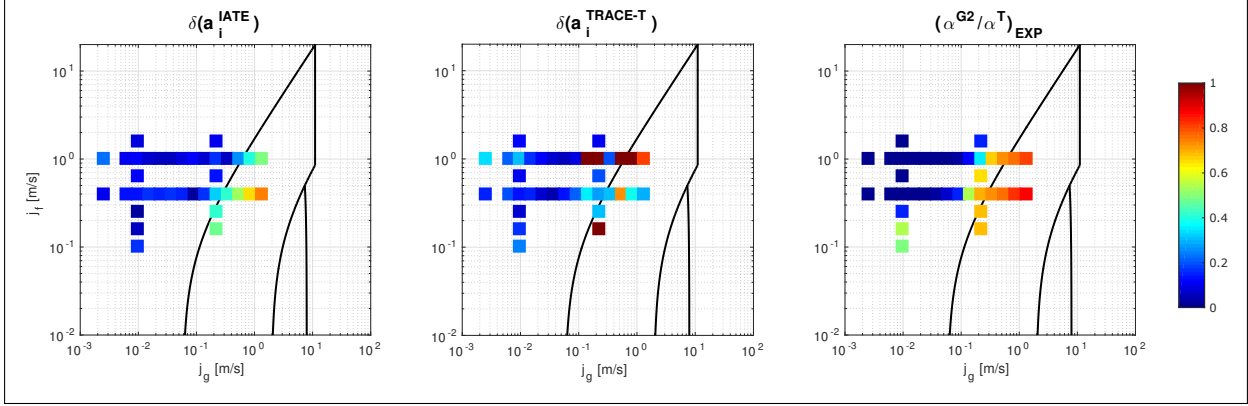


Figure 3.13: A comparison of performance for DN50 TOPFLOW data. Left column indicates error for standalone IATE model, center column indicates error for two-fluid IATE model. The right column presents the experimental void fraction contribution from group 2 bubbles.

– especially in the case of the standalone IATE system. The mechanistic modelling of the Fu-Ishii 2G IATE model [22] has resulted in requirement of several empirically determined coefficients. The experimental data used to evaluate the Fu-Ishii model were measured using conductivity probes [23]. However, in a prior study [48], large discrepancies between conductivity probes and wire-mesh sensors were observed at high void fractions. It is therefore likely that this discrepancy in experimental measurements has led to a correlation between poor IATE performance and high void fraction regimes, when using high resolution wire-mesh sensor data. Therefore, in order to improve IATE performance, it would be essential to reconcile discrepancies between the conductivity probe and wire-mesh sensor experimental methods at high void fraction regimes and determine if any reassessment of the Fu-Ishii coefficients is necessary.

Table 3.5: Average error calculated by Eq. (3.15) for standalone IATE (“ST”) and two-fluid IATE (“TFT”).

ST vs. TFT	$j_g \leq 10^{-2}$ m/s	10^{-2} m/s $< j_g < 2 \cdot 10^{-1}$ m/s	$j_g \geq 2 \cdot 10^{-1}$ m/s
$j_f \geq 5 \cdot 10^{-1}$ m/s	13.2 21.5	7.34 24.9	23.4 61.5
$j_f < 5 \cdot 10^{-1}$ m/s	10.4 15.9	13.4 16.0	50.6 51.5

3.3.3 Remarks

The performance of the two-group Fu-Ishii IATE model has been successful in low void fraction bubbly flows. In such simple flows, the bubble expansion term dominates the propagation of interfacial area. At high superficial velocities, where interaction mechanism

source/sink terms are expected to contribute to interfacial area transport, the IATE performance deteriorates with increasing superficial gas to liquid velocity ratio. The sink for group-2 bubbles is over-predicted by the wake entrainment mechanism, leading to overall poor prediction of the total interfacial area concentration. Group-1 interfacial area is predicted well in almost all tests. The shearing-off mechanism is a major source for group-1 a_i propagation.

In a study by Manera [48], it is noted that while the conductivity probe and wire-mesh sensor measurements are in good agreement for low void fractions, a significant discrepancy exists at high void fractions. The interfacial area concentration measured with conductivity probes is based on the measurement of the surface inclination with respect to the vertical axis. The measurement of such an angle is expected to deteriorate when the interface between phases is mostly parallel to the probes (such as in slug flows). In addition, group-2 measurements might be affected by poor counting statistics. As the IATE model relies on empirically-determined coefficients to close interaction mechanisms, the values require reassessment. The wire mesh sensor has been benchmarked over a wide range of void fractions and is expected to retain accuracy in high void fraction flows. Therefore, the TOPFLOW data provides an avenue for addressing the shortcomings of the 2G IATE model.

A performance comparison of the standalone IATE model (using interpolated experimental field values for closure) to the two-fluid IATE model (using state-of-the-art system code TRACE) was presented. The comparison indicated similar performance in the bubbly flow regime. The two-fluid model performed poorly at lower slip ratios (in contrast to poor performance of standalone IATE at higher slip ratios). This discrepancy manifests as the two-fluid model does not accurately predict field values for group-2 void fraction. This results in a poor prediction of the shearing-off mechanism, and therefore the group-1 interfacial area. This study indicates that future efforts should focus on the improvement in group-2 interfacial area transport, particularly on reassessment of the wake entrainment mechanism.

3.4 Smith-Schlegel Model

Since the Fu-Ishii model is limited to pipe diameters below the stable cap bubble size, Eq. (3.32), a model is required to assess interfacial transport in large-diameter pipes. To be able to understand the requirements for a large-diameter pipe IATE model, it is important to briefly discuss the differences between large and small-diameter pipes with respect to two-phase flow dynamics.

3.4.1 Scaling Effects in Larger Diameters

Four basic flow regimes were identified by Hewitt and Hall-Taylor [25] for upward two-phase flow in vertical small-diameter pipes, namely bubbly flow, slug flow, churn-turbulent flow and annular flow. Flow regime transition criteria were identified by Mishima and Ishii [51]. In small-diameter pipes, as the superficial gas velocity increases, disperse bubbles coalesce to form slugs. These slugs occupy the entirety of the pipe cross-section and are able to sustain their shape, as they are advected, due to the confinement provided by the pipe walls. A visualization of the flow regime development as superficial gas velocity is increased is presented on the left side of Fig. 3.14 for small-diameter pipes.

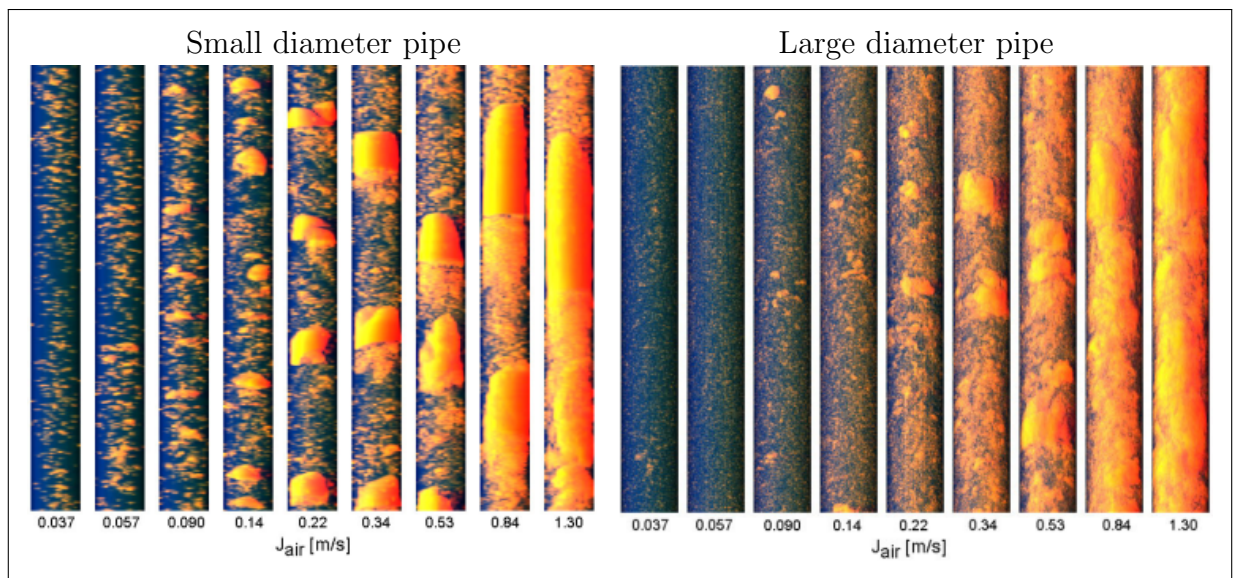


Figure 3.14: Virtual side projections of void distributions from wire mesh sensor measurements in DN50 test section (left) and DN200 test section (right) for $j_f = 1$ m/s [58].

For large-diameter pipes, there are scaling effects at equivalent superficial velocities. Such effects were noted in experimental studies by Ohnuki and Akimoto [55]. Further experiments using wire-mesh sensors by Prasser [58] provided a large database of high resolution (in space and time) experimental data to explore the scaling effects. The right side of Fig. 3.14 displays flow development in a large-diameter pipe as superficial gas velocity is increased. In contrast to the well-defined slug bubble structures noted in smaller diameter pipes, large erratically shaped structures are formed in large-diameter pipes. Slug bubbles are not stable in large-diameter pipes, therefore, with increasing gas superficial velocity, the bubbly flow regime will transit directly to the churn turbulent flow regime. The lack of wall confinement allows bubbles more degrees of freedom in large-diameter pipes, leading to differences in the incidence of interaction mechanisms (i.e. impacts ϕ_j in IATE) on larger bubbles, when

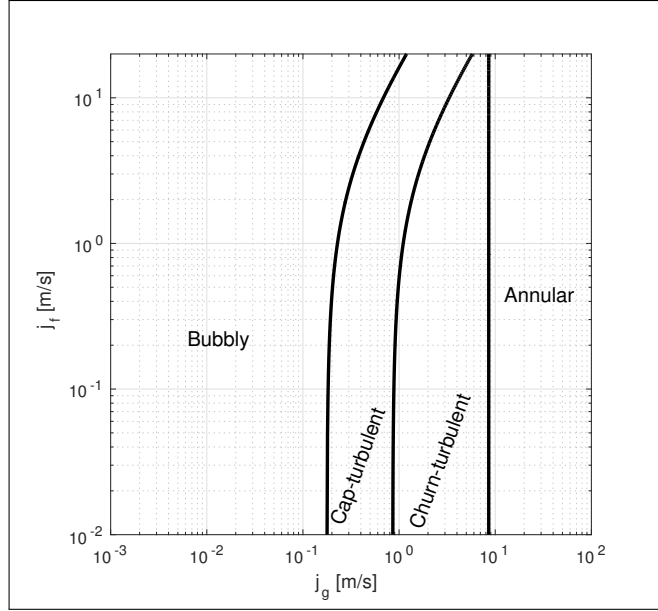


Figure 3.15: Flow regime map for DN200 experimental conditions using criteria proposed by Schlegel [67]. In comparison to Fig. 3.7, no stable slug flow regime exists.

compared to flow in small-diameter pipes. In lieu of scaling effects noted in larger-diameter pipes, corresponding efforts have focused on development of an applicable IATE model.

The performance of the 1G IATE model was evaluated by Sun [78] against air-water flow data recorded for a larger 101.6 mm diameter pipe. Sun concluded that a two-group approach was essential to adequately account for bubble interactions in larger-diameter pipes. Schlegel [67] proposed transition criteria for large-diameter pipes, based on Ohnuki and Akimoto’s studies. In order to develop a mechanistic IATE model for large-diameter pipes, a larger experimental database was required. Experimental studies by Schlegel [66] in 152 mm and 203 mm diameter pipes using conductivity probes provided a basis for the Smith-Schlegel large-diameter IATE model [74].

3.4.2 Interaction Mechanisms

The Smith-Schlegel mechanistic model was evaluated against 102 mm and 152 mm diameter pipes with average interfacial area concentration error of 10.2% and 6.5%, respectively. Smith concluded that further work was necessary to model bubble-induced two-phase turbulence in larger-diameter pipes and that additional data in pipes larger than 152 mm should be evaluated. A list of interaction mechanisms that are accounted for in the Smith-Schlegel 2G IATE model is presented in Table 3.6. There are several differences compared to the Fu-Ishii 2G IATE model (Table 3.4). Surface instability is considered as an independent mechanism

and both random collision and turbulent impact mechanisms have two extra interactions each. Thus the Smith-Schlegel model has five more interaction mechanisms than the Fu-Ishii model. Improvements to the Smith-Schlegel model were suggested by Schlegel [65]; in particular, the prediction of bubble-induced turbulence and relative velocities of bubbles were improved. While source terms in the Smith model are different than the Fu-Ishii model, the interfacial area transport equations remain the same (i.e. Eqs. (3.11) and (3.12)).

Table 3.6: List of various interaction mechanisms accounted for in the Smith-Schlegel model. All parameters used by the model are listed in the last column [74].

Symbols	Mechanisms	Interaction	Parameters
$\phi_{RC}^{(1)}$	Random collision	(1)+(1)→(1)	$C_{RC}^{(1)} = 0.01, C_{RC}^{(12,2)} = 0.01$
$\phi_{RC}^{(11,2)}$	Random collision	(1)+(1)→(2)	$C_{RC}^{(2)} = 0.01$
$\phi_{RC}^{(12,2)}$	Random collision	(1)+(2)→(2)	$C_{WE}^{(1)} = 0.002, C_{WE}^{(12,2)} = 0.01$
$\phi_{RC}^{(2)}$	Random collision	(2)+(2)→(2)	$C_{WE}^{(2)} = 0.06$
$\phi_{WE}^{(1)}$	Wake Entrainment	(1)+(1)→(1)	$C_{TI}^{(1)} = 0.05, C_{TI}^{(2,1)} = 0.04$
$\phi_{WE}^{(11,2)}$	Wake Entrainment	(1)+(1)→(2)	$C_{TI}^{(2)} = 0.01$
$\phi_{WE}^{(12,2)}$	Wake Entrainment	(1)+(2)→(2)	$We_{cr1} = 1.2, We_{cr2} = 1.2$
$\phi_{WE}^{(2)}$	Wake Entrainment	(2)+(2)→(2)	$C_{SO} = 2.5 \times 10^{-6}$
$\phi_{TI}^{(1)}$	Turbulent Impact	(1)→(1)+(1)	$We_{crSO} = 4000$
$\phi_{TI}^{(2,11)}$	Turbulent Impact	(2)→(1)+(1)	$\alpha_{1,max} = 0.62$
$\phi_{TI}^{(2,12)}$	Turbulent Impact	(2)→(1)+(2)	$C_{RC0} = 3.0, C_{RC1} = 3.0$
$\phi_{TI}^{(2)}$	Turbulent Impact	(2)→(2)+(2)	$C_{RC2} = 3.0$
$\phi_{SO}^{(2,12)}$	Shearing-off	(2)→(2)+(1)	
$\phi_{SI}^{(2)}$	Surface Instability	(2)→(2)+(2)	

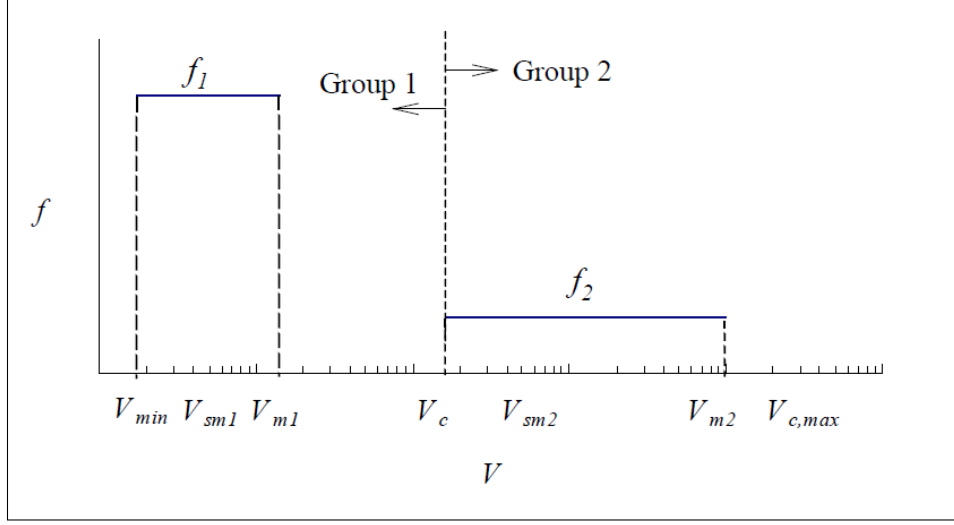


Figure 3.16: Assumption of bubble population distributions in Smith-Schlegel model [73].

3.4.2.1 Random Collision

The random collision involving only group-1 bubbles follows the Wu [82] formulation, Eq. (3.16), using isotropic turbulence to estimate coalescence frequency. However, the remaining two interactions (both involving a group-2 bubble), are reconsidered for larger pipes. In order to model the new interactions, the terms in Eq. (3.13) are evaluated.

Group 1 and 2 random collision

The coalescence efficiency [13] of group-2 bubbles is given by

$$\lambda_{RC}^{(2)} = \exp\left(-C_{RC0} \frac{D_{sm2}^{5/6} \rho_f^{1/2} \varepsilon^{1/3}}{\sigma^{1/2}}\right), \quad (3.40)$$

where C_{RC0} is an empirically determined coefficient. Also,

$$\phi_{RC,1}^{(12,2)} = -1.14 C_{RC}^{(12,2)} \lambda_{RC}^{(2)} (\varepsilon \alpha_1^2 \alpha_2^4 a_{i1}^3 a_{i2}^2)^{1/3} \left[1 - \exp\left(-C_{RC1} \frac{(\alpha_{1m} \alpha_1)^{1/3}}{\alpha_{1m}^{1/3} - \alpha_1^{1/3}}\right)\right], \quad (3.41)$$

$$\phi_{RC,2}^{(12,2)} = 1.80 C_{RC}^{(12,2)} \lambda_{RC}^{(2)} (\varepsilon \alpha_1^5 \alpha_2 a_{i2}^5)^{1/3} \left[1 - \exp\left(-C_{RC1} \frac{(\alpha_{1m} \alpha_1)^{1/3}}{\alpha_{1m}^{1/3} - \alpha_1^{1/3}}\right)\right], \quad (3.42)$$

where $C_{RC}^{(12,2)}$ is an empirically determined coefficient.

Group 2 random collision

The cross-sectional area of larger group-2 bubbles and fluctuating turbulent velocity is considered. The upper limit of integration is the maximum stable group-2 bubble size (Eq. (3.32)). The interfacial area sink rate due to random collision of group-2 bubbles is

$$\phi_{RC}^{(2)} = -95.7 C_{RC}^{(2)} \lambda_{RC}^{(2)} (\varepsilon \alpha_2^7 a_{i2}^{-1})^{1/3} \frac{1}{D^2} \left[1 - \exp \left(-C_{RC2} \alpha_2^{1/2} \right) \right] (1 - 0.37 D_{c2}^*{}^3) , \quad (3.43)$$

where $D_{cj}^* \equiv D_c / D_{smj}$.

3.4.2.2 Wake Entrainment

Group 1 wake entrainment

The wake entrainment mechanism for group-1 bubbles is considered similar to the Fu-Ishii formulation. The cylindrical wake region behind the bubble is considered and using the average rise velocity, the coalescence rate is determined to be Eq. (3.44). The same approach (with corrected integral limits) is used to determine the source for group-2, Eq. (3.45):

$$\phi_{WE}^{(1)} = -0.17 C_{WE}^{(1)} C_{D1}^{1/3} u_{r1} a_{i1}^2 , \quad (3.44)$$

$$\phi_{WE}^{(11,2)} = 2.57 C_{WE}^{(11,2)} C_{D1}^{1/3} u_{r1} a_{i1}^2 \left(1 - \frac{2}{3} D_{c1}^* \right) , \quad (3.45)$$

where both $C_{WE}^{(1)}$ and $C_{WE}^{(11,2)}$ are empirically determined coefficients.

Group 1 into 2 wake entrainment

The entrainment of group-1 bubbles into leading large group-2 bubbles is also considered. In this case, the cross-sectional area, local wake velocity, u_{w2} , and cap bubble relative velocity, u_{r2} , is considered. The average rise velocity of the bubbles, \bar{u}_{rw2} can be calculated from u_{w2} through an axial average over the wake length. As a first order approximation, the dependence of the group-2 drag coefficient on volume is ignored. The resulting loss for group-1 and gain for group-2 are

$$\phi_{WE,1}^{(12,1)} = -0.33 C_{WE}^{(12,2)} \bar{u}_{w12} a_{i1} a_{i2} , \quad (3.46)$$

$$\phi_{WE,2}^{(12,2)} = 0.922 C_{WE}^{(12,2)} \bar{u}_{w12} a_{i2}^2 \frac{\alpha_1}{\alpha_2} , \quad (3.47)$$

where $\bar{u}_{w12} = \bar{u}_{rw2} + u_{r1} - u_{r2}$ is the local wake velocity of the bubble. Again, another empirically determined coefficient $C_{WE}^{(12,2)}$ is introduced.

Group 2 wake entrainment

The approach to modelling the entrainment between two group-2 bubbles is similar to the “group-1 into group-2” wake entrainment model, except the number density of the trailing bubble now corresponds to group-2. Smith [74] reiterates that while wake entrainment of group-2 bubbles eventually leads to ‘stable’ slug bubbles in smaller diameters, a similar entrainment process may continue indefinitely in larger-diameter pipes. The resulting loss in group-2 interfacial area is

$$\phi_{WE}^{(2)} = -1.02C_{WE}^{(2)} [1 - \exp(-0.7\alpha_2)] \bar{u}_{rw2} \frac{a_{i2}^2}{\alpha_2} (1 - 0.10D_{c2}^{*2}) . \quad (3.48)$$

3.4.2.3 Turbulent Impact

The turbulent impact mechanism again considers the balance of cohesive and disruptive forces, assessed by the Weber number Eq. (3.31). When a critical value (We_{cr}) is exceeded, a disintegration of a bubble occurs. Four cases are mechanistically modelled.

Group 1 turbulent impact

The breakup of group-1 bubbles lead to a net gain for group-1 a_i of

$$\phi_{TI}^{(1)} = 0.12C_{TI}^{(1)} (\varepsilon a_{i1}^5 \alpha_1^{-2})^{1/3} (1 - \alpha_g) \exp\left(-\frac{We_{cr1}}{We_1}\right) \left(1 - \frac{We_{cr1}}{We_1}\right)^{1/2} , \quad (3.49)$$

where $C_{TI}^{(1)}$ is an empirically determined coefficient.

Group 2 turbulent impact

While the break of group-2 bubbles may result in more than two daughter bubbles, it is assumed that only binary breakup can occur. The resulting gain for group-1 a_i , if daughters are both group-1 bubbles, is given by

$$\begin{aligned} \phi_{TI,1}^{(2,1)} &= 6.165C_{TI}^{(2,1)} (\varepsilon a_{i2}^5 \alpha_2^{-2})^{1/3} (1 - \alpha_g) \exp\left(-\frac{We_{cr2}}{We_2}\right) \left(1 - \frac{We_{cr2}}{We_2}\right)^{1/2} \times \\ &\times \left(0.212D_{c2}^{*13/3} - 0.167D_{c2}^{*5}\right) , \end{aligned} \quad (3.50)$$

where $C_{TI}^{(2,1)}$ is an empirically determined coefficient. The remaining cases occur when a group-2 bubble break-up results in daughters that are either a group-1 and group-2 ((2) → (1) + (2)) or both are group-2 bubbles ((2) → (2) + (2)). The net gain of both interactions

for group-2 a_i are considered and represented by

$$\begin{aligned} \phi_{TI,2}^{(2)} &= 0.378C_{TI}^{(2)} (\varepsilon a_{i2}^5 \alpha_2^{-2})^{1/3} (1 - \alpha_g) \exp\left(-\frac{We_{cr2}}{We_2}\right) \left(1 - \frac{We_{cr2}}{We_2}\right)^{1/2} \times \\ &\times \left(1 - 0.212D_{c2}^*{}^{13/3}\right), \end{aligned} \quad (3.51)$$

where $C_{TI}^{(2)}$ is an empirically determined coefficient.

3.4.2.4 Shearing-off

The shearing-off mechanism is expected to be a major source of group-1 interfacial area. Similar to the Fu-Ishii approach, the mechanism is modelled by estimating the size of the sheared-off bubbles [19] and the volume that is sheared-off as the bubble is transported. The resulting interfacial source for group-1 is

$$\phi_{SO,1}^{(2,12)} = 7.17C_{SO} \frac{(\rho_f^3 v_{r1} \sigma^2 D^{-2} We_{c,SO}^{-3})^{1/5} a_{i2}^2}{\rho_g} \left[1 - \left(\frac{We_{c,SO}}{We_{m2}}\right)^4\right], \quad (3.52)$$

and the corresponding sink for group-2 is,

$$\phi_{SO,2}^{(2,12)} = -0.36C_{SO} \frac{\sigma}{\rho_g v_{g2}} \frac{a_{i2}^3}{\alpha_2^2} \left[1 - \left(\frac{We_{c,SO}}{We_{m2}}\right)\right], \quad (3.53)$$

where C_{SO} is an empirically determined constant.

3.4.2.5 Surface Instability

The surface instability mechanism was not explicitly modelled in the Fu-Ishii model. However this phenomenon requires separate consideration for larger-diameter pipes. Due to the increased bubbles mobility as a consequence of the limited confinement effects from the pipe walls, it is expected that coalescence of group-2 bubbles can lead to the temporary formation of a bubble that is larger than the stable limit (Eq. (3.32)). Both random collision and wake entrainment can form such large bubbles. Therefore, the surface instability considers contributions from both mechanisms, and no new coefficients are introduced:

$$\begin{aligned} \phi_{SI}^{(2)} &= 2.62 \times 10^{-4} C_{RC}^{(2)} \varepsilon^{1/3} \frac{\alpha_2^2}{D_h^2} \left[1 - \exp\left(-C_{RC2} \alpha_2^{1/2}\right)\right] \left(\frac{\sigma}{g\Delta\rho}\right)^{1/6} + \\ &+ 1.43 \times 10^{-7} C_{WE}^{(2)} \bar{u}_{rw2} \alpha_2^2 \left[1 - \exp(-0.7\alpha_2)\right] \left(\frac{\sigma}{g\Delta\rho}\right)^{-1}. \end{aligned} \quad (3.54)$$

3.4.3 Evaluation

The performance of the Smith-Schlegel large diameter IATE model has been assessed against TOPFLOW DN200 experimental data (discussed in Section 3.2.2). Test flow conditions range from bubbly flow to annular flow regimes, allowing the assessment of IATE model over all flow regimes encountered in large diameter vertical pipes. An overview of the Smith-Schlegel IATE performance is presented in Section 3.4.3.1 to highlight regions of good and poor performance. Individual tests are then discussed in detail in Section 3.4.3.2, where the main mechanisms contributing to interfacial area propagation are investigated. Recommendations on how to improve IATE performance are discussed in Section 3.4.3.3 contains discussion of possible paths towards improving IATE performance. The error estimator used in the following sections is determined by Eq. (3.15).

3.4.3.1 Overview of Performance

Evaluations of all DN200 test conditions are presented in Fig. 3.17, where the error in predicting group-wise and total a_i is reported. The large-diameter vertical pipe flow regime map proposed by Schlegel [67] (Fig. 3.15) has been included in the background. Several tests correspond to the cap-turbulent and churn-turbulent regimes. We note that the transition to annular flow regime, indicated in Table 3.3 is slightly different than the transition predicted by Schlegel's criterion [67].

For group-1 (small bubbles), the IATE model performs very well at superficial gas velocities < 3 cm/s, with average error mostly below $\pm 10\%$. As the superficial gas velocity increases, group-1 a_i is incorrectly predicted. The prediction of group 1 a_i deteriorates significantly with the appearance of group-2 bubbles at higher superficial gas velocities. The Smith-Schlegel model exhibits poor performance for the group-2 a_i over the entire range of flow conditions analyzed with the exception of two tests at high superficial liquid velocity and low superficial gas velocity. The prediction of a_i deteriorates for both groups as the ratio of superficial gas to superficial liquid velocity increases.

Although group-wise prediction of interfacial area is poor, the total a_i is predicted reasonably well for most of the tests analyzed. At $j_g < 3$ cm/s the estimated total a_i depends solely on group-1 performance and therefore good prediction is expected. It is noteworthy that for $j_g > 3$ cm/s the prediction of total a_i is good despite large errors in the prediction of group-1 and group-2 a_i . Surprisingly, even in high void fraction flow regimes, the error in predicting total interfacial area remains fairly low for most tests (within $\pm 20\%$). Clearly, the good predictions of total a_i are the result of compensation of errors in the estimation of group-1 and group-2 interaction mechanisms.

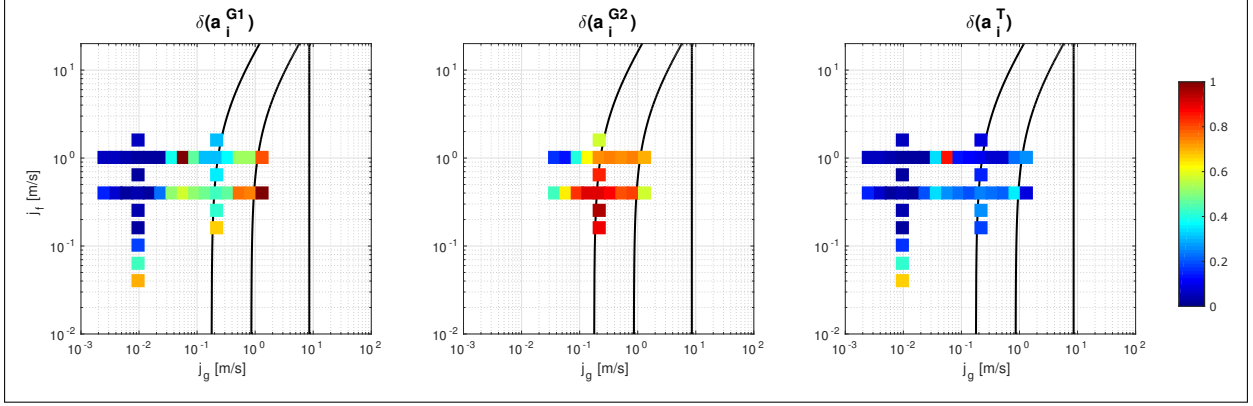


Figure 3.17: A comparison of performance for DN200 TOPFLOW data. Left column indicates error for group 1 interfacial area concentration and right column indicates error for group 2 interfacial area concentration. The third column indicates error for prediction of total interfacial area.

3.4.3.2 Discussion

In the following figures, the comparison of experimental and calculated values for the interfacial area is presented in detail. Experimental data are presented as discrete data (with uncertainty bars of $\pm 10\%$ [15]). The predicted a_i is presented as continuous data. Group-1 results are shown in red color, while Group-2 results are shown in blue. The contributions of separate source terms (ϕ_{j1} and ϕ_{j2}) are also reported in order to understand the contribution of underlying mechanisms to the a_i propagation. The experimental and interpolated values of the void fraction (α_g) evolution along the pipe axis are also presented.

The results for Test 19 and 42, both corresponding to the bubbly flow regime, are presented in Fig. 3.18. In these tests, large bubbles are absent, therefore the group-2 a_i is null and the total a_i corresponds to the group-1 a_i . The values for interfacial area are predicted well by the IATE model. Upon inspecting values for group-1 a_i contribution (Δa_i^{G1}), it is noted that the bubble expansion term (ϕ_{EXP1}) is the dominating mechanism for both tests (the group 1 expansion is the first term on the right hand side of Eq. (3.11); a similar term for group 2 expansion exists in Eq. (3.12)). In steady-state, adiabatic, air-water flows the bubble expansion term simplifies to Eq. (3.39).

The bubble expansion term is a function of void fraction values and gas phase velocity. Since both these quantities are taken from interpolated experimental data, it is expected that Eq. (3.39) accurately computed (in the limit of the measurement accuracy for void fraction and gas velocity). This is reflected by the good a_i prediction. Hence the IATE model is found to be successful at low superficial gas and liquid velocities within the bubbly flow regime, where the bubble expansion term is dominating.

In Fig. 3.19 results for four tests are presented, corresponding to a superficial liquid

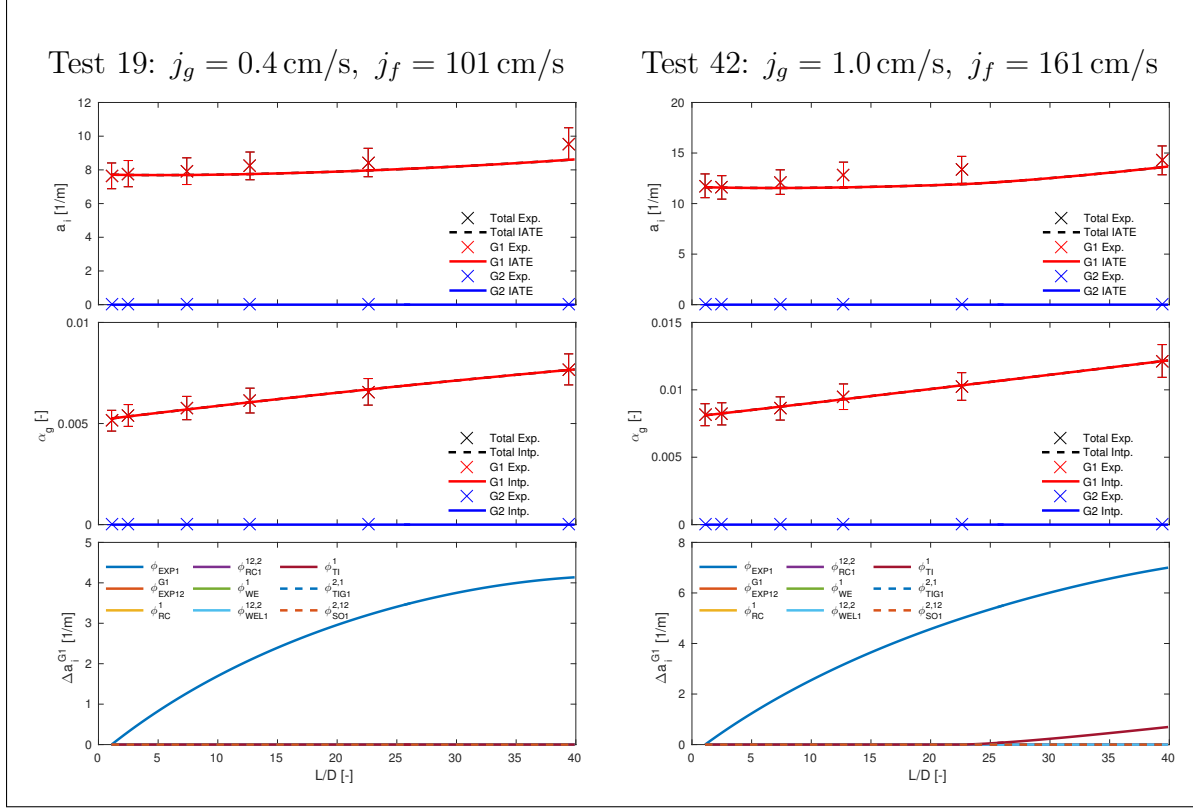


Figure 3.18: IATE results for Test 17 and 42.

velocity of 1.02 m/s, and increasing values of superficial gas velocity. In the figure, group-wise and total a_i and void fraction evolution are reported together with the group-wise cumulative source term contributions and the axial development of bubble size (D_{bub}) distributions as measured by WMS. The value of D_c , the critical bubble diameter, is indicated in the bubble size distributions to separate populations of group-1 and group-2 bubbles.

In the first two tests, at $j_g = 1.5$ cm/s and $j_g = 2.4$ cm/s, only small group-1 bubbles are present (the entire bubble size spectrum being below D_c). The a_i is predicted correctly by the IATE model. The dominating source term is once again the bubble expansion term. However, as the superficial gas velocity increases further to 3.7 cm/s, other interaction mechanisms start playing a role. For group-1, the shearing-off from large group-2 bubbles has a larger impact than the expansion term ϕ_{EXP1} and leads to an over-prediction of group-1 a_i . The over-prediction is more severe when the superficial gas velocity is increased further to 5.7 cm/s. Group 2 a_i predicted well in Fig. 3.19. Group 2 bubbles only appear for $j_g \geq 3.7$ cm/s and the dominating mechanisms are bubble expansion and shearing-off.

It is important to note that while the shearing-off mechanism in group-1 causes an over-prediction of break-up, a corresponding over-prediction of sink is not noted for group-2. When the shearing-off mechanism plays a role, the volume is conserved, yet the interfacial

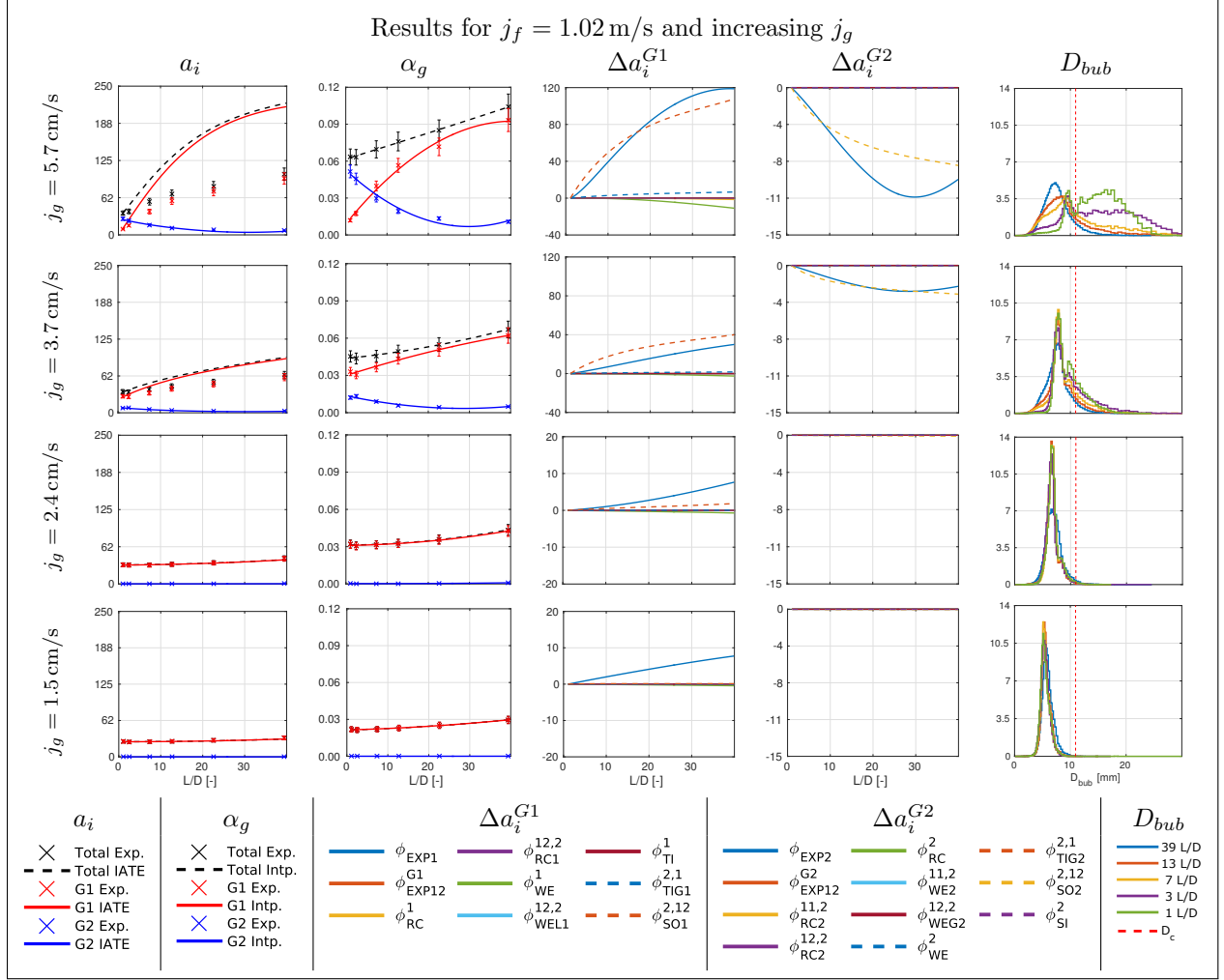


Figure 3.19: IATE results for tests 52, 63, 74, and 85.

area concentration is not conserved, and a net gain of total a_i is expected [74]. This is due to the high interfacial area concentration of small sheared-off bubbles (which belong to group-1).

The shearing-off process is mechanistically modelled through several assumptions. All group-1 bubbles that are sheared-off are assumed to have a spherical shape and a singular size, d_s . The parent group-2 bubble is modelled as a large cap bubble. The magnitude of daughter particle diameter, d_s , is assumed to be equivalent to the skirt thickness of the parent. Both $\phi_{SO1}^{2,12}$ and $\phi_{SO2}^{2,12}$ are formulated with these assumptions and are proportional to an empirically determined constant, $C_{SO} = 5 \times 10^{-5}$. Thus, high j_g tests in Fig. 3.19 indicate that either the diameter of daughter group-1 bubbles from shearing-off is underestimated (i.e. higher a_i source), or there is an underestimation of group-1 coalescence (i.e. an underestimation of the group-1 a_i sink). It is also noteworthy that the bubble size distributions for $j_g = 5.7$ cm/s

indicate rapid break-up of large bubbles ($1 L/D$ to $7 L/D$) downstream of the gas injection, which is not successfully captured by the Smith-Schlegel model.

At higher superficial gas, in the churn-turbulent flow regime, more complex bubble structures appear in the flow. Tests 116, 117, 118 and 119 are representative of churn-turbulent flow and their results are presented in Fig. 3.20. At the highest superficial liquid velocity, 1.61 m/s, the interfacial area for both group-1 and group-2 is captured qualitatively – however, large quantitative discrepancies between predicted and experimental values are observed for $> 10 L/D$. In addition to the shearing-off and bubble expansion terms, the turbulent impact source term, ϕ_{TI}^1 , also contributes to the group-1 a_i propagation. For group-2, the wake entrainment mechanism (ϕ_{WE}^2) becomes the sole driver of a_i . However, this mechanism is over-predicted, leading to an underestimation of group-2 a_i . Therefore, the mechanism ϕ_{WE}^2 requires re-evaluation.

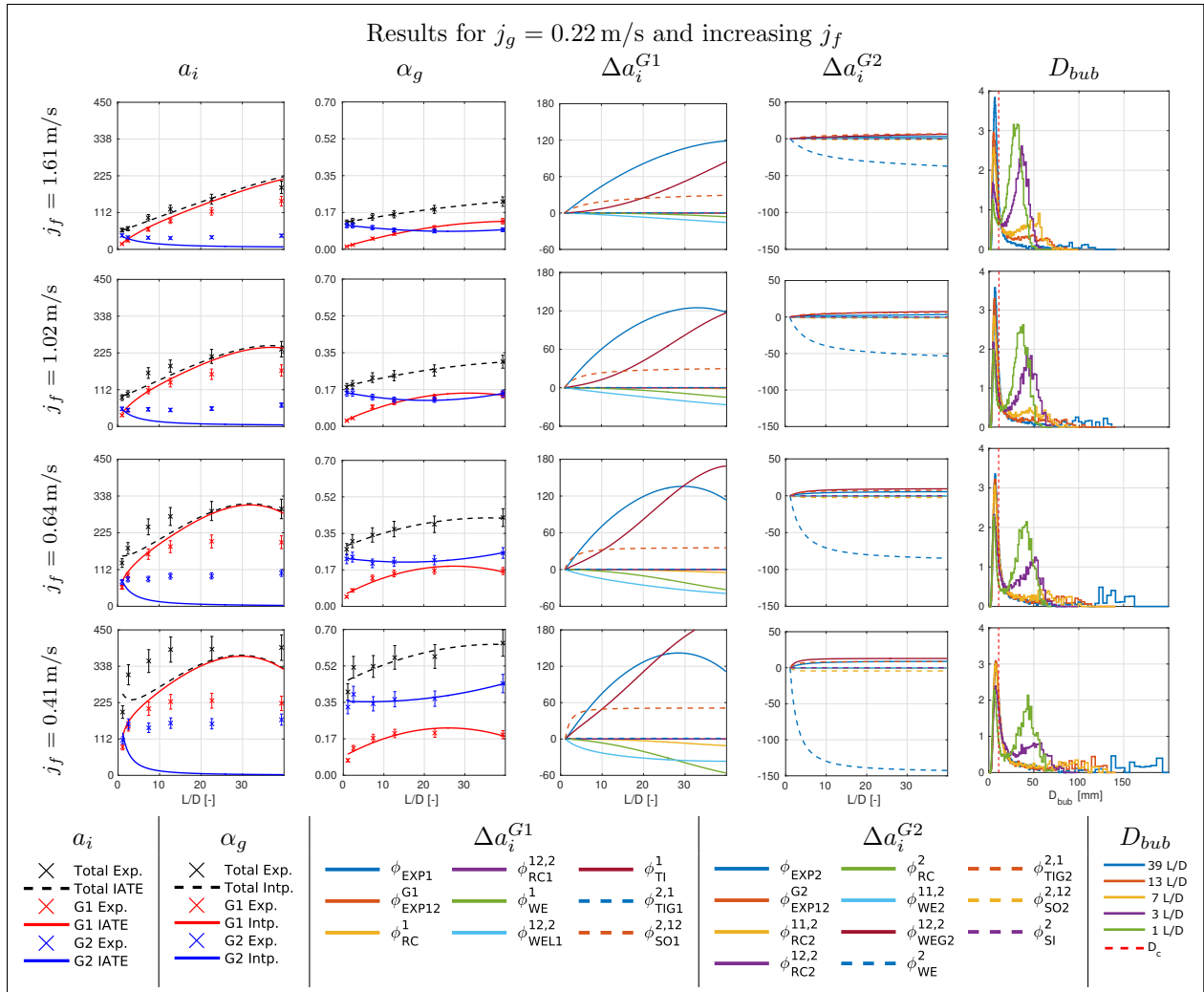


Figure 3.20: IATE results for tests 116, 117, 118, and 119.

As the superficial liquid velocity is decreased, the prediction of group-wise a_i degrades monotonically. For all tests, both wake entrainment mechanisms (ϕ_{WE}^1 and $\phi_{WEL1}^{12,2}$) are contributing to Δa_i^{G1} . Both terms of the wake entrainment represent a sink for group-1 a_i , but, the (negative) contribution of the wake entrainment to group-1 a_i is smaller than the (positive) contribution of bubble expansion, shearing-off and turbulent impact sources (ϕ_{EXP1} , $\phi_{SO1}^{2,12}$, and ϕ_{TI}^1). The turbulent impact mechanism for group-1 bubbles (ϕ_{TI}^1) becomes a dominating source causing over-prediction of group-1 a_i . The mechanism considers eddies that are approximately the same size as the group-1 bubble. Essential to the prediction of the collision frequency between an eddy and a bubble is the turbulent dissipation rate [74]. Schlegel suggested improvements in calculating the dissipation rate [65] by considering velocity differences between the disperse and liquid phase. However, even with Schlegel's improvements, ϕ_{TI}^1 is driving an incorrectly large source insertion.

Additional insight can be gained by analyzing the measured evolution of the bubble size distribution along the pipe axis. While there is an increase in the group-1 size distribution from 1 L/D to 7 L/D , the distribution remains constant thereafter. This indicates that a short development length is required for the source and sink mechanisms of group-1 to stabilize. This is not replicated in the IATE model predictions. For group-2, the shearing-off mechanism dominates all other mechanisms. Unfortunately, this leads to a significant over-prediction of a_i^{G2} sink. The experimental bubble size distributions indicate that larger and larger bubbles appear in the flow as it develops along the pipe. This is consistent with a decrease of group-2 a_i due to coalescence. Therefore, group-2 sink terms need to be revisited.

The above discussions have focused solely on the accuracy of group-wise performance of IATE. However, when the IATE model is coupled to the conventional two-fluid equations, the *total* a_i (Eq. (1.10)) is required for closure. Thus, evaluating performance of the IATE model with the viewpoint of assessing total a_i performance is also necessary. In low void fraction tests that are dominated by group-1 bubbles (Fig. 3.18 and Fig. 3.19), there is a negligible difference between group-wise and total a_i , and hence no difference between their respective accuracy. However, in high void fraction tests that have a sizable group-2 bubble population, there are significant differences. In Fig. 3.20, at the highest superficial liquid velocity (1.61 m/s), the group-wise values of a_i begin to increasingly deviate from experimental data as the flow develops and are outside the experimental uncertainty error bars at 7 L/D . In contrast, the prediction of total a_i value remains accurate and misses the experimental reading at 39 L/D by a small margin. This is due to the fact that the addition of the over-prediction of group 1 a_i is compensated by the under-prediction of group 2 a_i .

The erroneous yet successful prediction of total a_i is not limited to the tests discussed above. Two further tests, at high void fraction and high superficial gas and liquid velocities

are presented in Fig. 3.21. Test 140 is in the churn-turbulent flow regime, while test 160 is in the annular flow regime. Both tests indicate a similar over-prediction of group-1 a_i and under-prediction of group-2 a_i – resulting in a good prediction of total a_i . These results explain the apparent discrepancy in group-wise and total a_i performance noted in discussions of Fig. 3.17. Although it would be incorrect to discuss the validity of source term contributions, it is prudent to discuss dominating terms. For test 160, there are few dominating terms in both group-1 and group-2. The shearing-off mechanism dominates group-1 a_i propagation in test 160, and plays a lesser role in test 140. Group-2 is heavily impacted by the wake entrainment mechanism for group-2 bubbles in both tests. The wake entrainment mechanism was also criticized previously when group-2 bubbles constitute a significant part of the overall void fraction (Fig. 3.20).

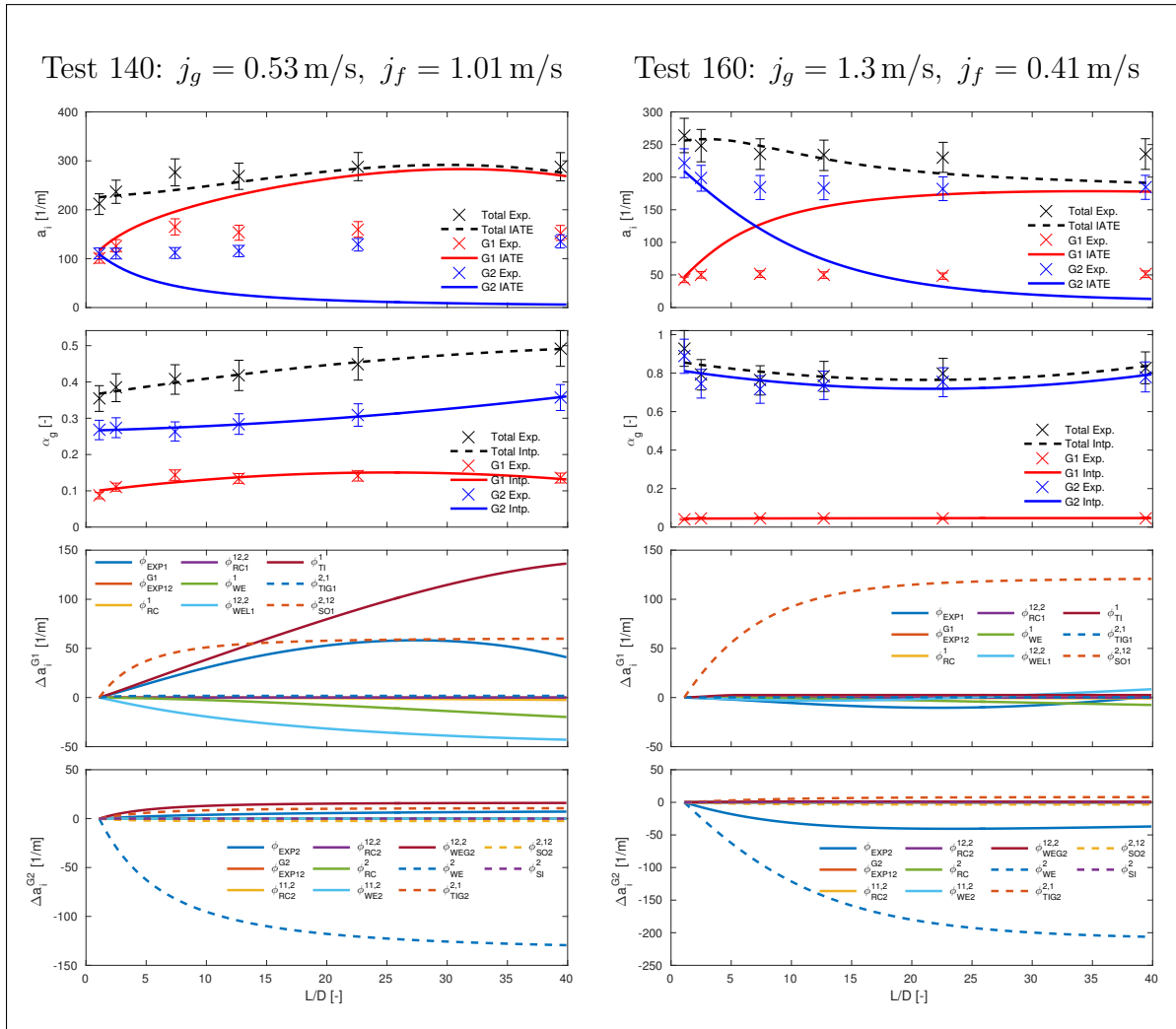


Figure 3.21: IATE results for Test 140 and 160.

3.4.3.3 Path Forward

For group 1, the IATE model performs well at superficial gas velocities < 3 cm/s, with average error mostly below $\pm 10\%$. As the superficial gas velocity increases, group-1 a_i is incorrectly predicted. The deterioration in the prediction of group-1 a_i coincides with the appearance of group-2 bubbles at higher superficial gas velocities. IATE performance for group-2 is in general rather poor, with the exception of flow conditions characterized by high superficial liquid velocity and low superficial gas velocity. The dominating mechanism for group-2 bubbles is the shearing-off mechanism, which also contributes to over-prediction of the source term for group-1 bubbles. The conventional two-fluid model only requires the total a_i and therefore would only be affected by the estimation of total a_i . However, a modified two-fluid model [76] that transports two disperse groups, requires group-wise a_i . Thus, if the modified two-fluid model is coupled to the current IATE model, results at high void fraction may be invalid.

At its current state, the TOPFLOW large diameter pipe data indicates that the Smith-Schlegel IATE model is only valid in the low void fraction bubbly flow regime. A reassessment of the coefficients used for the mechanisms may improve performance of the Smith-Schlegel model. The fact that poor predictions of group-1 and group-2 a_i compensate one another might indicate that the published coefficients [65, 74] have been optimized by minimizing the error on the prediction of the total a_i only, rather than group-wise performance.

We have also shown that the low void fraction bubbly flow tests that are successfully predicted using the current IATE model (Fig. 3.18) correspond to cases in which the bubble expansion term is the dominating mechanism. The bubble expansion term is similar in formulation for both group-1 and group-2 transport, Eq. (3.39). The performance of the transport equations if only bubble expansion is considered (i.e. all interaction mechanisms are ignored, $\phi_j^1 = \phi_j^2 = 0$) is presented in Fig. 3.22. In contrast to Fig. 3.17, there is a significant improvement in group-wise a_i prediction for high void fraction tests. The error in predicting total interfacial area is tabulated in Table 3.7. On average, a significant improvement is noted for $j_f < 5 \cdot 10^{-1}$ m/s, while mostly retaining performance in other regimes. This comparison indicates that at the current state, the modelling of the interaction mechanisms is deteriorating the prediction of group-wise a_i , while contributing to a very slight improvement of the total interfacial area prediction at high j_f . Therefore, the incidences of interaction mechanisms (and therefore their coefficients) need to be reassessed, in particular the shearing-off and group-1 turbulent impact mechanisms.

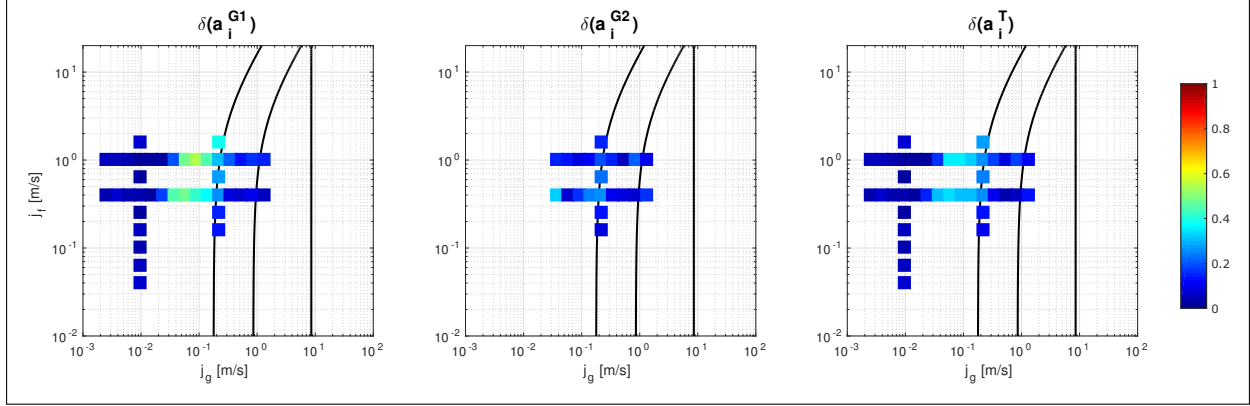


Figure 3.22: Performance for DN200 TOPFLOW data with interaction mechanisms nullified. Left column indicates error for group 1 interfacial area concentration and right column indicates error for group 2 interfacial area concentration. The third column indicates error for prediction of total interfacial area.

Table 3.7: Average error [%] for total interfacial area calculated by Eq. (3.15) for Smith-Schlegel model ('IATE') and IATE equations with only expansion term ('EXP').

IATE vs. EXP	$j_g \leq 10^{-2}$ m/s	10^{-2} m/s $< j_g < 2 \cdot 10^{-1}$ m/s	$j_g \geq 2 \cdot 10^{-1}$ m/s
$j_f \geq 5 \cdot 10^{-1}$ m/s	4.38 4.29	24.3 20.3	13.6 19.0
$j_f < 5 \cdot 10^{-1}$ m/s	17.5 4.68	20.4 23.7	51.3 10.3

3.4.4 Remarks

The Smith-Schlegel model has been found to perform well in the bubbly flow regime, with errors in the prediction of the interfacial area concentration less than $\pm 10\%$. It has been shown that in the bubbly flow regime, the primary source of a_i propagation is the bubble expansion mechanism, which relies on the correct estimation of the axial pressure drop. In the churn-turbulent flow regime, large group-2 bubbles are present in the flow and the wake entrainment mechanism becomes important, together with other mechanisms such as shearing-off. Shearing-off of group-2 bubbles leads to an over-estimation of the group-1 source term, resulting in poor predictions of the group-1 a_i . In the transition from churn-turbulent to annular flow, several interaction mechanisms have been found to contribute to inaccurate a_i prediction for group-1. However, wake entrainment remains the dominating mechanism for group 2. Additionally, the capability of wire mesh sensors to provide bubble size distributions has also indicated that group-wise dominance of coalescence or break-up is often incorrect. Furthermore, in high void fraction regimes, while the prediction of group-wise a_i was incorrect, total a_i was predicted well as a result of compensation of errors.

The Smith-Schlegel IATE model provides a necessary step towards accounting for the difference in flow dynamics from small to large diameter vertical pipes. However, future evaluations of the model should concurrently consider both total and group-wise performance to allow compatibility with conventional and modified two-fluid models. Comparisons to evaluations of the TOPFLOW database that only consider bubble expansion indicate that further re-evaluation of interaction mechanisms are necessary in high void fraction regimes. In particular, focus should be dedicated to the shearing-off mechanism, which was shown to dominate interfacial area propagation for group-2, and to the turbulent impact mechanism, which was shown to dominate group-1.

Chapter 4

Optimization Studies

Before proceeding with the optimization of the two-group IATE models, a brief summary of the performance of the current models is provided. The detailed evaluation of the existing two-group Fu-Ishii IATE model against the TOPFLOW DN50 air-water database is reported in Section 3.3.2. The detailed evaluation of the existing two-group Smith-Schlegel IATE model against the TOPFLOW DN200 air-water database is reported in Section 3.4.3. All proceeding work in this chapter is an original contribution of the dissertation.

State of Fu-Ishii model performance

The summary of the prediction of group-wise and total interfacial area is shown in Fig. 4.1, where the figure of merit expressed by Eq. (3.15), represents the deviation of the IATE model prediction from experimental data. It was found that the IATE model performs well for group-1 bubbles, but that the performance deteriorates as the flow conditions move toward the slug flow regime. The prediction of group-2 a_i is generally poor. The wake entrainment mechanism for group-2 bubbles is the major contributor towards over-prediction of interfacial area sink. Table 4.1 presents quantitative distribution of error. The error generally remains below 20% for $j_g < 2 \cdot 10^{-1}$ m/s; it is substantially higher at high j_g .

The Purdue experiments [34] using conductivity probes are used as an independent database to assess the performance of the Fu-Ishii model after its optimization based on TOPFLOW DN50 data. The performance of the default Fu-Ishii two-group IATE model against a compilation of all available Purdue tests is presented in Fig. 4.2. The Purdue database includes experiments performed for 12.7mm, 48.3mm, 102 mm and 152 mm diameter test sections. As for the TOPFLOW tests, good performance is found for group-1 bubbles. Group-2 interfacial area density propagation is poorly predicted, with error generally above 40%. It is notable that the performance for group-2 bubbles in 48.3 mm diameter

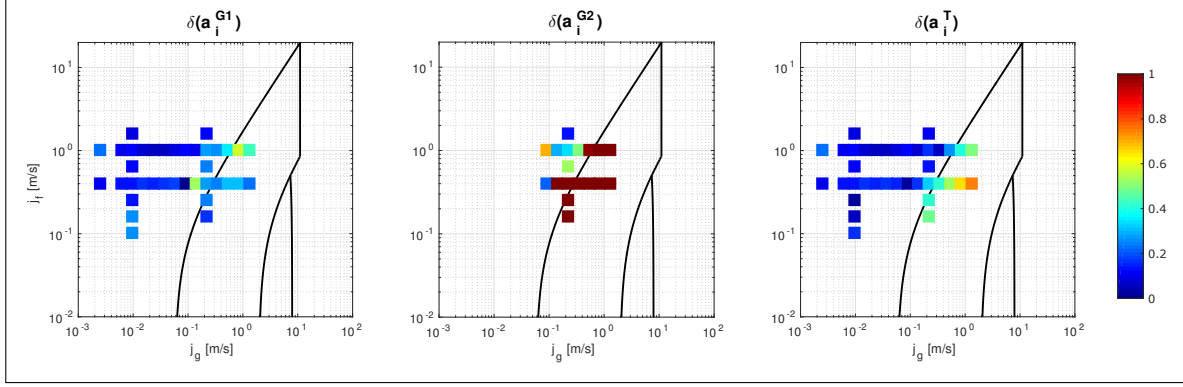


Figure 4.1: A comparison of performance for DN50 TOPFLOW data.

Table 4.1: A comparison of average error calculated by Eq. (3.15) for all TOPFLOW DN50 tests.

		$j_g \leq 10^{-2}$ m/s	10^{-2} m/s $< j_g < 2 \cdot 10^{-1}$ m/s	$j_g \geq 2 \cdot 10^{-1}$ m/s
$j_f \geq 5 \cdot 10^{-1}$ m/s	G1	13.2	7.92	31.8
	G2	0.00	16.6	63.9
	T	13.2	7.34	23.4
$j_f < 5 \cdot 10^{-1}$ m/s	G1	17.1	20.0	25.0
	G2	0.00	20.2	100
	T	10.4	13.4	50.6

pipes is particularly poor, as observed with the TOPFLOW DN50 (52.3 mm) diameter pipe experiments. A quantitatively comparison is shown in Tables 4.1 and 4.2. Hereafter, results from the Purdue tests measured for 12.7, 102, and 152 mm) diameter test sections will be discussed separately. The results for these latter tests are summarized in Table 4.3. While the error for the total interfacial area remains below 20% for all tests, poor predictions for group 2 a_i are still observed.

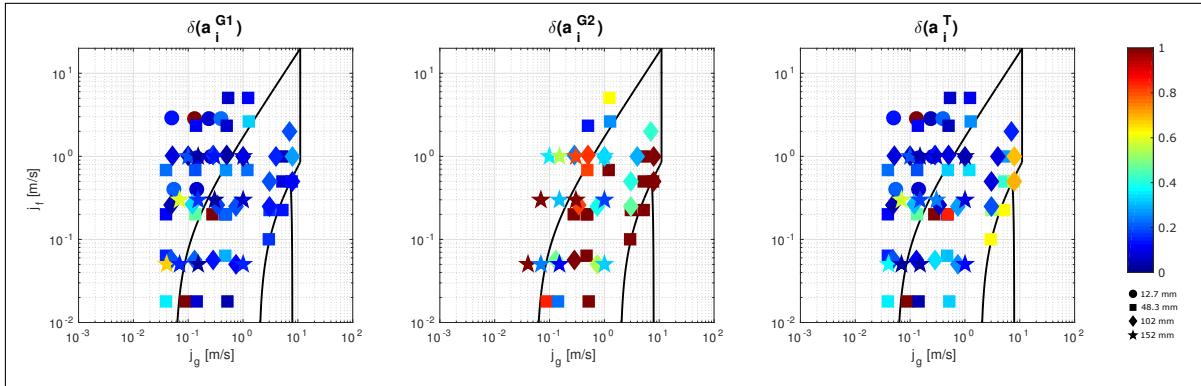


Figure 4.2: A comparison of performance for four sets of Purdue University experimental data.

Table 4.2: A comparison of average error calculated by Eq. (3.15) for 48.3 mm Purdue University tests.

		$j_g < 2 \cdot 10^{-1}$ m/s	$j_g \geq 2 \cdot 10^{-1}$ m/s
$j_f \geq 5 \cdot 10^{-1}$ m/s	G1	17.7	14.6
	G2	0.0	64.7
	T	17.7	26.6
$j_f < 5 \cdot 10^{-1}$ m/s	G1	36.0	26.9
	G2	17.6	99.3
	T	35.4	54.8

Table 4.3: A comparison of average error calculated by Eq. (3.15) for other Purdue University tests.

		$j_g < 2 \cdot 10^{-1}$ m/s	$j_g \geq 2 \cdot 10^{-1}$ m/s
$j_f \geq 5 \cdot 10^{-1}$ m/s	G1	19.6	12.7
	G2	15.0	40.6
	T	19.7	13.8
$j_f < 5 \cdot 10^{-1}$ m/s	G1	21.8	12.5
	G2	21.7	37.9
	T	17.8	12.6

In summary, previous studies and the more recent study performed within the framework of this dissertation have found that the Fu-Ishii two-group IATE model generally performs well for prediction of group-wise and total interfacial area at low superficial gas velocities. For flow conditions with $j_g \geq 2 \cdot 10^{-1}$ m/s larger group-2 bubbles appear in the flow. In general, the contribution of these larger bubbles to the overall interfacial area density is not adequately predicted. In particular, a significant disagreement with group-2 bubbles experimental data is found for both TOPFLOW DN50 (52.3 mm) and Purdue 48.3 mm database.

State of Smith-Schlegel model performance

The summary of the prediction of group-wise and total interfacial area for TOPFLOW DN200 experiments is shown in Fig. 4.3, where the figure of merit Eq. (3.15) represents the deviation of the IATE model prediction from experimental data. It was found that good performance is observed at low void fraction regimes for group-1 and deteriorates towards high superficial gas velocities. For group-2, the performance is generally poor. As mentioned previously, the good performance in the prediction of total interfacial area is achieved erroneously as group-wise errors compensate each other. The error is also tabulated

in Table 4.4. At $j_g \geq 2 \cdot 10^{-1}$ m/s, the problem of error compensation is evident as group-1 and group-2 errors are 45.0% and 72.2%, respectively, while the total error is only 13.6%.

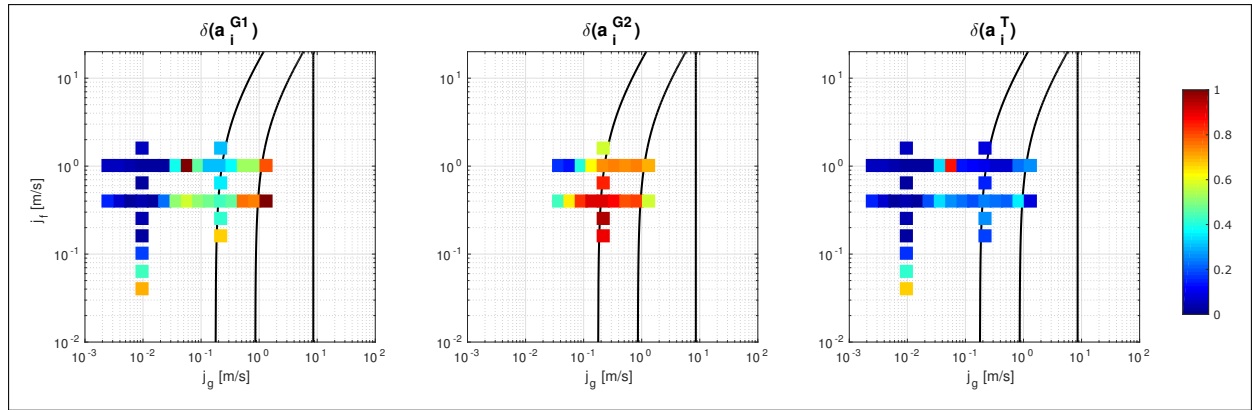


Figure 4.3: A comparison of performance for DN200 TOPFLOW data. Left column indicates error for group 1 interfacial area concentration and right column indicates error for group 2 interfacial area concentration. The third column indicates error for prediction of total interfacial area.

Table 4.4: A comparison of average error calculated by Eq. (3.15) for all TOPFLOW DN200 tests.

		$j_g \leq 10^{-2}$ m/s	10^{-2} m/s $< j_g < 2 \cdot 10^{-1}$ m/s	$j_g \geq 2 \cdot 10^{-1}$ m/s
$j_f \geq 5 \cdot 10^{-1}$ m/s	G1	4.4	36.6	45.0
	G2	0.0	25.8	72.2
	T	4.4	24.3	13.6
$j_f < 5 \cdot 10^{-1}$ m/s	G1	18.3	38.4	63.2
	G2	0.0	54.9	81.3
	T	17.5	20.3	23.1

The Purdue experiments [34] with diameters above 100 mm is also benchmarked against the Smith-Schlegel model. The summary of group-wise and total interfacial area prediction for large diameter Purdue experiments is presented in Fig. 4.4. Similar to the TOPFLOW DN200 results, the group-1 performance is good at low j_g . However, in the high void fraction flow regimes there is poor performance observed for the prediction of group-1 a_i . For group-2, significantly better performance is observed for Purdue university tests. The error for the Purdue university tests is tabulated in Table 4.5.

The contrast of poor prediction of group-2 a_i in TOPFLOW DN200 tests against poor performance of group-1 a_i in Purdue university tests can be attributed to the significant differences in hydraulic diameters. TOPFLOW DN200 pipe is significantly larger than the Purdue University pipes (198 mm vs. 102 mm and 152 mm, respectively). The TOPFLOW

DN200 pipe has almost 300% more cross-sectional area than the 102 mm Purdue pipe, and this would certainly have consequences on the incidence of mechanisms.

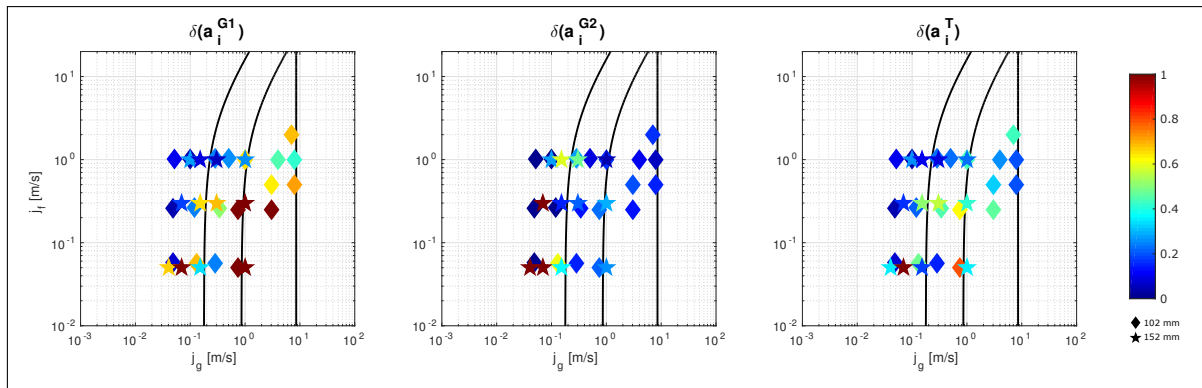


Figure 4.4: A comparison of performance for two sets of Purdue University experimental data.

Table 4.5: A comparison of average error calculated by Eq. (3.15) for large diameter Purdue University tests.

		$j_g < 2 \cdot 10^{-1}$ m/s	$j_g \geq 2 \cdot 10^{-1}$ m/s
$j_f \geq 5 \cdot 10^{-1}$ m/s	G1	12.4	32.9
	G2	21.2	20.2
	T	12.5	21.9
$j_f < 5 \cdot 10^{-1}$ m/s	G1	41.2	82.2
	G2	42.8	21.3
	T	32.1	46.9

4.1 Genetic Algorithm

The present study is focused on exploring quantitative methods to improve the overall performance of the two-group IATE models over a wide range of flow conditions. Various optimization algorithms are described in the open literature. The choice of optimization algorithm depends on the particular problem to be optimized. In the present work, the TOPFLOW experimental data are used as basis for the optimization. The following problem is posed:

$$\begin{aligned}
 &\text{Minimize } : f(\vec{x}) \\
 &\quad \vec{x} \in \mathfrak{R}^n \\
 &\text{Given } : \vec{x}_{min} \leq \vec{x} \leq \vec{x}_{max}
 \end{aligned} \tag{4.1}$$

The objective function, $f(\vec{x})$, to be used in the optimization algorithm the relative group-weighted error between IATE prediction and the corresponding experimental data. The objective function is defined by Eq. (4.2), where Z represents the total number of measured axial locations, and the subscripts indicate calculated or experimentally values of the total interfacial area concentration at location ζ . The group weighting factor, $\omega_{g,\zeta}$, allows consideration of the importance of the group-wise interfacial area contribution towards the objective function. The input, \vec{x} replaces default coefficients (\vec{C}) of the IATE model (the default coefficients of Fu-Ishii’s model are presented in Table 3.4, and Smith-Schlegel’s model in Table 3.6). The inputs are real and part of an n -dimensional domain, where n is the number of coefficients being modified, subject to varying boundaries. The lower boundary is currently set as 0 ($\vec{x}_{min} = \vec{0}$). The upper boundary is set as two order of magnitudes larger than default values ($\vec{x}_{max} = 10^2\vec{C}$).

$$f(\vec{x}) \equiv \frac{1}{Z-1} \sum_{\zeta=2}^Z \left[\omega_{1,\zeta} \left| \frac{a_{1,\zeta,calc} - a_{1,\zeta,meas}}{a_{1,\zeta,meas}} \right| + \omega_{2,\zeta} \left| \frac{a_{2,\zeta,calc} - a_{2,\zeta,meas}}{a_{2,\zeta,meas}} \right| \right] \quad (4.2)$$

In order to solve the problem, the following requirements that should be met by the optimization algorithm are defined:

- **Non-linear:** The optimization should not require numerical gradients/hessians.
- **Global:** A global (as opposed to a local) optimization that considers the entire domain of input parameters is preferred. Local optimization methods do not explore the entire domain and rely on a user defined initial location ($\in \mathfrak{R}^n$) that may be in the proximity of a local minimum and therefore limiting the opportunity of finding a global minimum.
- **Parallelizable:** It would be beneficial to utilize a method that provides multiple asynchronous inputs. This would allow simultaneous evaluations of $f(\vec{x})$, reducing the total computational time required to complete the optimization.

The genetic algorithm [24] is a heuristic search algorithm that mimics the process of natural selection. The algorithm attempts to solve optimization problems with techniques such as inheritance, mutation, selection and cross over. The following is a brief high-level description of the solution methodology of a genetic algorithm:

1. **Initialization:** A fixed population of size N (\vec{x}_i^g where $i = 1 \dots N$) is generated with random distribution $\in \mathfrak{R}^n$. The superscript g denotes the generation of the population (i.e. initially $g = 1$).

2. **Selection:** The objective function, $f(\vec{x})$, is calculated. The traits of $g + 1$ generation is determined by the performance of the g population.

- *Mutation:* The fittest solutions are selected for “breeding” and a mutation procedure determines how traits evolve over generations. Various options are available including uniform mutation or Gaussian mutation.

- *Migration:* Randomly selected populations are expected to migrate within \mathfrak{R}^n in order to minimize the chance of the algorithm missing local minima.

3. **Convergence:** The algorithm achieves a satisfactory result when $g \geq G$ (where G is a minimum amount of generations required for convergence) and the relative change in the objective function is lower than a user-defined threshold (generally 10^{-5}).

Due to the solution methodology, the genetic algorithm meets the requirements necessary to solve a non-linear, global and computationally parallelizable problem. It should be noted that although the genetic algorithm attempts to arrive at a global minimum, it does not guarantee such an outcome. Increasing the number of minimum generations can ameliorate this issue (the default minimum generations is quadrupled from 20 per n to 80 in this study).

4.1.1 Implementation

The implementation of the IATE models remain equivalent to the previous chapter (see Section 3.2.3). In order to isolate the error introduced by IATE, only two transport equations were discretized: the transport of group 1 and group 2 interfacial area. The TOPFLOW experimental data provides group-wise α_g , a_i and v_g values at several axial locations. A quadratic fit (with respect to axial location) to these field values accurately captures their advection. Using interpolated values of α_g and v_g allowed closure of the IATE. The model was discretized using a simple first order forward difference scheme. The initial condition is taken from the first experimentally measured axial location.

In discussions of optimization results, the performance of 2G IATE will be quantified by error, Eq. (3.15). The error in predicting group-wise and total interfacial area will be discussed. Two operators will be consistently used to discuss results, Eqs. (4.3) and (4.4). The operator

$$\Delta(f(\vec{x})) \equiv f(\vec{C}_{default}) - f(\vec{C}_{min}) , \quad (4.3)$$

will represent the change in the objective function (Eq. (4.2)) between two sets of coefficients

$\vec{C}_{default}$ and \vec{C}_{min} . The operator

$$\delta(C) \equiv \frac{C_{min} - C_{default}}{C_{default}}, \quad (4.4)$$

will represent the relative change for a particular coefficient. Due to the bounds introduced in Eq. (4.1), the minimum possible $\delta(C)$ is -1, and the maximum is 99.

4.2 Optimization of Fu-Ishii Model

The application of the genetic algorithm introduced in Section 4.1) is discussed in the following sections. In Section 4.2.1, the IATE model coefficients are optimized to minimize the difference between measured and computed a_i for each TOPFLOW test individually. This study is aimed at identifying the presence of eventual patterns in the optimized coefficients across the j_g-j_f space. In Section 4.2.2, the objective function is defined on the basis of the average error on interfacial area concentration over all tests and produces a single set of optimized coefficients for the IATE model. The performance of the optimized IATE model is then assessed against both the TOPFLOW DN50 tests and the Purdue tests. Lastly, in Section 4.2.3 optimization studies are presented in which the objective function targets directly an interaction mechanism that had been found responsible for the poor performance of the default IATE model in the high void fraction regime, namely the wake entrainment of large group-2 bubbles.

4.2.1 Individual Optimization

In this section, the IATE model coefficients are optimized to minimize the difference between measured and computed a_i for each single TOPFLOW test. In this way, an independent set of optimized coefficients is obtained for each individual experimental test. This study is only aimed at identifying the presence of eventual patterns in the optimized coefficients across the j_g-j_f space. Existence of patterns may imply that the genetic algorithm is able to prioritize the impact of particular interaction mechanisms as flow conditions vary. The results of the individual optimization are presented in Fig. 4.5. In the top figure, the overall improvement on the prediction of the total interfacial area concentration is shown for each point in the TOPFLOW test matrix. In the other figures, the results of the optimization for each coefficient of the IATE model is presented as variation from the coefficient default value. First, it is interesting to note that there is almost a negligible improvement in performance in interfacial area concentration for $j_g \leq 0.0151 \text{ m/s} \cap j_f \geq 0.405 \text{ m/s}$. In the previous

assessment of TOPFLOW DN50 data [14], this particular region was dominated by bubble expansion. The bubble expansion term does not rely on empirical coefficients, therefore it is to be expected that the modification of interaction mechanism coefficients will have no impact on IATE performance improvement. As highlighted in Fig. 4.1, the default Fu-

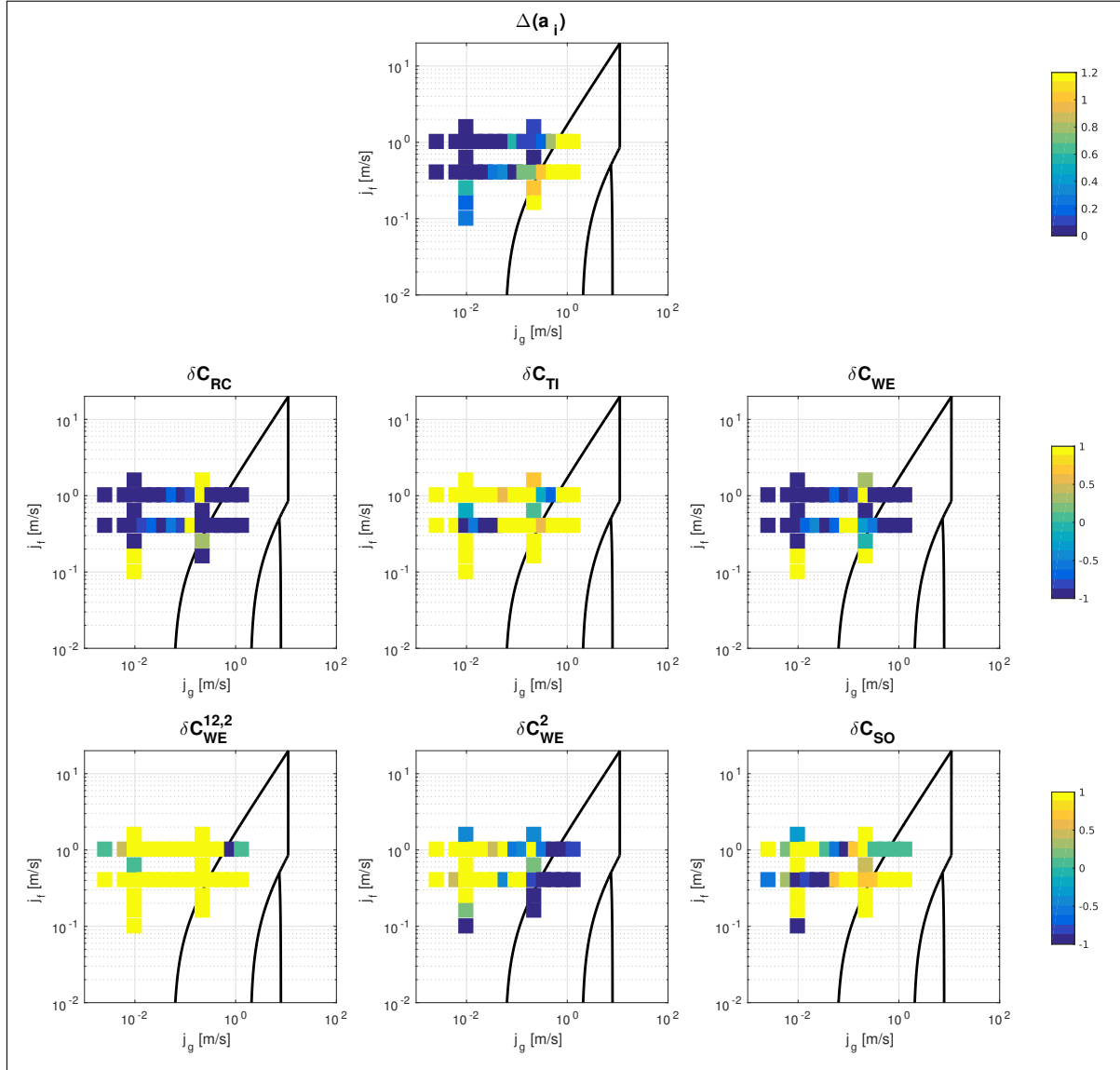


Figure 4.5: Results for optimizing individual TOPFLOW DN50 tests. The improvement in predicting interfacial area ($\Delta(a_i)$ using Eq. (4.3)) is presented at the top. The relative change in coefficient values (δC using Eq. (4.4)) is presented.

Ishii two-group IATE model exhibit poor performance in the high void fraction regimes. Therefore, as expected, the improvement of the a_i predictions after optimization is greatest for $j_g \geq 0.342$ m/s. The wake entrainment of groups-2 bubbles was found to be the dominant contributor to the degradation in model performance and therefore a large decrease in C_{WE}^2

is noted as a consequence of the optimization.

4.2.2 Global Optimization

The IATE model relies on a single set of empirical coefficients. In this section we discuss the results obtained with the optimized IATE model when all TOPFLOW DN50 tests are used simultaneously for the optimization (global optimization). Therefore, the output of the global optimization genetic algorithm is a single set of coefficients that have shown to achieve a minimal error within the assigned coefficient bounds (Section 4.1) over the entire range of liquid and gas superficial velocities. The optimized set of coefficients are reported in Table 4.6. As a result of the optimization, a significant reduction in coefficients values of random collision (C_{RC}) and wake entrainment (C_{WE}) is obtained; both coefficients only impact the sink for group-1 interfacial area concentration. There is a significant reduction of intergroup and group-2 wake entrainment ($C_{WE}^{12,2}$ and C_{WE}^2) is also obtained; both coefficients impact the sink of group-2 interfacial area concentration. There is a large increase in the turbulent impact coefficient (C_{TI}), which is a source for both group-1 and group-2 interfacial area concentration. The coefficient of shearing-off (C_{SO}) is moderately modified. These changes in coefficients result in an overall improvement of 18.4% for the objective functions.

Table 4.6: Global optimization of all TOPFLOW DN50 tests. The change in coefficients and objective function is calculated by Eq. (4.4) and Eq. (4.3), respectively.

	C_{RC}	C_{TI}	C_{WE}	$C_{WE}^{12,2}$	C_{WE}^2	C_{SO}	$f(\vec{x})$
Default	0.0041	0.0085	0.002	0.015	10.0	0.031	0.714
Optimized	2.95×10^{-5}	0.364	1.53×10^{-5}	0.00111	1.53	0.0352	0.530
δC	-0.99	42	-0.99	-0.93	-0.847	0.134	$\Delta = 0.184$

The change in error for the prediction of the interfacial area concentration (Eq. (4.2)) using the globally optimized set of coefficients is shown in Fig. 4.6. For group 1, little change in the prediction performance is observed, albeit the large decrease in C_{RC} and C_{WE} . For group 2, there are significant improvements. Notably, all improvements in performance occur at the high void fraction slug flow regime. However, the coefficient optimization does result in some deterioration for the prediction of a_i at the transition from bubbly to slug flow regime, the trade-off still being in favor of the optimized coefficients. The impact of the optimization is analyzed more in detail with Fig. 4.7, where a comparison between predicted and experimental values for the group-wise and total interfacial area concentration is reported for four experimental tests. For these tests, the prediction of the default IATE model for group-2 interfacial area concentration were particularly poor. The default Fu-Ishii

model is able to correctly capture both qualitatively as well as quantitatively the evolution of group-1 interfacial area concentration along the pipe vertical axis. However, for group 2, as the superficial liquid velocity is decreased to $j_f \leq 0.64$ m/s and below, the default model predicts a strong wake entrainment (ϕ_{WE}^2), leading to an over-prediction of the sink term for group-2 interfacial area concentration propagation. In contrast, the globally optimized coefficients retain the performance for group 1 while improving the prediction of group-2 interfacial area concentration. Looking at the mechanisms contributing to the change of group-2 interfacial area concentration (Σa_i^{G2}), it can be noticed that as a result of the optimization, a significant reduction in group 2 wake entrainment and an increase in group-2 turbulent impact is obtained, which lead to a significant improvement in the prediction of the total interfacial area for $j_f = 0.41$ m/s and $j_f = 0.26$ m/s.

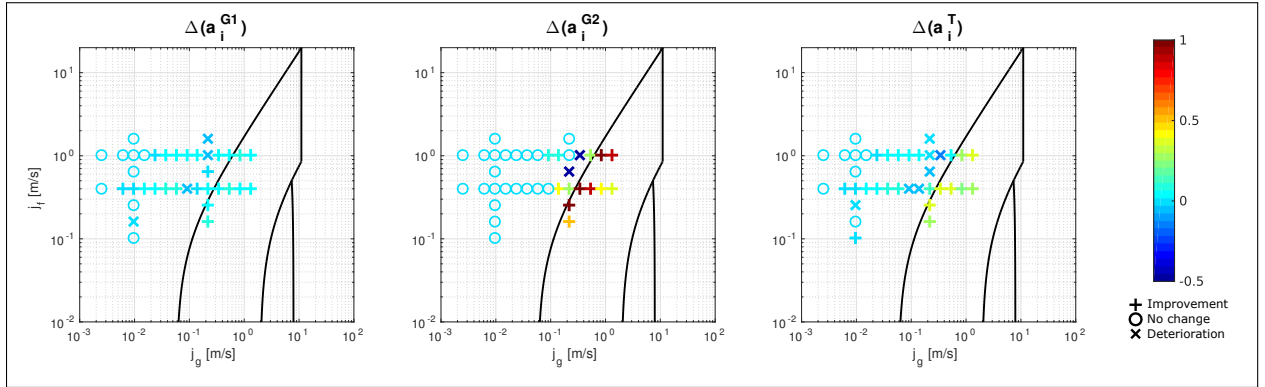


Figure 4.6: Improvement of performance for DN50 TOPFLOW data using optimized \vec{C} .

The average gain in prediction performance (in percentage) in different regions of the j_g-j_f space is shown in Table 4.7. For $j_g \leq 10^{-2}$ m/s, a negligible improvement (up to 0.4%) in the IATE model prediction of the group-wise (G1 and G2) and total (T) interfacial area concentration is found. This result is expected, given that at these flow conditions the propagation of the interfacial area concentration is mostly driven by bubble expansion. For 10^{-2} m/s $< j_g < 2 \cdot 10^{-1}$ m/s, the prediction for interfacial area concentration of both group 1 and 2 (and thus total interfacial area) improve by 1% to 3%. However, the most significant improvements are obtained for $j_g \geq 2 \cdot 10^{-1}$ m/s, where the observed improvements for group-2 and total interfacial area concentration are up to 43% and 28% respectively.

It is interesting to analyze how the IATE model, optimized on the basis of the TOPFLOW data, performs against a set of independent experiments (e.g. the Purdue tests [34] presented in Fig. 4.2). The improvement of the performance of the optimized IATE model with respect to the default model for the prediction of the Purdue tests is shown in Fig. 4.8 and Tables 4.8 and 4.9. In Fig. 4.8, it can be seen that the optimized IATE model performs better than the

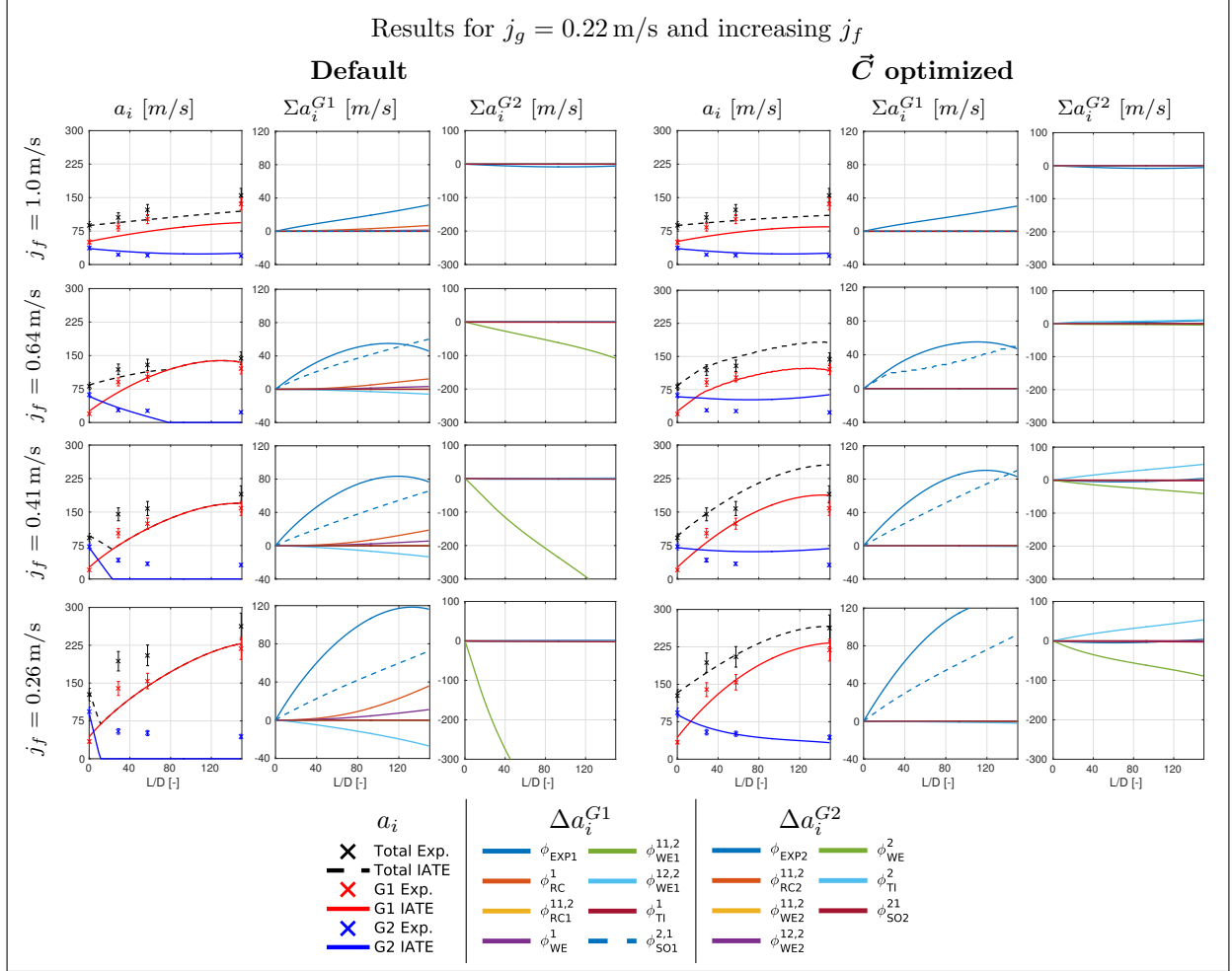


Figure 4.7: Results for Tests 115 to 118 using the 2G IATE model.

default model over the entire range of available tests. Similar to what noted for TOPFLOW DN50, most of the improvement occurs for group-2 bubbles in high void-fraction regimes. Group 1 generally has moderate benefit from the optimized coefficients.

The quantitative performance for the Purdue 48.3 mm diameter tests is tabulated in Table 4.8. A significant performance gain in the prediction of the total interfacial area is obtained at low j_g – j_f , where improvements of up to 25% are observed. At high j_g and j_f improvements above 12% are noted. Performance improvements for all other Purdue tests (test sections of different diameters) are presented in Table 4.9. While at low j_f , there is an improvement in prediction of total interfacial area, a decrease in performance is observed for $j_f \geq 5 \cdot 10^{-1}$ m/s. It is not surprising that the optimized model performs best for independent tests carried out on a test section of similar diameter as the one used for the model optimization. If the optimized model is used for smaller or larger diameters, the benefits are a trade-off for improved performance at lower j_f .

Table 4.7: Average error gain/loss calculated by Eq. (3.15) for all TOPFLOW DN50 tests using optimized \vec{C} .

Gain vs. Loss		$j_g \leq 10^{-2}$ m/s	10^{-2} m/s $< j_g < 2 \cdot 10^{-1}$ m/s	$j_g \geq 2 \cdot 10^{-1}$ m/s
$j_f \geq 5 \cdot 10^{-1}$ m/s	G1	0.4	2.61	1.6
	G2	0.0	2.3	13.6
	T	0.4	2.4	5.7
$j_f < 5 \cdot 10^{-1}$ m/s	G1	0.3	3.2	5.0
	G2	0.0	1.2	42.8
	T	0.1	2.2	28.1

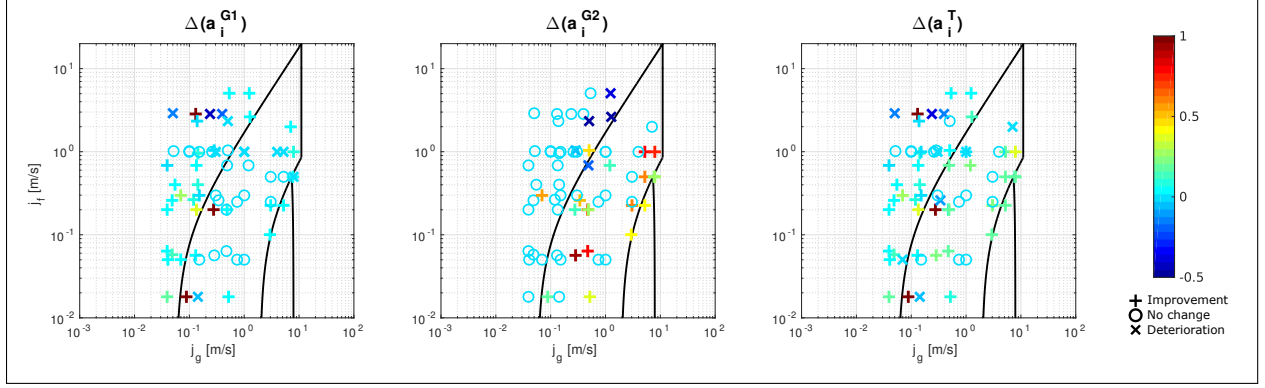


Figure 4.8: Improvement of performance for Purdue University data using optimized \vec{C} .

Table 4.8: Average error gain/loss calculated by Eq. (3.15) for 48.3 mm Purdue tests using optimized \vec{C} .

Gain vs. Loss		$j_g < 2 \cdot 10^{-1}$ m/s	$j_g \geq 2 \cdot 10^{-1}$ m/s
$j_f \geq 5 \cdot 10^{-1}$ m/s	G1	2.6	1.4
	G2	0.0	9.1
	T	2.6	12.4
$j_f < 5 \cdot 10^{-1}$ m/s	G1	14.0	12.1
	G2	2.8	30.5
	T	24.9	15.5

In order to understand how changes to coefficients impact the objective function, the principal component analysis (PCA) is discussed next. PCA allows a multi-dimensional set of data to be projected onto new principal components that account for the largest variance. In the PCA presented here, each observation has been weighted by $1/\exp(f(\vec{x}))$. Therefore, changes to coefficients that produce the lowest average error have a higher weight. The PCA will only consider 50th percentile (in terms of lowest objective function value) and above candidates. The resulting principal components are shown in Table 4.10. The cumulative variance ($\sum \sigma^2$) of the first principal component is 98.7% and the second principal

Table 4.9: Average error gain/loss calculated by Eq. (3.15) for other Purdue tests using optimized \vec{C} .

Gain vs. Loss		$j_g < 2 \cdot 10^{-1}$ m/s	$j_g \geq 2 \cdot 10^{-1}$ m/s
$j_f \geq 5 \cdot 10^{-1}$ m/s	G1	0.8	7.3
	G2	0.0	4.4
	T	0.6	4.3
$j_f < 5 \cdot 10^{-1}$ m/s	G1	6.7	4.87
	G2	0.5	9.3
	T	6.2	1.0

component reaches 99.9%, both vectors have significant values for C_{WE}^2 and C_{TI} , respectively. Therefore, the first two principal components indicate that the improvement of the objective function Eq. (4.2) in a global optimization is *most* sensitive to changes in C_{WE}^2 , followed by C_{TI} . A projection of the principal components and observations is reported in Fig. 4.9. Qualitatively, a majority of the patterns formed by the observations are aligned to the principal components, confirming the validity of the principal components. PCA indicates that a significant potential to improve the IATE performance rests within a single coefficient, C_{WE}^2 . The coefficient of wake entrainment for group two was indeed found to be a major contributor to the poor performance of group-2 a_i propagation in high void-fraction flow regimes [14]. As indicated by the individual optimizations (Section 4.2.1), little potential to improve performance at low void fractions exists. Thus, the sensitivity of the global objective function to C_{WE}^2 is justified.

Table 4.10: Principal components of genetic algorithm candidates in optimization of all Fu-Ishii coefficients for TOPFLOW DN50.

	\vec{PC}_1	\vec{PC}_2	\vec{PC}_3	\vec{PC}_4	\vec{PC}_5	\vec{PC}_6
C_{RC}	0.000	0.000	0.002	0.005	0.123	0.992
C_{TI}	0.275	0.962	0.002	0.000	-0.001	0.000
C_{WE}	0.001	0.001	0.017	0.004	0.992	-0.124
$C_{WE}^{12,2}$	0.018	-0.007	0.883	-0.470	-0.013	0.002
C_{WE}^2	0.961	-0.274	-0.025	-0.006	-0.001	0.000
C_{SO}	0.016	-0.006	0.469	0.883	-0.012	-0.003
$\sum \sigma^2$	0.987	0.999	1.000	1.000	1.000	1.000

4.2.3 Localized Optimization of Group-2 Wake Entrainment

In the previous section, it has been concluded that the largest impact to improvement of the Fu-Ishii two-group IATE model is obtained by modifying the group-2 wake entrainment

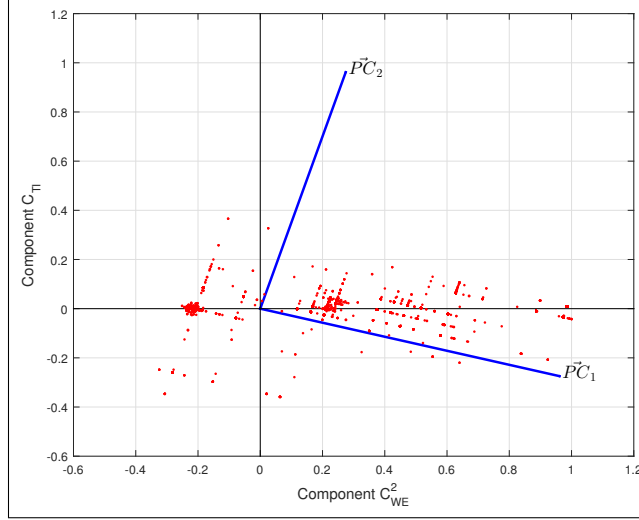


Figure 4.9: Principle components biplot for 50th percentile and above genetic algorithm candidates.

(C_{WE}^2). In the global optimization discussed in the previous section, the accuracy of the IATE model is accounted for all tests, including those in low void fraction regimes that do not have group-2 bubbles. In this section, a set of tests among the TOPFLOW data are selected that exhibit a strong group-2 wake entrainment. In particular, tests 105, 114, 115, 116, 117, and 127 are chosen (Table 3.2). These tests have experimental conditions that are alike, in terms of superficial velocities. It is therefore expected that optimizing the group-2 wake entrainment coefficient on these tests should improve performance in other tests at high void fractions.

The results from the optimization are presented in Table 4.11. The value of the objective function (Eq. (4.2)) is improved by over 40%, and the value of the group-2 wake entrainment coefficient is decreased by 95%. The results of using the optimized C_{WE}^2 coefficients are reported in Fig. 4.10. Similar to the global optimization, a majority of the improvement in performance occurs in the high void fraction region for group-2 bubbles. This manifests in a significant improvement in the total interfacial area prediction. The group-1 performance is not expected to change drastically. Changes in average error is tabulated in Table 4.12. Quantitatively, negligible changes in performance are noted for $j_g < 2 \cdot 10^{-1}$ m/s. For $j_g \geq 2 \cdot 10^{-1}$ m/s \cap $j_f < 5 \cdot 10^{-1}$ m/s, significant improvement is noted resulting in about 33% improvement in total a_i prediction. In contrast, the global optimization achieved an improvement of 28%.

The application of optimized C_{WE}^2 to several tests is shown in Fig. 4.11. As described in the previous section, tests 115 to 118 suffer from an increasing over-prediction of group-2 wake entrainment as the gas superficial velocity increases. On the right hand side of the

Table 4.11: Results for localized optimization of group 2 wake entrainment.

	C_{WE}^2	$f(\vec{x})$
Default	10.0	1.31
Optimized	0.515	0.875
δC	-0.95	$\Delta = 0.435$

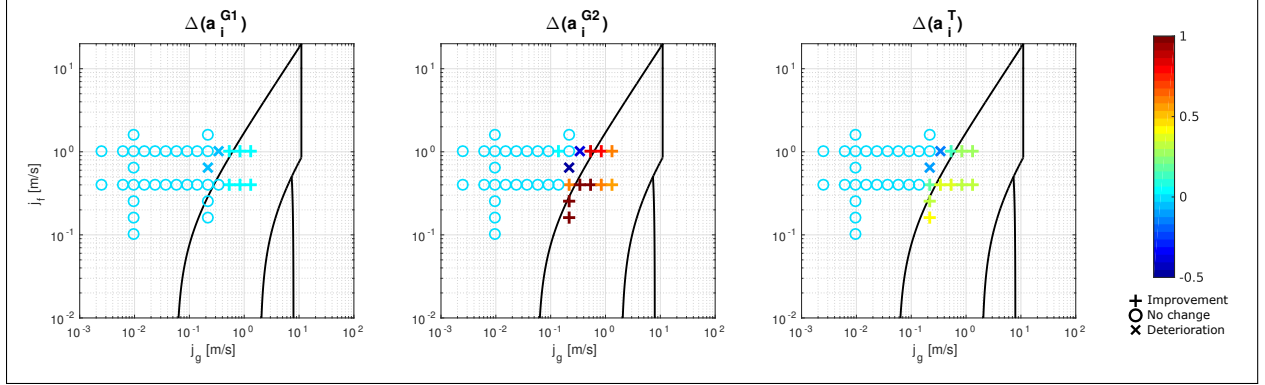


Figure 4.10: Improvement of performance for TOPFLOW DN50 data using optimized C_{WE}^2 .

figure, the corresponding results with the optimized C_{WE}^2 are presented. For the cumulative group 2 source contribution, Σa_i^{G2} , there is a significant reduction in the contribution from ϕ_{WE}^2 , as expected. The optimization significantly improves the qualitative prediction of group-2 a_i . The total interfacial area is also propagated correctly within the experimental uncertainty bars at low L/D. The propagation of group-1 a_i is not affected.

In the previous section, we have discussed a global optimization of the IATE model for all its coefficients, on the basis of the entire TOPFLOW database. The current section instead is focused on the optimization of a single coefficient (the group-2 wake entrainment) on the basis of 6 TOPFLOW tests. Nevertheless, it is found that the benefits of this more limited model optimization are significant for neighboring tests too. When the optimized C_{WE}^2 coefficient is applied to Purdue tests, the outcome is positive. Fig. 4.12 presents the individual change in performance for all Purdue tests. Similar to TOPFLOW, the prediction of group-1 interfacial area concentration sees no degradation/improvement, yet the prediction of group-2 a_i improves mostly in the higher void fraction region. Table 4.13 tabulates the change in average error for 48.3mm Purdue tests. A significant margin of 24% improvement for the total a_i is observed for high superficial gas to velocity ratio region, while no degradation in performance is noted on average; in fact, a better improvement is obtained than with the globally optimized coefficients. Table 4.14 tabulates changes in performance for all other Purdue tests. In contrast to the net neutral change in performance noted for the globally optimized coefficients (Table 4.9), there are only gains for this case.

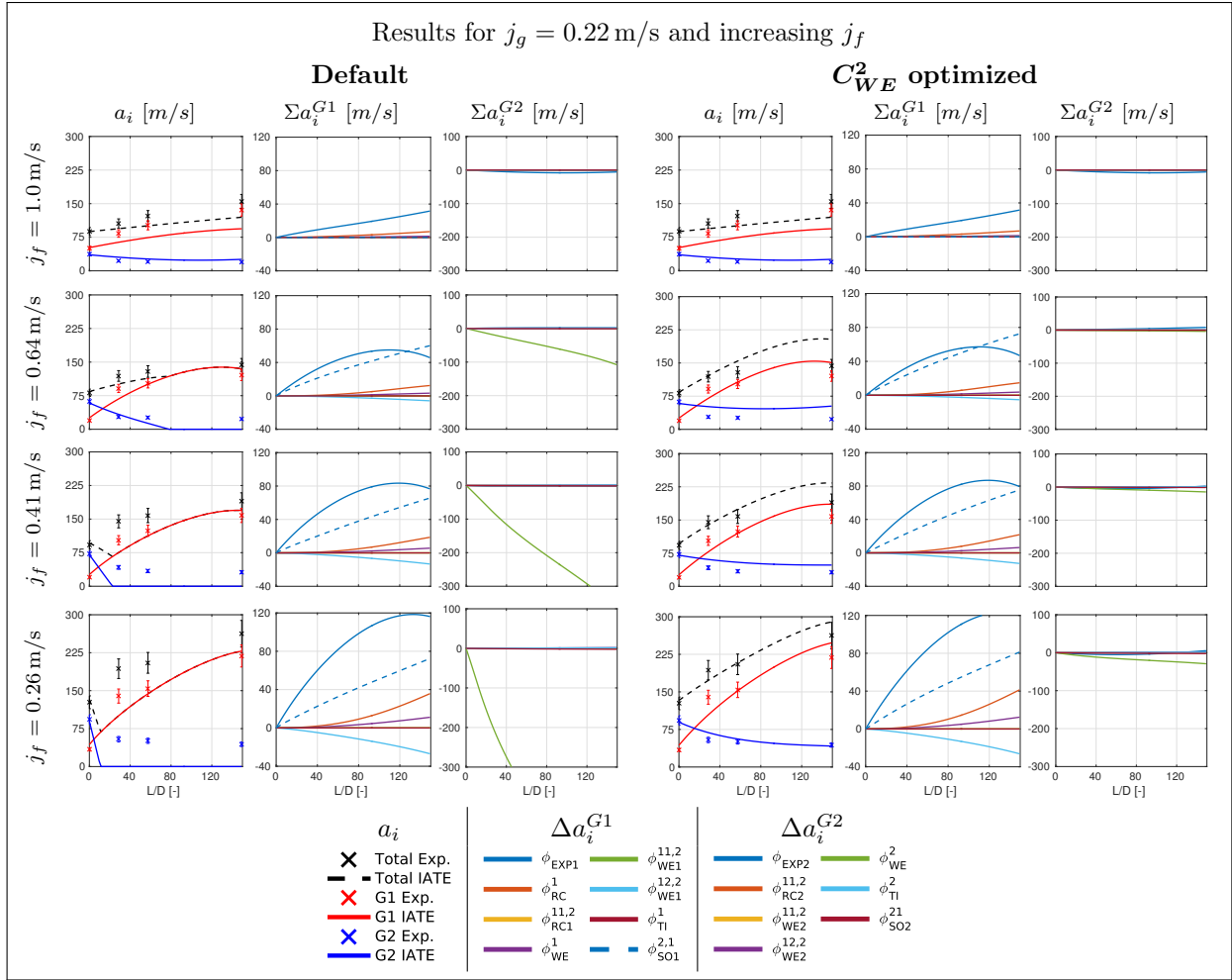


Figure 4.11: Results for Tests 115 to 118 using the 2G IATE model.

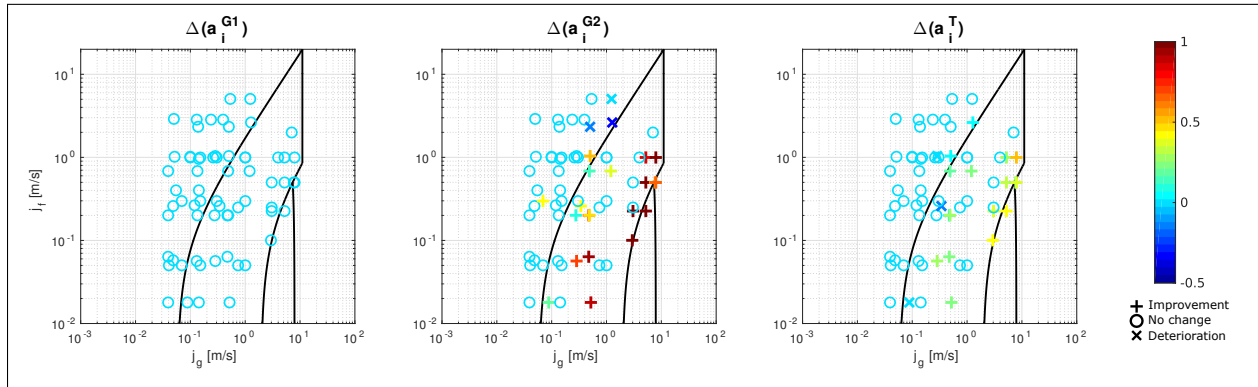


Figure 4.12: Improvement of performance for Purdue University data using optimized C_{WE}^2 .

Two important outcomes can be drawn from the results presented in this section. First, the selection of the objective function for the optimization requires an informed input by the

Table 4.12: Average error gain/loss calculated by Eq. (3.15) for TOPFLOW DN50 tests using optimized C_{WE}^2 .

Gain vs. Loss		$j_g \leq 10^{-2}$ m/s	10^{-2} m/s $< j_g < 2 \cdot 10^{-1}$ m/s	$j_g \geq 2 \cdot 10^{-1}$ m/s
$j_f \geq 5 \cdot 10^{-1}$ m/s	G1	0.0	0.0	0.1
	G2	0.0	0.3	16.1
	T	0.0	0.0	6.3
$j_f < 5 \cdot 10^{-1}$ m/s	G1	0.0	0.0	1.2
	G2	0.0	0.0	60.4
	T	0.0	0.1	32.7

Table 4.13: Average error gain/loss calculated by Eq. (3.15) for 48.3 mm Purdue tests using optimized C_{WE}^2 .

Gain vs. Loss		$j_g < 2 \cdot 10^{-1}$ m/s	$j_g \geq 2 \cdot 10^{-1}$ m/s
$j_f \geq 5 \cdot 10^{-1}$ m/s	G1	0.0	0.0
	G2	0.0	19.0
	T	0.0	13.3
$j_f < 5 \cdot 10^{-1}$ m/s	G1	0.0	0.1
	G2	3.0	59.0
	T	0.0	24.0

Table 4.14: Average error gain/loss calculated by Eq. (3.15) for other Purdue tests using optimized C_{WE}^2 .

Gain vs. Loss		$j_g < 2 \cdot 10^{-1}$ m/s	$j_g \geq 2 \cdot 10^{-1}$ m/s
$j_f \geq 5 \cdot 10^{-1}$ m/s	G1	0.0	0.0
	G2	0.0	7.9
	T	0.0	3.8
$j_f < 5 \cdot 10^{-1}$ m/s	G1	0.0	4.8
	G2	0.0	7.4
	T	0.1	1.1

user to achieve a generalized improvement in IATE performance. The optimization of the sole C_{WE}^2 coefficient based on a limited selection of tests (where the respective mechanism is prevalent) is significantly more successful than a brute force global optimization of all coefficients for all tests. The reduction of C_{WE}^2 from the default value of 10.0 to 0.515 results in gains in performance for all experimental databases. Secondly, the studies have shown that while the magnitude of improvement in performance for alike hydraulic diameters is similar, a significantly lesser improvement is noted for smaller or larger diameters. Therefore, due to scaling effects with respect to the hydraulic diameter, there is a limit to the universality of optimized coefficients that can be reasonable achieved.

4.2.4 Remarks

The IATE model has been shown to perform well in the bubbly flow regime for several hydraulic diameters, yet poor predictions have been observed at high void fraction, mostly due to the erroneous propagation of group-2 bubbles (see Section 3.3.2 for details). The present section has been focused on the improvement of the performance of the Fu-Ishii model for small diameter pipes. The high-resolution database of the TOPFLOW DN50 facility (utilizing wire-mesh sensors) is used as the basis for Fu-Ishii IATE model evaluation and optimization. Improvements in the model performance are obtained using a genetic algorithm, which attempts to modify the default closure coefficients in order to arrive at a global minima for selected figure of merits, namely the group-wise and total interfacial area concentration.

Optimization of model coefficients based on individual TOPFLOW tests, although not practical for implementation, have helped reveal important effects. First, for $j_g \leq 0.0151$ m/s $\cap j_f \geq 0.405$ m/s, almost no improvement to the current performance of the Fu-Ishii IATE is possible through any modification of the model coefficients. This because at these flow conditions, the propagation of interfacial area concentration is dominated by the bubble expansion term, which is driven by variation in pressure head and therefore does not rely on any closure coefficients. Secondly, the individual optimizations indicated that the highest region for improvement in performance is the high void fraction region for $j_g \geq 2 \cdot 10^{-1}$ m/s. The coefficient exhibiting the largest variation as a result of the optimization was the wake entrainment for group 2, C_{WE}^2 , which had to be drastically reduced. This particular mechanism has been found to be the major contributor to the over-estimation of the sink for group-2 a_i .

The global optimization of all IATE coefficients based on all TOPFLOW DN50 data was considered. This resulted in a set of coefficients that decreased average error in prediction of total interfacial area by 18.4% for TOPFLOW tests. A majority of the improvement stemmed from the high void fraction slug flow regime. Application of the optimized coefficients to independent Purdue data indicated that the modification of the default coefficients using a global optimization had a significant improvement for tests with similar hydraulic diameters. For smaller and larger diameter tests, the result was neutral, with improved performance at lower j_f at the cost of degradation at the opposite spectrum. The principal component analysis of all the observations during the optimization procedure indicated a very high sensitivity of the objective function $f(\vec{x})$ to the value of the group-2 wake entrainment coefficient C_{WE}^2 .

The last optimization study focused on the modification of the sole group-2 wake entrainment coefficient C_{WE}^2 on the basis of six neighboring TOPFLOW tests where an over-

prediction of the incidence of group-2 wake entrainment mechanism was observed. The optimization resulted in a reduction of the default coefficient from 10.0 to 0.515. The modification of the group-2 wake entrainment coefficient resulted in a significant improvement of the prediction of the total a_i for TOPFLOW tests with $j_g \geq 2 \cdot 10^{-1}$ m/s, namely 6.3% for $j_f \geq 5 \cdot 10^{-1}$ m/s and 32.7% for $j_f < 5 \cdot 10^{-1}$ m/s. The application of the modified coefficient to Purdue 48.3 mm tests resulted in improvements of 13.3% and 24.0% for group-1 and group-2 a_i predictions, respectively. Application to other Purdue university tests (with smaller and larger diameters) indicated smaller improvement of 3.8% and 1.1% respectively, but negligible degradation in performance.

Several conclusions can be drawn from the investigations presented here. The first is that the IATE model correctly predicts which regions in j_g-j_f space are dominated by bubble expansion. Secondly, a global optimization of the IATE model coefficient will not necessarily result in a generalized improvement of the IATE performance, although the use of principal component analysis allows to determine the coefficients (and therefore the mechanisms) that play the strongest role in minimizing the errors in the prediction of the group-wise and total interfacial area. The optimization of the group-2 wake entrainment coefficient C_{WE}^2 on the basis of few selected experimental tests resulted in a larger improvement of the IATE model across all experimental databases analyzed in the present work. While the optimization studies have provided a path towards improvement of current IATE models, they have also indicated that the ceiling for improvement is dictated by the geometry of the experimental database used as a basis for the genetic algorithm and the lack of scalability of two-phase flow for larger or smaller pipe diameters. The study recommends a decrease of C_{WE}^2 to 0.515.

4.3 Optimization of Smith-Schlegel Model

The optimization methodology used for studying the Fu-Ishii model is also applicable to the Smith-Schlegel model. However, while the Fu-Ishii has 6 closure coefficients, the Smith-Schlegel model requires 10. This is due to the larger number of interaction mechanisms that are considered to occur in large diameter pipes (a full list of interactions is provided in Table 3.6).

4.3.1 Individual Optimization

The result of optimization when the objective function ($f(\vec{x})$) considers each test individually is presented in Fig. 4.13. A small portion of experimental tests at high j_f and low j_g

experience no benefit from any optimization of coefficients. This indicates that the bubble expansion term is dominating in this small range of flow conditions. However, the majority of tests do benefit from optimization of the coefficients. In particular the tests with a high superficial gas-to-liquid velocity ratio have a greater potential for model performance improvement.

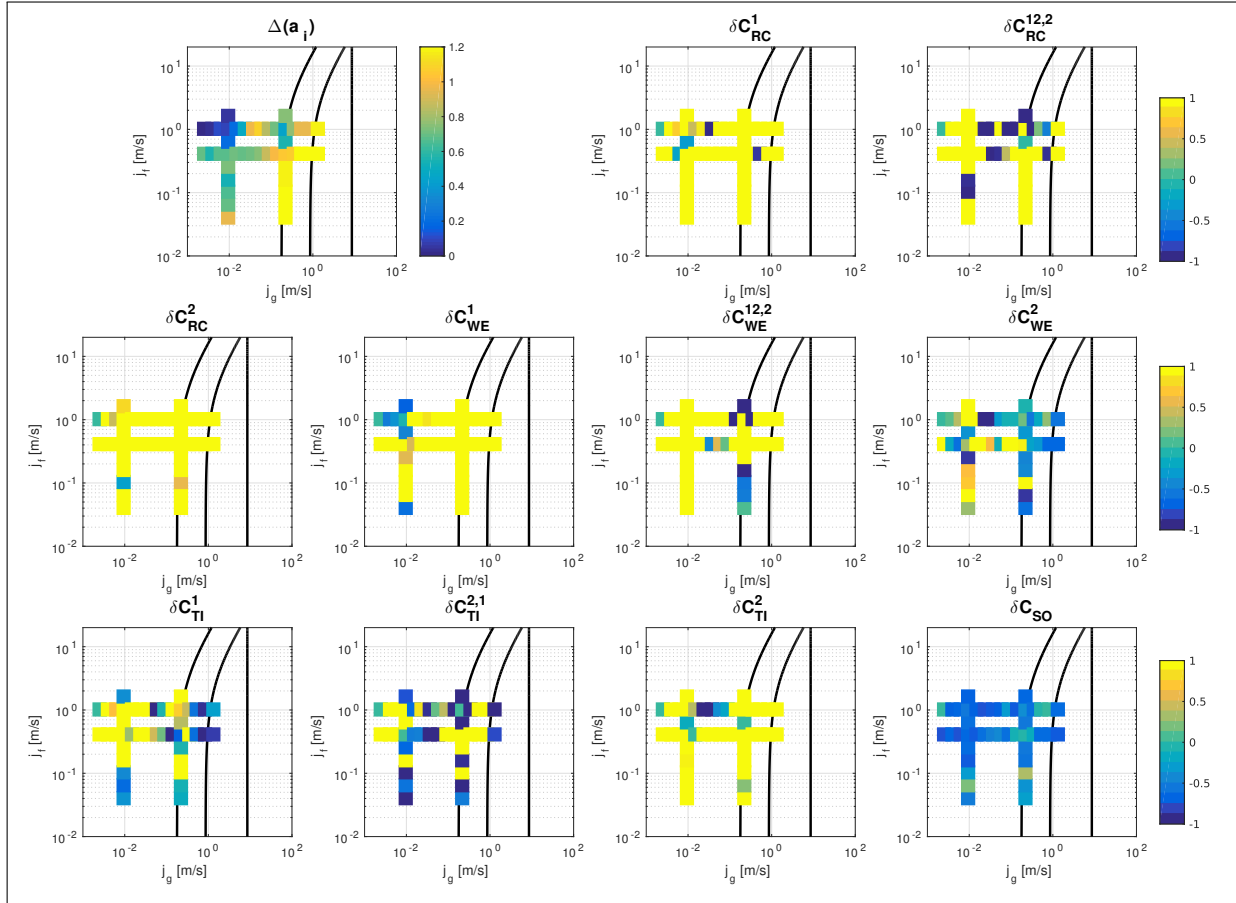


Figure 4.13: Results for optimizing individual TOPFLOW DN200 tests. The improvement in predicting interfacial area ($\Delta(a_i)$ using Eq. (4.3)) is presented at the top. The relative change in coefficient values (δC using Eq. (4.4)) is presented.

It is interesting to note that both C_{WE}^2 and C_{SO} are suggested to decrease in value for high void-fraction conditions. This is in accordance to the conclusions of the assessment of the original Smith-Schlegel evaluation (see Section 3.4.4), for which both mechanisms were identified as the cause for the poor prediction of group-2 a_i . This implies that although the objective function is only considering individual tests, the local physics in j_g-j_f space is retained by the IATE model.

4.3.2 Global Optimization

In this section, the objective function $f(\vec{x})$ considers performance of the IATE model across all TOPFLOW DN200 tests concurrently. The result of the global optimization is presented in Table 4.15. The objective function decreases by 20%, which is a significant improvement. The optimization suggests a noticeable reduction of C_{WE}^2 and C_{SO} (as discussed above, both coefficients caused significant deterioration in performance for DN200 evaluations). It is important to note that C_{RC}^2 is suggested to increase towards the bounded limit as $\delta(C_{RC}^2) = 0.99$. Increasing the bounds may lead to a larger margin of improvement. The improvement for TOPFLOW DN200 tests using the globally optimized coefficient set is presented in Fig. 4.14. It is remarkable that, although there are significant improvements to both group-wise performance, the prediction of the total interfacial area concentration is not improved and in fact displays a loss of performance.

Table 4.15: Global optimization of all TOPFLOW DN200 tests. The change in coefficients and objective function is calculated by Eq. (4.4) and Eq. (4.3), respectively.

	C_{RC}^1	$C_{RC}^{12,2}$	C_{RC}^2	C_{WE}^1	$C_{WE}^{12,2}$	$f(\vec{x})$
Default	0.01	0.05	0.01	0.002	0.02	0.362
Optimized	0.26	0.41	1.00	0.000	0.017	0.159
δC	24.9	7.2	99.0	-0.98	-0.14	$\Delta = 0.203$
	C_{WE}^2	C_{TI}^1	$C_{TI}^{2,1}$	C_{TI}^2	C_{SO}	
Default	0.05	0.05	0.02	0.01	$5.0 \cdot 10^{-5}$	
Optimized	0.021	0.013	0.006	0.023	$1.4 \cdot 10^{-5}$	
δC	-0.58	-0.73	-0.70	1.29	-0.72	

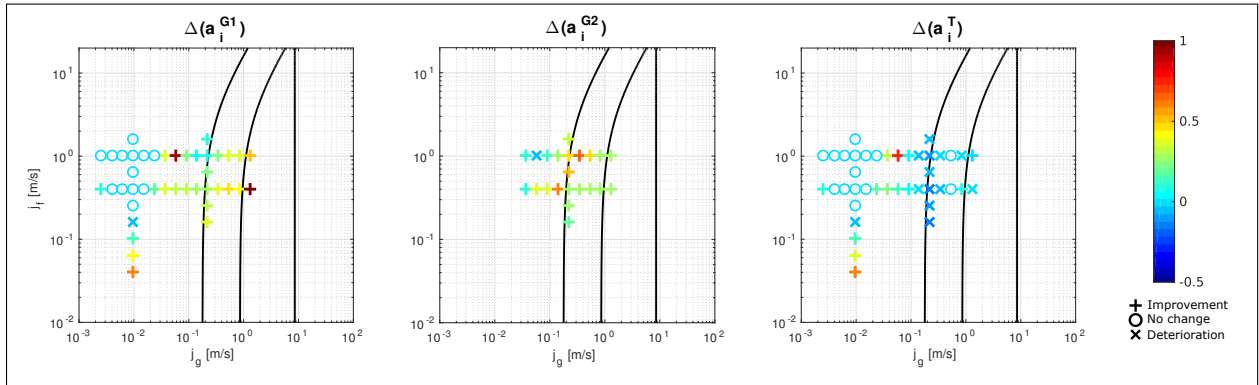


Figure 4.14: Improvement of performance for TOPFLOW DN200 data using optimized \vec{C} .

The results of the globally optimized coefficients on TOPFLOW DN200 are tabulated in Table 4.16. As discussed in Section 3.4.4, the Smith-Schlegel model presents good per-

formance for the total a_i at high void fractions. However, this is achieved through error compensation of the group-wise a_i . Therefore, although group-1 and group-2 prediction is improved by 25%-30% and 25%-40% respectively, there is an overall deterioration in total a_i of -4%. The impact of this outcome is realized for Test 160, presented in Fig. 4.15. For Test 160, the qualitative performance is indeed improved for both group-1 and group-2. However, the magnitude is still severely lacking. In the intermediate j_g range, there is significant improvement in performance in both group-wise and total interfacial area. A significant improvement in group-1 performance is also noted at low superficial gas and liquid velocity

Table 4.16: Average error gain/loss calculated by Eq. (3.15) for all TOPFLOW DN200 tests using optimized \vec{C} .

Gain vs. Loss		$j_g \leq 10^{-2}$ m/s	10^{-2} m/s $< j_g < 2 \cdot 10^{-1}$ m/s	$j_g \geq 2 \cdot 10^{-1}$ m/s
$j_f \geq 5 \cdot 10^{-1}$ m/s	G1	0.1	24.4	26.8
	G2	0.0	12.3	41.3
	T	0.1	16.3	-3.6
$j_f < 5 \cdot 10^{-1}$ m/s	G1	13.3	24.2	32.3
	G2	0.0	32.4	26.8
	T	12.5	9.1	-3.5

The TOPFLOW DN200 optimized coefficients are applied to the large diameter Purdue university tests. The improvement in performance is presented in Fig. 4.16 and tabulated in Table 4.17. While there is a significant improvement in performance for group-1, there is a large deterioration for group-2. The deterioration in prediction of group-2 a_i for Purdue university experiments is in direct contrast to the significant improvement in prediction of group-2 a_i obtained for TOPFLOW DN200 test cases (Table 4.16). As noted earlier when discussing Tables 4.4 and 4.5, there is a significant discrepancy in the performance of the original Smith-Schlegel model when assessed against the two independent experimental databases. The result indicates that the optimization on the basis of TOPFLOW DN200 experiments is not applicable to flow conditions in other hydraulic diameters (i.e. the large diameter Purdue experiments).

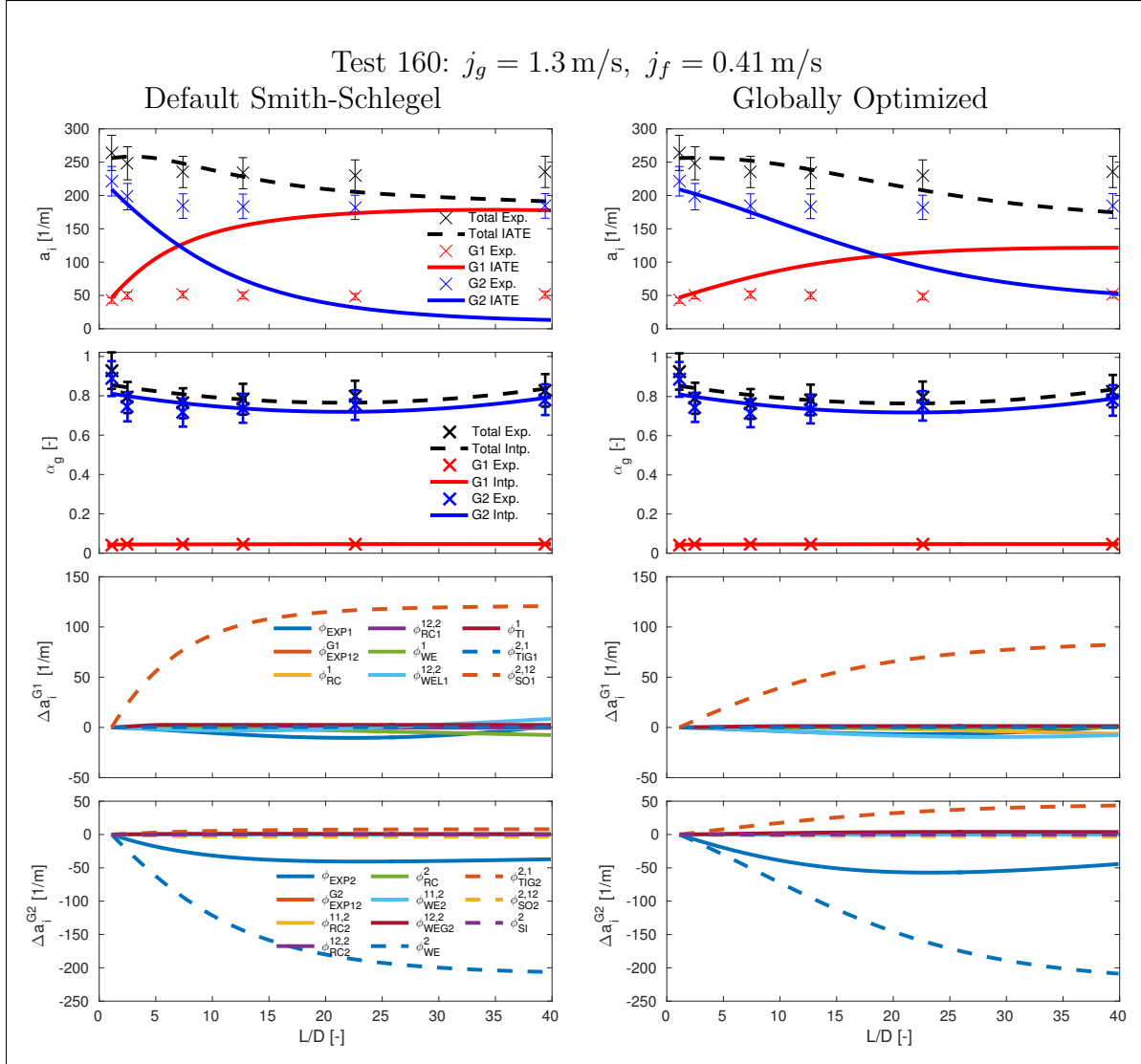


Figure 4.15: Improvement of Smith-Schlegel performance for Test 160. Both tests use the same legends.

Table 4.17: Average error gain/loss calculated by Eq. (3.15) for for large diameter Purdue tests using optimized \vec{C} .

Gain vs. Loss		$j_g < 2 \cdot 10^{-1} \text{ m/s}$	$j_g \geq 2 \cdot 10^{-1} \text{ m/s}$
$j_f \geq 5 \cdot 10^{-1} \text{ m/s}$	G1	3.5	20.1
	G2	-14.6	-32.3
	T	3.9	11.8
$j_f < 5 \cdot 10^{-1} \text{ m/s}$	G1	21.3	38.8
	G2	7.6	-19.7
	T	15.7	13.2

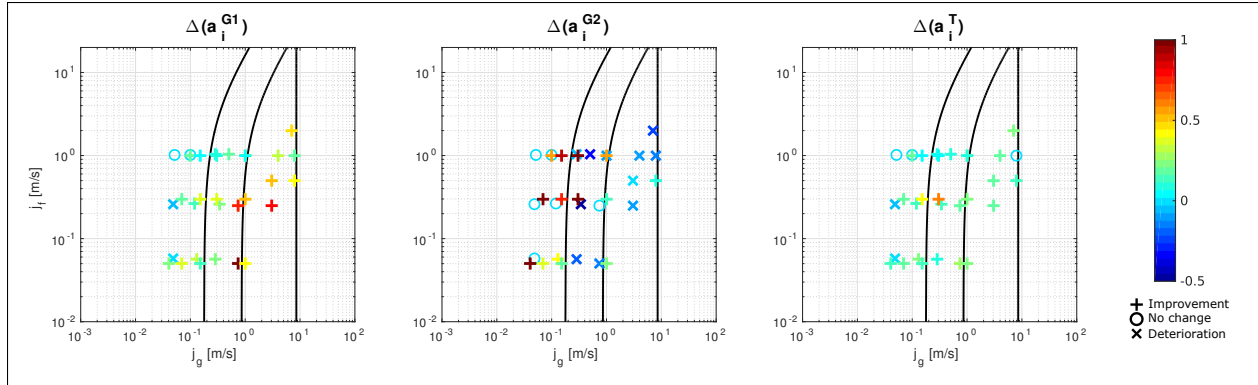


Figure 4.16: Improvement of performance for large diameter Purdue tests using optimized \vec{C} .

4.3.3 Remarks

A substantial improvement in group-wise performance could be realized only by significant changes to all 10 coefficients in the Smith-Schlegel model. While for the Fu-Ishii model, a principal component analysis could be used to single out the bubble break-up and coalescence mechanisms that mostly contributed to a poor performance of the model, for the Smith-Schlegel model such degeneration of most relevant bubbles interaction mechanisms was not successful.

The optimization results in improved predictions of the total interfacial area concentration at $j_g \leq 2 \cdot 10^{-1} \text{m/s}$, and in a performance deterioration slightly above this range. This is due to the issues associated with the default Smith-Schlegel model, for which it was found that the good performance for total a_i was a result of error compensation in the group-wise a_i predictions. Unfortunately, when the globally optimized coefficients on the basis of TOPFLOW DN200 data are applied to independent large diameter data obtained at Purdue, the results are unsatisfactory. There is a significant deterioration in the prediction of group-2 a_i , while total interfacial area prediction improves moderately. As the outcome in improvement of Purdue university tests are opposite to the TOPFLOW improvements, the application of the optimized coefficients is invalid. This may be attributed to the significantly larger hydraulic diameter of the TOPFLOW pipe and a lack of scalability of two-phase flows at these conditions. The unsatisfactory results also draw attention to the complexity of the Smith-Schlegel model. It includes a large number of mechanisms with a strong empirical nature, including 10 coefficients to be experimentally determined. Contrary to flow conditions in small diameter pipes, in flows in large diameter pipes it is more difficult to isolate individual mechanisms in the various parts of the $j_g - j_f$ space, making it difficult to experimentally determine a valid set of model coefficients.

Chapter 5

Conclusions

In an attempt to address the drawbacks of static flow regime maps, widely used in two-fluid model closure, the interfacial area transport equation model (IATE) was first proposed by Kocamustafaogullari and Ishii [42]. Past validation efforts published in the open literature have suffered from the lack of detailed experimental data, especially for flows characterized by high void-fractions, in the slug and churn turbulent flow regimes. The present dissertation is aimed at advancing the state-of-the-art on current IATE models validation and optimization, on the basis of a high-resolution experimental database including both a small (DN50) and a large (DN00) pipe diameter test section. The work-horse for the high-resolution experiments are wire-mesh sensors, able to measure local instantaneous void-fraction distributions with a resolution of 3 mm and up to 10,000 images/s. Both the Fu-Ishii model, developed for small diameter pipes, and the Smith-Schlegel model, developed for large diameter pipes, were investigated. In particular, this dissertation has focused on:

- Assessing the uncertainty in the reconstruction of interfacial area from wire-mesh sensors data,
- Assessing the performance of current IATE models against the novel high-resolution database based on wire-mesh sensor measurements,
- Exploring the use of generic algorithms to improve the performance of current IATE models across all experimental databases available in the literature .

Accuracy of wire-mesh sensor measurements of interfacial area concentration

A detailed investigation based on user-defined synthetic bubble distributions has shown that the uncertainty introduced by the interfacial area reconstruction algorithm can be expected to be low (less than 5% for spherical, cap and slug bubbles). However, a larger error is observed for slugs with an internal cavity. Successful modifications of the original reconstruction algorithm have resulted in a reduction of error from 25% to 15%. In most experimentally observed flows, a very concave internal cavity is not expected. Thus, a conservative estimate of $\pm 10\%$ is suggested for the uncertainty associated with interfacial area concentration measurements using wire-mesh sensors.

Assessment of current IATE models against high resolution wire-mesh sensor data

Two state-of-the-art IATE models were considered for small and large diameter pipes. The Fu-Ishii model, developed for flows in small diameter pipes, was evaluated for the TOPFLOW DN50 data, while the Smith-Schlegel model, specifically developed for flows in large diameter pipes, was evaluated for the TOPFLOW DN200 data.

Assessment of the Fu-Ishii model

The performance of the two-group Fu-Ishii model was found to be good (within experimental uncertainty of $\pm 10\%$) for flows at low void-fraction, corresponding to bubbly flow regime. In such simple flows, the bubble expansion term was found to dominate the propagation of interfacial area concentration along the pipe vertical axis. At high superficial velocities, where the source/sink terms due to bubble coalescence and break-up mechanisms significantly contribute to the transport of interfacial area concentration, the IATE performance deteriorates with increasing superficial gas to liquid velocity ratio. It was found that an over-prediction of the incidence of wake entrainment yield an excessing sink for group-2 bubbles, leading to overall poor prediction of the total interfacial area concentration. Group-1 interfacial area was predicted well in almost all tests. The shearing-off mechanism was found to be a major source for group-1 a_i propagation.

The standalone IATE model (using interpolated experimental field values for closure) was then compared to the two-fluid IATE model (using the state-of-the-art system code TRACE). The two models resulted in similar performance in the bubbly flow regime. However, because

the solution of the IATE model in TRACE was contaminated by the inaccuracy of the two-fluid model to predict the axial void-fraction and gas velocity profiles, poor performance of the IATE/TRACE model was observed also at low superficial gas to liquid ratios. The poorer performance of the coupled IATE/TRACE model was mainly due to the fact that the two-fluid model implemented in TRACE is not able to accurately predict field values for group-2 bubbles (i.e. void fraction and gas velocity), leading to a poor estimation of the shearing-off mechanism, and therefore group-1 interfacial area.

Assessment of the Smith-Schlegel model

The Smith-Schlegel model was found to perform well in the bubbly flow regime, with errors in the prediction of the interfacial area concentration less than $\pm 10\%$. Similar to the Fu-Ishii model, it was shown that in the bubbly flow regime, the primary source of a_i propagation is the bubble expansion mechanism. In the churn-turbulent flow regime, large group-2 bubbles are present in the flow and the wake entrainment mechanism becomes important, together with other mechanisms such as shearing-off. Inaccurate estimation of the shearing-off mechanism for group-2 bubbles was found to yield an over-estimation of the source term for group-1 a_i resulting in poor group-1 a_i predictions. In the transition from churn-turbulent to annular flow, several interaction mechanisms have been identified that contribute to inaccurate predictions of group-1 a_i . However, wake entrainment remains the dominating mechanism for group-2 bubbles. At high void fractions, it was found that the total a_i was predicted well only as a result of compensation of errors, given that the prediction of group-wise a_i was incorrect.

Use of genetic algorithms to improve IATE performance over a wide range of flow conditions

In the assessment of current IATE model performed within this dissertation, it was concluded that the Fu-Ishii model would significantly benefit from a reconsideration of the wake entrainment of group-2 bubbles. The Smith-Schlegel model was found to perform well at high void fractions only due to a compensation of errors. The coefficients for the IATE model can only be defined experimentally and their determination for current IATE models has suffered from a lack of adequate experimental data. A genetic algorithm was selected for its capability to optimize global non-linear problems in addition to its parallelizability. The optimization was applied to both the Fu-Ishii and the Smith-Schlegel models.

Optimization of Fu-Ishii model

Although optimization of model coefficients based on individual TOPFLOW tests are not practical for implementation, they have helped identify important effects. First, for $j_g \leq 0.0151 \text{ m/s} \cap j_f \geq 0.405 \text{ m/s}$, almost no improvement to the current performance of the Fu-Ishii IATE is possible through any modification of the model coefficients. This is because at these flow conditions, the propagation of interfacial area density is dominated by the bubble expansion term, and bubble break-up and coalescence mechanisms play an insignificant role in the evolution of the interfacial area concentration.

Next a global optimization of all IATE coefficients based on all TOPFLOW DN50 data was considered. This resulted in a set of coefficients that decreased average error in prediction of total interfacial area by 18.4% over all TOPFLOW tests. Most of the improvement in the IATE model predictions stemmed from the high void fraction slug flow regime. Application of the optimized coefficients to independent Purdue data indicated that the modification of the default coefficients using a global optimization had a significant improvement for tests with similar hydraulic diameters. For smaller and larger diameter tests, the result was neutral, with a slightly improved performance at lower j_f at the cost of a slight degradation at the opposite spectrum. The principal component analysis of all the observations during the optimization procedure indicated a very high sensitivity of the model predictions to the value of the group-2 wake entrainment coefficient C_{WE}^2 .

The last optimization study focused on the modification of the group-2 wake entrainment coefficient C_{WE}^2 only, on the basis of a few (six) neighboring TOPFLOW tests in which an over-prediction of the incidence of group-2 wake entrainment mechanism was observed. The optimization resulted in a reduction of the default C_{WE}^2 coefficient from 10.0 to 0.515. The modification of the group-2 wake entrainment coefficient resulted in a significant improvement in the prediction of the total a_i for TOPFLOW tests with $j_g \geq 2 \cdot 10^{-1} \text{ m/s}$, namely 6.3% for $j_f \geq 5 \cdot 10^{-1} \text{ m/s}$ and 32.7% for $j_f < 5 \cdot 10^{-1} \text{ m/s}$. The application of the modified coefficient to Purdue 48.3 mm tests resulted in improvements of 13.3% and 24.0% for group-1 and group-2 a_i prediction, respectively. Application to other Purdue university tests (with smaller and larger diameters) indicated smaller improvement of 3.8% and 1.1% respectively, but negligible degradation in performance. Therefore, it is recommended to decrease C_{WE}^2 from its default value to 0.515.

Optimization of the Smith-Schlegel model

A substantial improvement in group-wise performance could be realized only by significant changes to all 10 coefficients in the Smith-Schlegel model. While for the Fu-Ishii model, a

principal component analysis could be used to single out the bubble break-up and coalescence mechanisms that mostly contributed to a poor performance of the model, for the Smith-Schlegel model such degeneration of most relevant bubbles interaction mechanisms was not successful.

The optimization results in improved predictions of the total interfacial area concentration at $j_g \leq 2 \cdot 10^{-1} \text{m/s}$, and in a performance deterioration slightly above this range. This is due to the issues associated with the default Smith-Schlegel model, for which it was found that the good performance for total a_i was a result of error compensation in the group-wise a_i predictions. Unfortunately, when the globally optimized coefficients on the basis of TOPFLOW DN200 data is applied to independent large-diameter data obtained at Purdue, the results are unsatisfactory. There is a significant deterioration in the prediction of group-2 a_i , while total interfacial area prediction improves moderately. As the outcome in improvement of Purdue university tests are opposite to the TOPFLOW improvements, the application of the optimized coefficients is invalid. This may be attributed to the significantly larger hydraulic diameter of the TOPFLOW pipe and a lack of scalability of two-phase flows at these conditions. The unsatisfactory results also draw attention to with the complexity of the Smith-Schlegel model. It includes a large number of mechanisms with a strong empirical nature, including 10 coefficients to be experimentally determined. Contrary to flow conditions in small diameter pipes, in flows in large diameter pipes it is more difficult to isolate individual mechanisms in the various parts of the j_g-j_f space, making it difficult to experimentally determine a valid set of model coefficients.

Future work

With the recommendation of a decrease of C_{WE}^2 from 10.0 to 0.515, the problems at high void fractions associated with the Fu-Ishii model are significantly reduced. The impact was shown to be applicable to external databases with similar hydraulic diameters (and have a negligible impact on other diameters). The next step would be to assess the performance of the Fu-Ishii model for steam-water flows that are occur in light-water reactors.

The work on the large diameter Smith-Schlegel model remains challenging. As highlighted in Section 3.4.3.3, omission of all interaction mechanisms currently achieve a better prediction of group-wise and total a_i (only the bubble expansion is a source term). Simplifying the interaction mechanisms with consideration of a population balance approach [53] might allow a better assessment of dominating interactions.

As the experimental isolation of the various bubble break-up and coalescence mechanisms is difficult, a potential solution to a deeper insight in the contribution of these mechanisms to

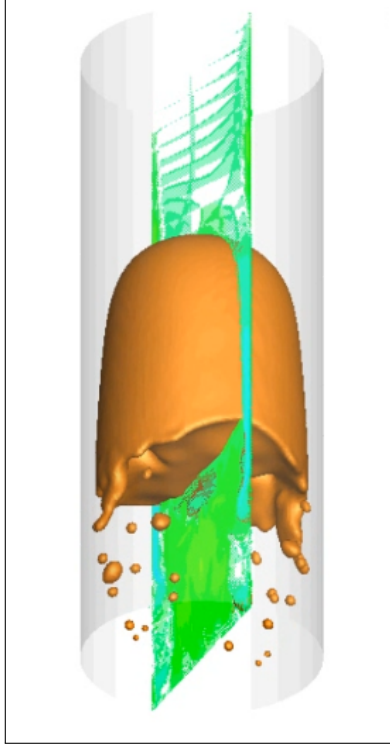


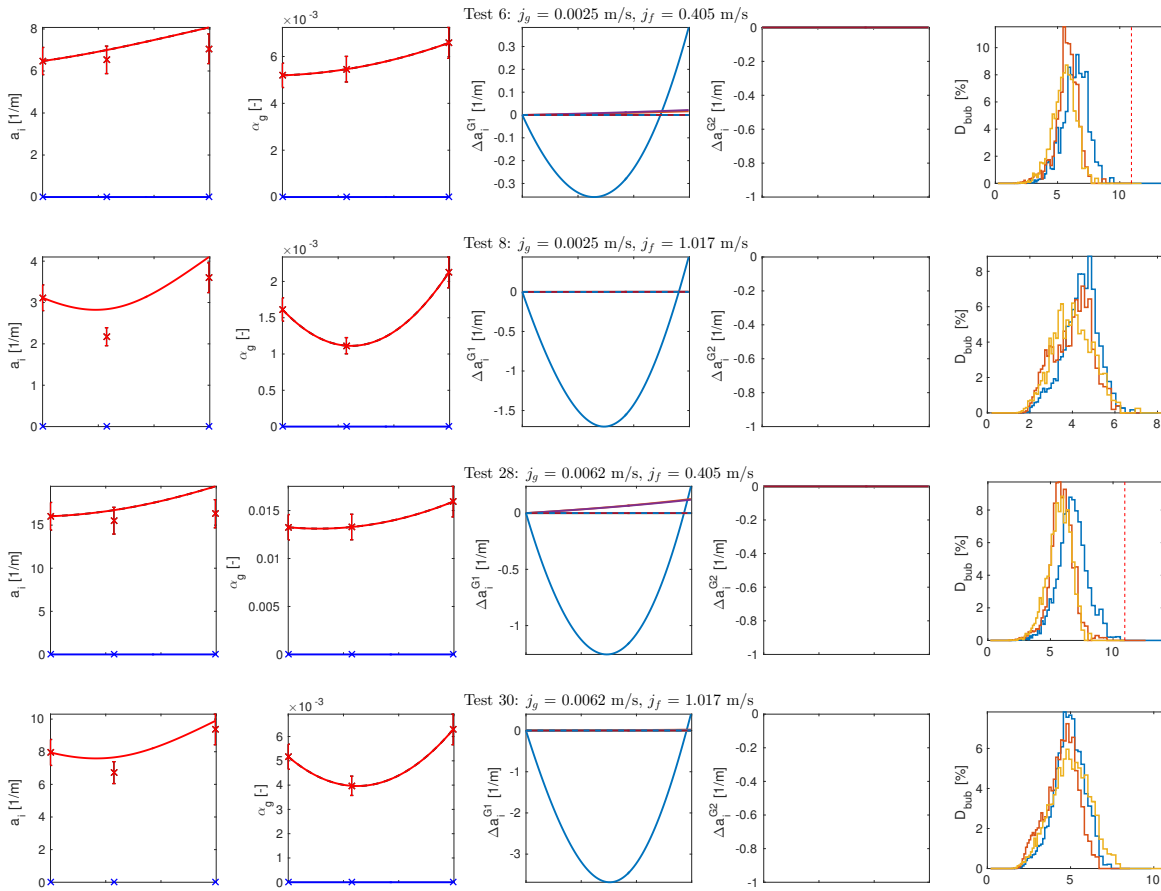
Figure 5.1: Preliminary DNS results in attempting to simulate shearing-off effects for a slug bubble.

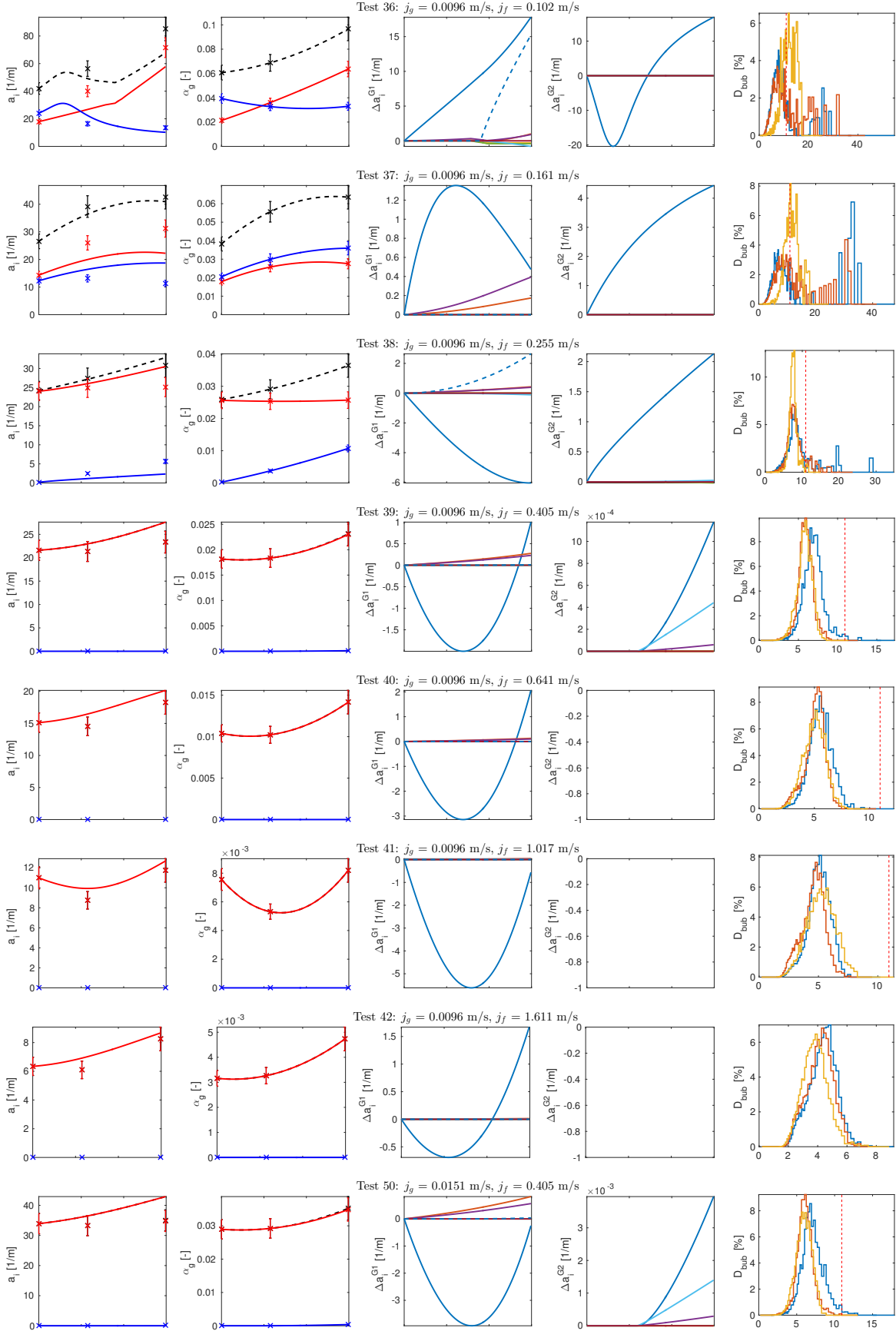
the group-wise a_i can be offered by the increasing success of Direct Numerical Simulations. Results from a preliminary investigation using a two-phase DNS code (PSI-Boil which employs Badillo's phase-field model [4]) are presented in Fig. 5.1. The simulation is attempting to improve understanding of the shearing-off mechanism.

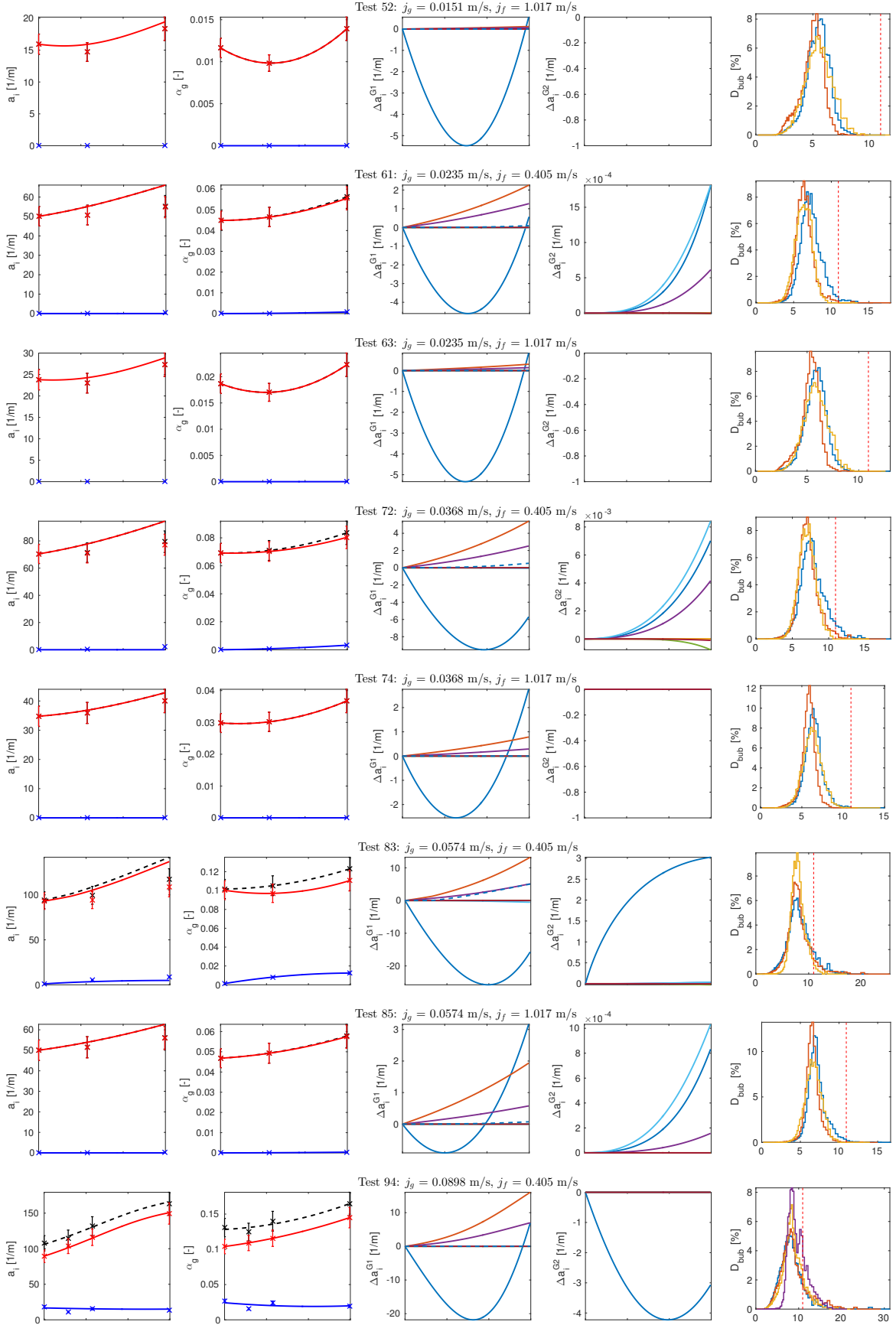
Appendix

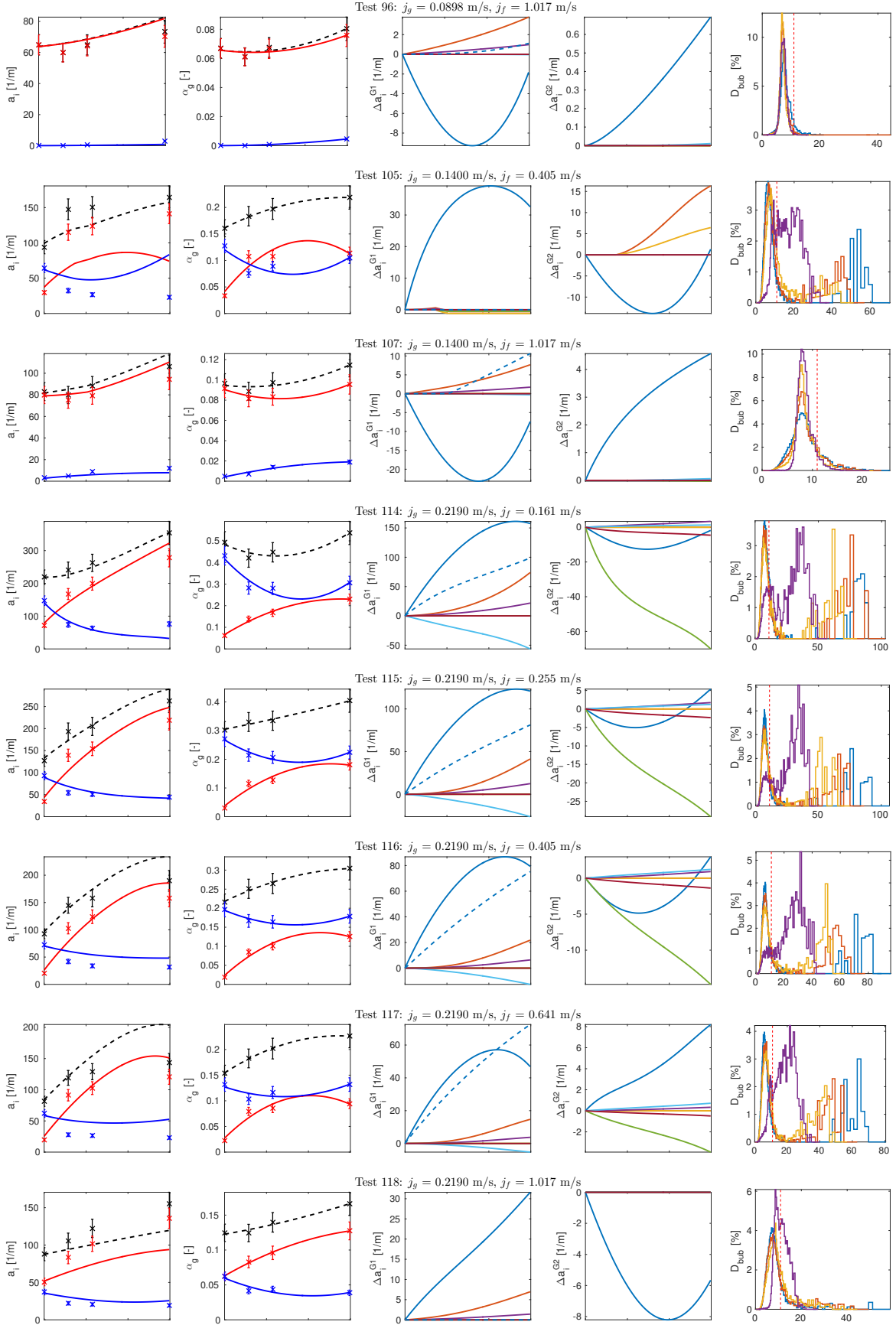
TOPFLOW DN50 evaluation with Fu-Ishii Model

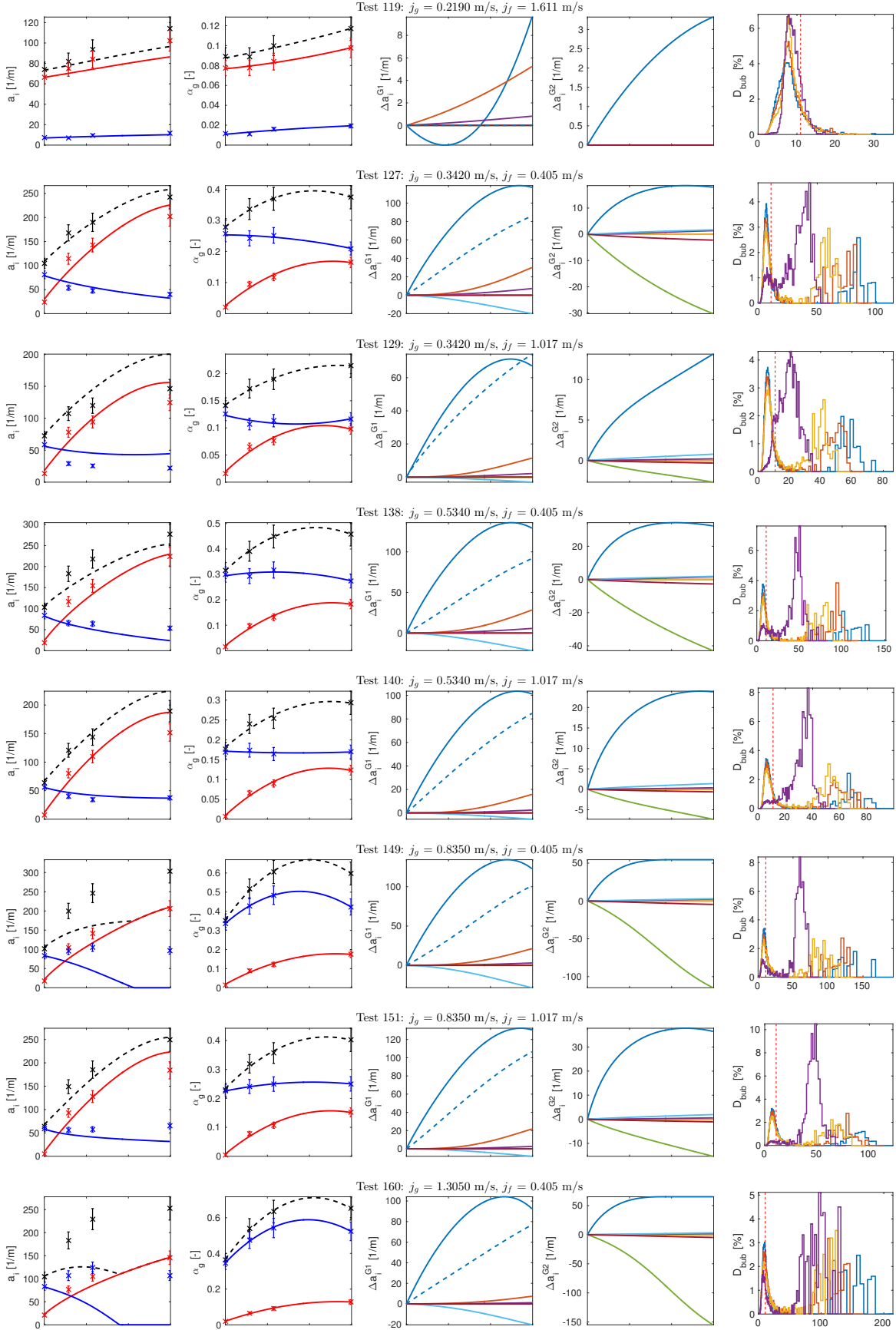
a_i	α_g	Δa_i^{G1}	Δa_i^{G2}	D_{bub}
<ul style="list-style-type: none"> ✕ Total Exp. — Total IATE ✕ G1 Exp. — G1 IATE ✕ G2 Exp. — G2 IATE 	<ul style="list-style-type: none"> ✕ Total Exp. — Total Intp. ✕ G1 Exp. — G1 Intp. ✕ G2 Exp. — G2 Intp. 	<ul style="list-style-type: none"> — ϕ_{EXP1}^1 — ϕ_{RC}^1 — $\phi_{RC1}^{11.2}$ — ϕ_{WE}^1 — $\phi_{WE}^{11.2}$ — ϕ_{WE}^{21} — $\phi_{WE1}^{12.2}$ — $\phi_{WE1}^{12.2}$ — ϕ_{TI}^1 — $\phi_{SO1}^{2,1}$ 	<ul style="list-style-type: none"> — ϕ_{EXP2}^2 — $\phi_{RC2}^{11.2}$ — $\phi_{WE2}^{11.2}$ — $\phi_{WE2}^{12.2}$ — ϕ_{TI}^2 — ϕ_{SO2}^{21} — ϕ_{WE}^2 	<ul style="list-style-type: none"> — 151 L/D — 59 L/D — 31 L/D — 2 L/D - - - D_c

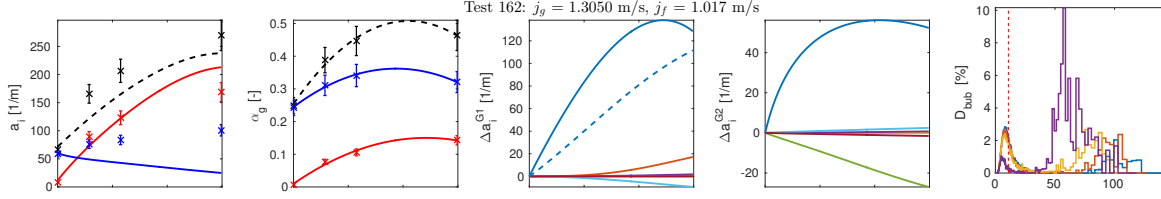






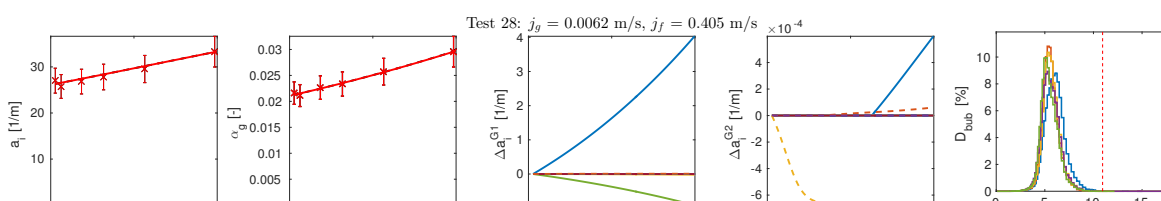
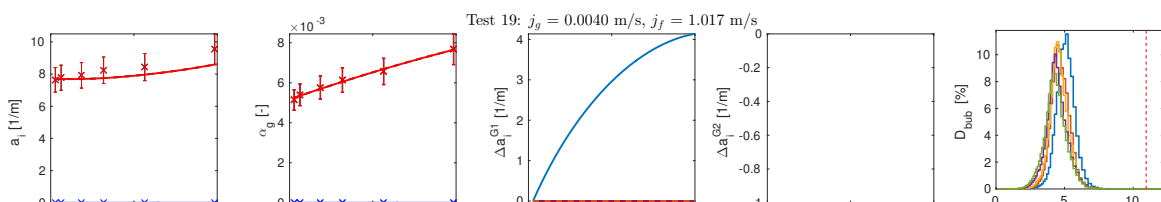
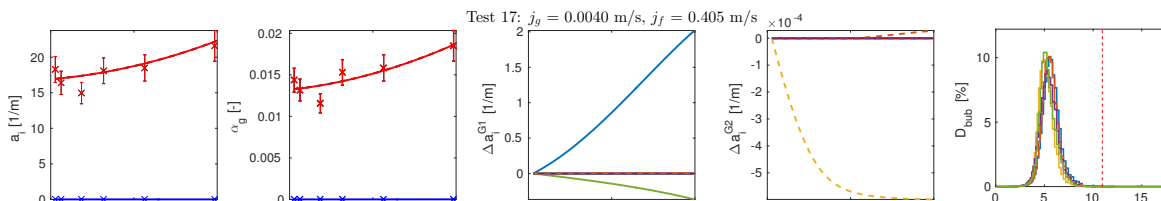
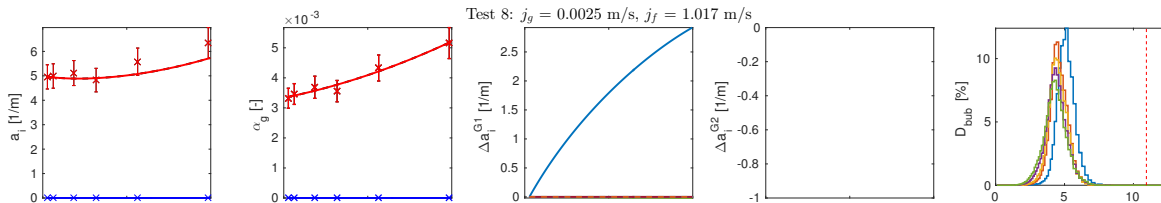
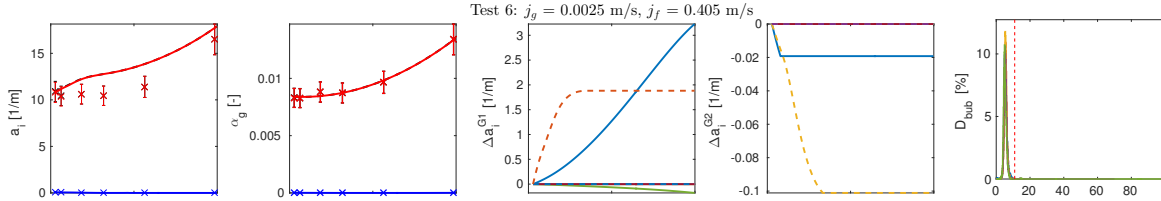


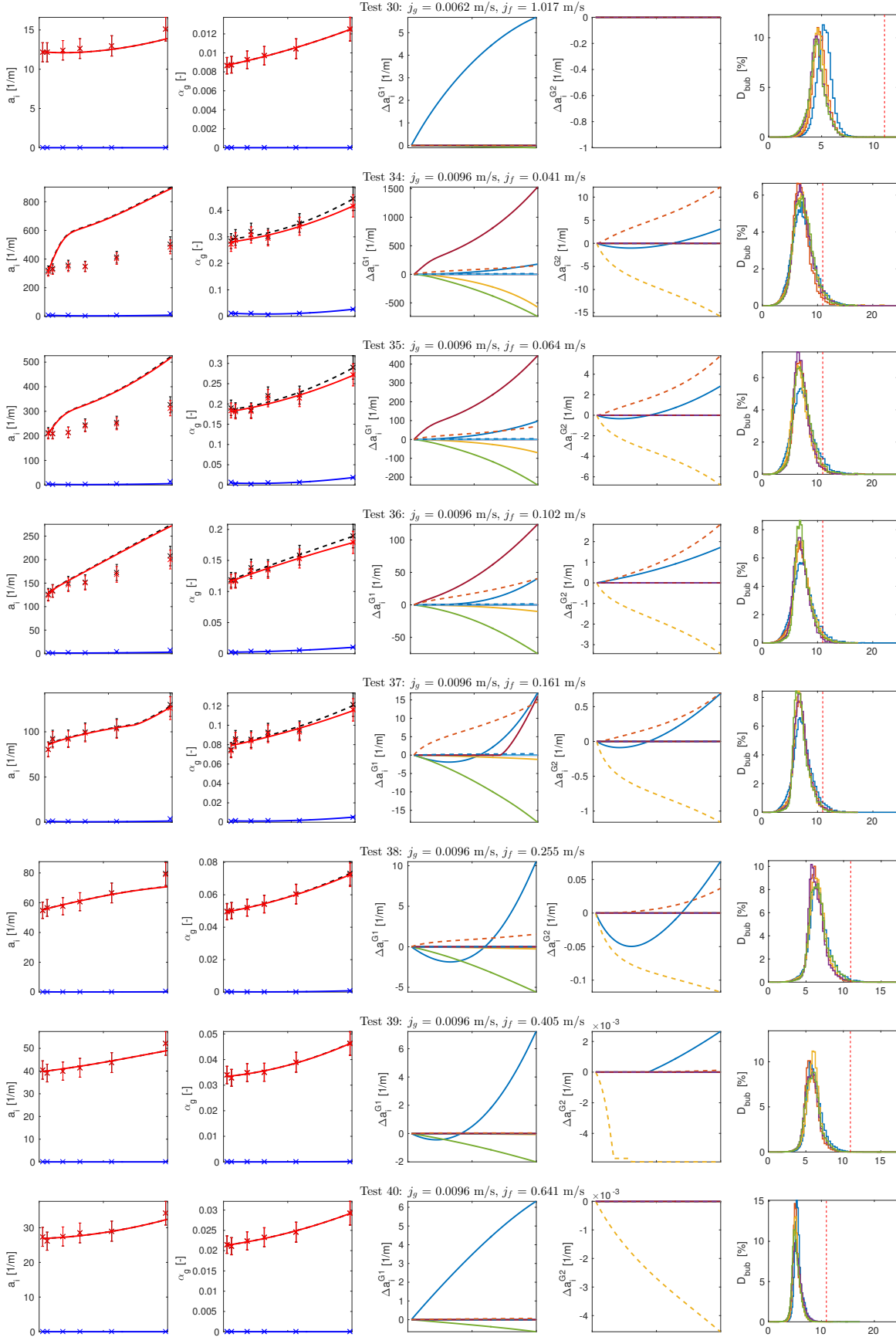


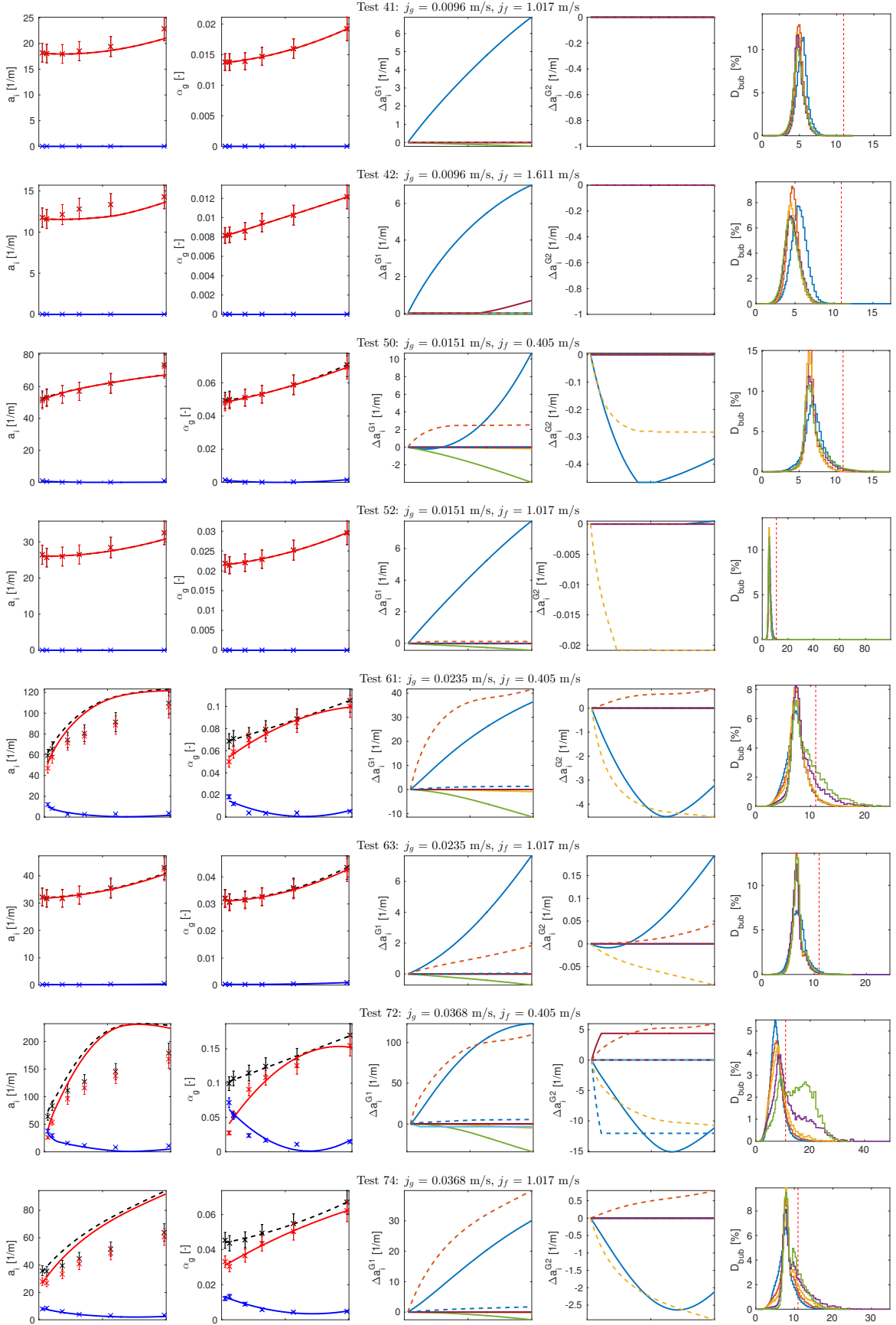


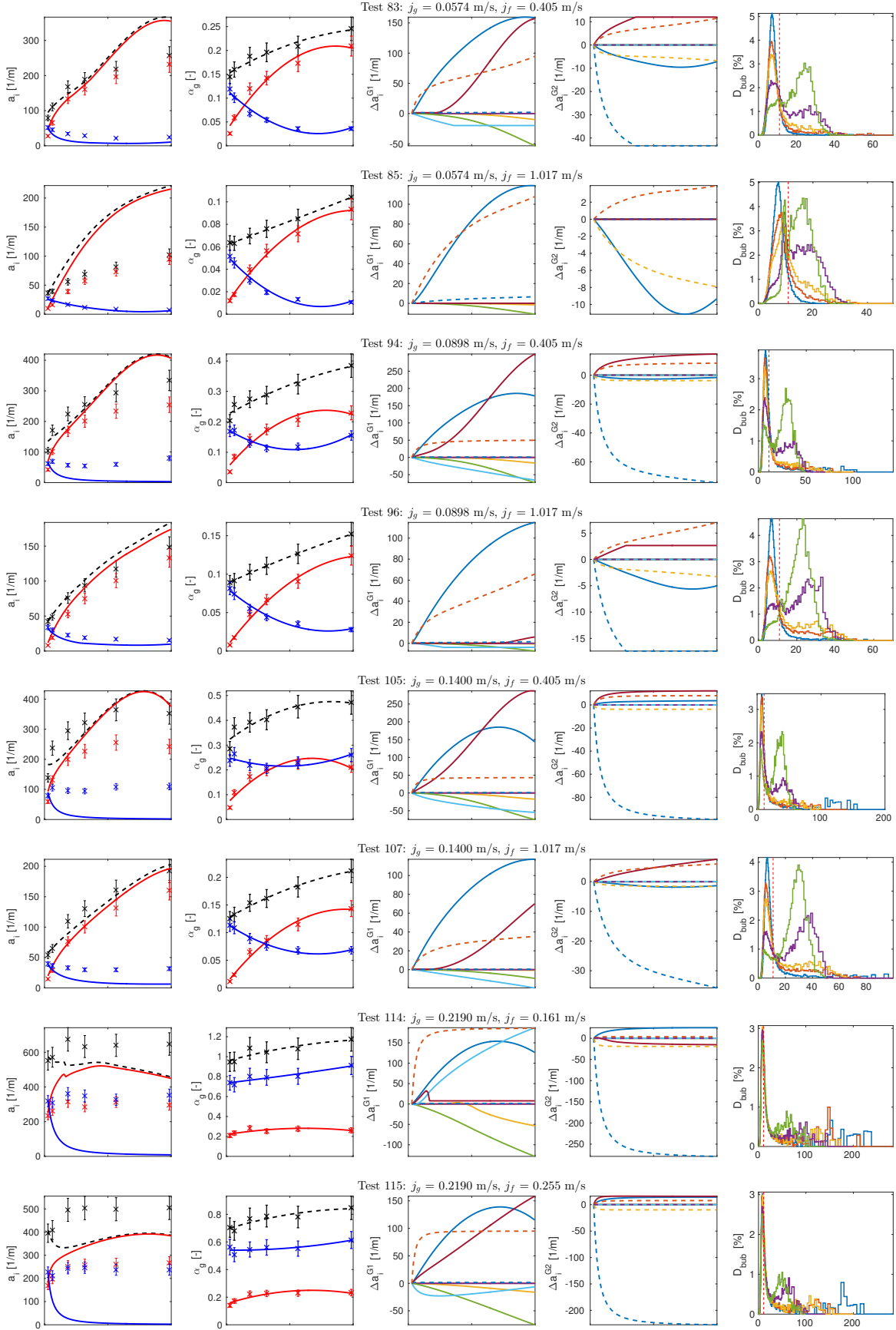
TOPFLOW DN200 evaluation with Smith-Schlegel Model

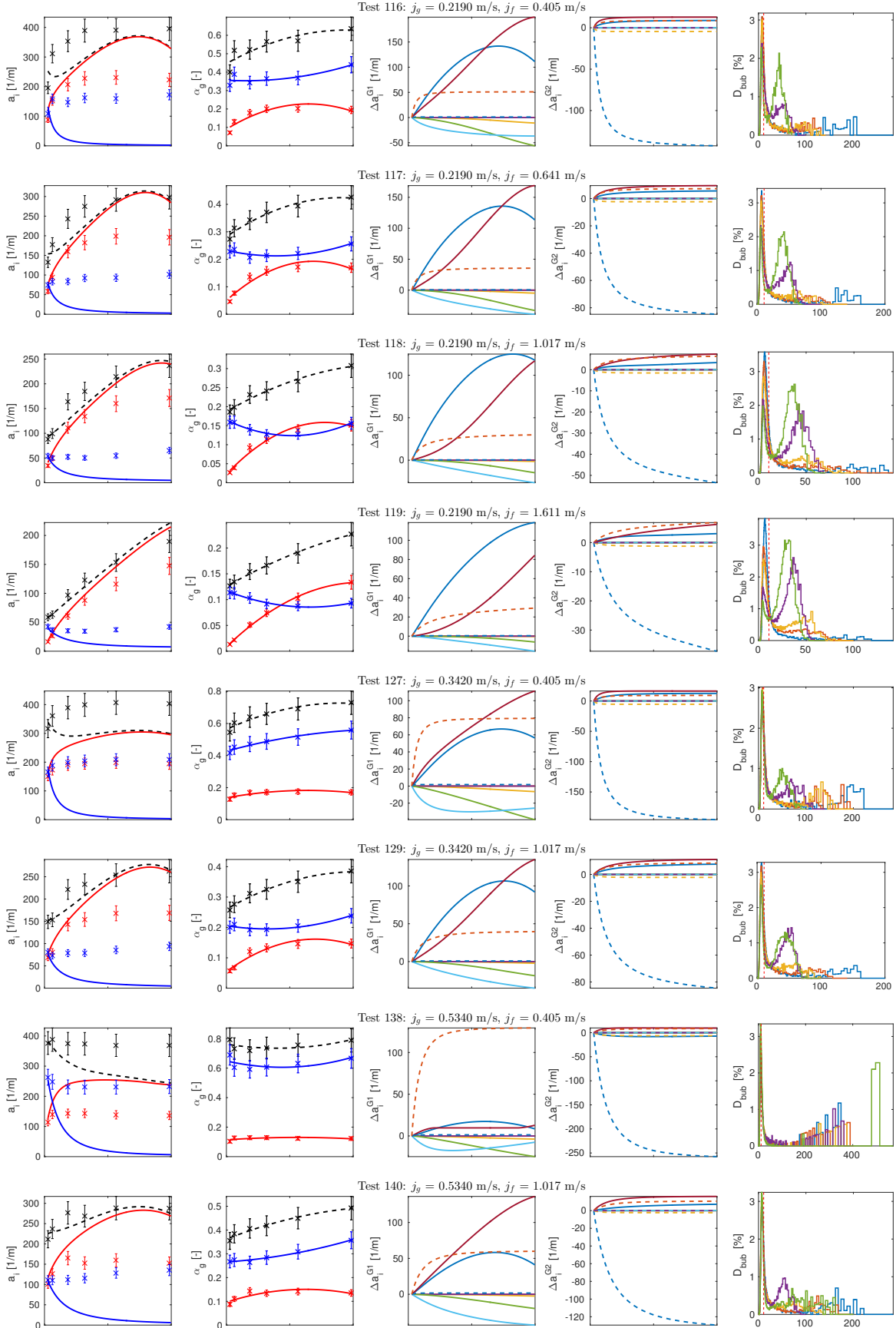
a_i	α_g	Δa_i^{G1}			Δa_i^{G2}			D_{bub}
<ul style="list-style-type: none"> × Total Exp. --- Total IATE × G1 Exp. --- G1 IATE × G2 Exp. --- G2 IATE 	<ul style="list-style-type: none"> × Total Exp. --- Total Intp. × G1 Exp. --- G1 Intp. × G2 Exp. --- G2 Intp. 	<ul style="list-style-type: none"> — ϕ_{EXP1} — ϕ_{EXP12} — ϕ_{RC}^1 	<ul style="list-style-type: none"> — $\phi_{RC1}^{12,2}$ — ϕ_{WE}^1 — $\phi_{WEL1}^{12,2}$ 	<ul style="list-style-type: none"> — ϕ_{PI}^1 — $\phi_{TIG1}^{2,1}$ — $\phi_{SO1}^{2,12}$ 	<ul style="list-style-type: none"> — ϕ_{EXP2} — ϕ_{EXP12} — $\phi_{RC2}^{11,2}$ — $\phi_{RC2}^{12,2}$ 	<ul style="list-style-type: none"> — ϕ_{RC}^2 — $\phi_{WE2}^{11,2}$ — $\phi_{WEG2}^{12,2}$ — ϕ_{WE}^2 	<ul style="list-style-type: none"> — $\phi_{TIG2}^{2,1}$ — $\phi_{SO2}^{2,12}$ — ϕ_{SI}^2 	<ul style="list-style-type: none"> — 39 L/D — 13 L/D — 7 L/D — 3 L/D — 1 L/D --- D_c

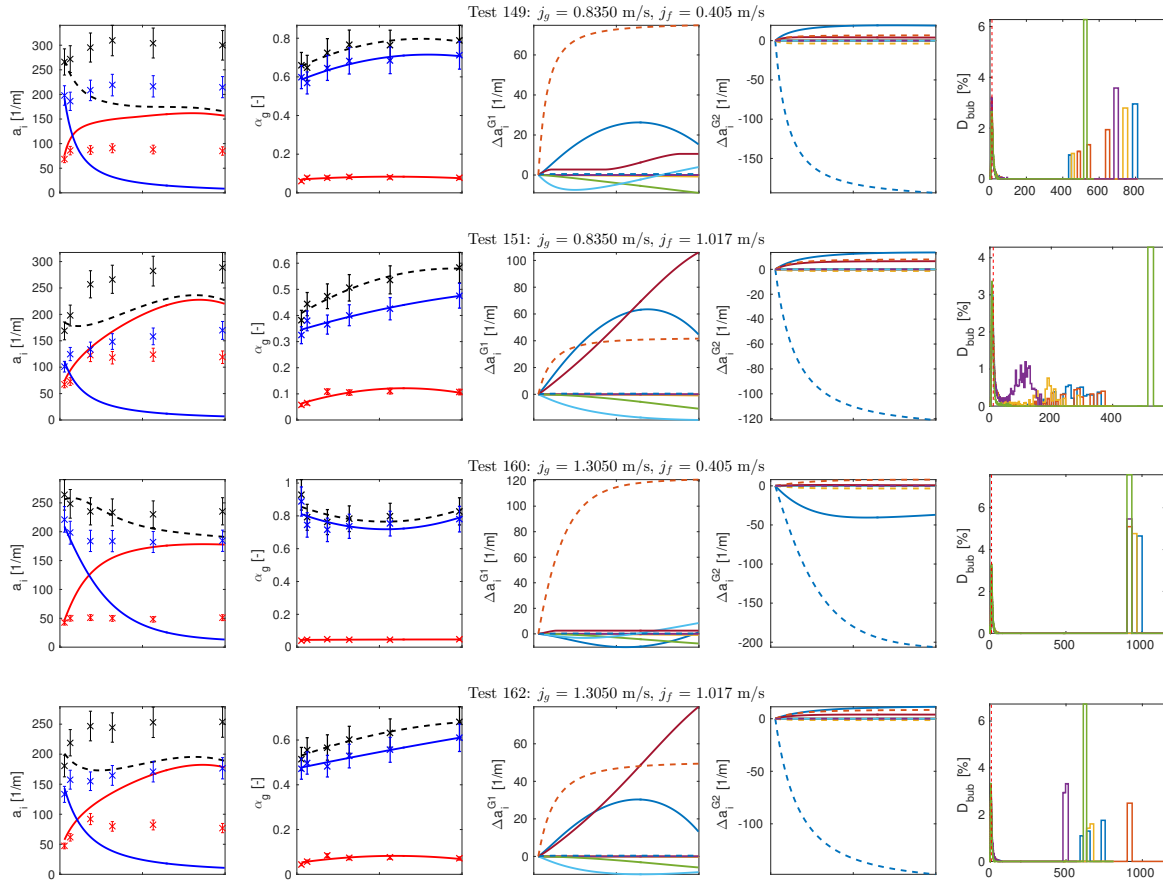












References

- [1] Nrc: Home page.
- [2] TRACE V5.0 Theory Manual. *Office of Nuclear Regulatory Research*.
- [3] C. Allison, G. Berna, R. Chambers, E. Coryell, K. Davis, D. Hagrman, D. Hagrman, N. Hampton, J. Hohorst, R. Mason, et al. Scdap/relap5/mod3. 1 code manual, volume iv: Matpro—a library of materials properties for light-water-reactor accident analysis. *DT Hagrman, NUREG/CR-6150, EGG-2720*, 4:4–234, 1993.
- [4] A. Badillo. Quantitative phase-field modeling for boiling phenomena. *Physical Review E*, 86(4):041603, 2012.
- [5] M. D. Bartel, M. Ishii, T. Masukawa, Y. Mi, and R. Situ. Interfacial area measurements in subcooled flow boiling. *Nuclear Engineering and Design*, 210(1):135–155, 2001.
- [6] M. Bernard, T. Worosz, S. Kim, C. Hoxie, and S. Bajorek. Comparison of results in the prediction of cap/slug flows between TRACE-T and TRACE V5.0 Patch 3. *The 15th International Topical Meeting on Nuclear Reactor Thermal Hydraulics*, 2013.
- [7] D. Bestion. The physical closure laws in the cathare code. *Nuclear Engineering and Design*, 124(3):229–245, 1990.
- [8] M. Beyer, D. Lucas, J. Kussin, and P. Schutz. Air-water experiments in a vertical dn200-pipe. *Wissenschaftlich-Technische Berichte*, FZD-505, 2008.
- [9] M. Bieberle and U. Hampel. Evaluation of a limited angle scanned electron beam x-ray ct approach for two-phase pipe flows. *Measurement Science and Technology*, 17(8):2057, 2006.
- [10] A. K. Biń. Gas entrainment by plunging liquid jets. *Chemical Engineering Science*, 48(21):3585–3630, 1993.
- [11] CGAL. Computational geometry algorithms library. 2015.
- [12] M. Corradini. Fundamentals of multiphase flow, online edition. 1997.
- [13] C. Coualoglou and L. Tavlarides. Description of interaction processes in agitated liquid-liquid dispersions. *Chemical Engineering Science*, 32(11):1289–1297, 1977.

- [14] A. Dave, A. Manera, M. Beyer, and D. Lucas. Evaluating performance of two-group interfacial area transport equation for vertical small diameter pipes. *Chemical Science and Engineering*, Submitted, 2016.
- [15] A. Dave, A. Manera, M. Beyer, D. Lucas, and H.-M. Prasser. Uncertainty Analysis of an Interfacial Area Reconstruction Algorithm and its application to Two Group Interfacial Area Transport Equation Validation. *Nuclear Engineering and Design*, In print, 2016.
- [16] A. E. Dukler, D. M. Maron, and N. Brauner. A physical model for predicting the minimum stable slug length. *Chemical Engineering Science*, 40(8):1379–1385, 1985.
- [17] D. Euh, B. Ozar, T. Hibiki, M. Ishii, and C.-H. Song. Characteristics of bubble departure frequency in a low-pressure subcooled boiling flow. *Journal of nuclear science and technology*, 47(7):608–617, 2010.
- [18] D. Euh, B. Yun, C. Song, T. Kwon, M. Chung, and U. Lee. Development of the five-sensor conductivity probe method for the measurement of the interfacial area concentration. *Nuclear engineering and design*, 205(1):35–51, 2001.
- [19] G. Evans, G. Jameson, and B. Atkinson. Prediction of the bubble size generated by a plunging liquid jet bubble column. *Chemical engineering science*, 47(13-14):3265–3272, 1992.
- [20] R. Fernandes, R. Semiat, and A. Dukler. Hydrodynamic model for gas-liquid slug flow in vertical tubes. *AIChE Journal*, 29(6):981–989, 1983.
- [21] T. Froystein. Flow imaging by gamma-ray tomography: Data processing and reconstruction techniques. *Frontiers in industrial process tomography II, Delft*, 1997.
- [22] X. Y. Fu and M. Ishii. Two-group Interfacial Area Transport in Vertical Air–water Flow I. Mechanistic Model. *Nuclear Engineering and Design*, 219(2):143–168, 2003.
- [23] X. Y. Fu and M. Ishii. Two-group Interfacial Area Transport in Vertical Air–water Flow II. Model Evaluation. *Nuclear Engineering and Design*, 219(2):169–190, 2003.
- [24] D. E. Goldberg. *Optimization & Machine Learning*. Addison-Wesley, 1989.
- [25] G. F. Hewitt and N. S. Hall-Taylor. Annular two-phase flow, 1970.
- [26] T. Hibiki and M. Ishii. Two-group interfacial area transport equations at bubbly-to-slug flow transition. *Nuclear Engineering and Design*, 202:39–76, 2001.
- [27] T. Hibiki and M. Ishii. Active nucleation site density in boiling systems. *International Journal of Heat and Mass Transfer*, 46(14):2587–2601, 2003.
- [28] K. Isao and I. Mamoru. Drift flux model for large diameter pipe and new correlation for pool void fraction. *International Journal of Heat and Mass Transfer*, 30(9):1927–1939, 1987.

- [29] M. Ishii. Thermo-fluid dynamic theory of two-phase flow. *NASA STI/Recon Technical Report A*, 75:29657, 1975.
- [30] M. Ishii. One-dimensional drift-flux model and constitutive equations for relative motion between phases in various flow regimes. Technical report, Argonne National Lab., IL (USA), 1977.
- [31] M. Ishii and T. Chawla. Local drag laws in dispersed two-phase flow. Technical report, Argonne National Lab., IL (USA), 1979.
- [32] M. Ishii and T. Hibiki. *Thermo-Fluid Dynamics of Two-Phase Flow*. SpringerLink: Bücher. Springer New York, 2010.
- [33] M. Ishii and S. Kim. Development of One-group and Two-group Interfacial Area Transport Equation. *Nuclear Science Engineering*, 146(3):257–273, 2003.
- [34] M. Ishii, S. Kim, X. Y. Fu, T. R. Smith, S. S. Paranjape, X. Sun, H. Goda, J. Uhle, and J. Kelly. Experimental investigation of the interfacial area transport in vertical two-phase flow. Purdue University, 2003.
- [35] M. Ishii and G. Kojasoy. Interfacial area transport equation and preliminary considerations for closure relations. In *Technical report, PU-NE-93/6*. Nuclear Engineering Department, Purdue University West Lafayette, IN, 1993.
- [36] M. Ishii and K. Mishima. Study of two-fluid model and interfacial area. Technical report, Argonne National Lab., IL (USA), 1980.
- [37] M. Ishii and K. Mishima. Two-fluid model and hydrodynamic constitutive relations. *Nuclear Engineering and design*, 82(2):107–126, 1984.
- [38] M. Ishii and N. Zuber. Drag coefficient and relative velocity in bubbly, droplet or particulate flows. *AIChE Journal*, 25(5):843–855, 1979.
- [39] S. Kim. *Interfacial Area Transport Equation and Measurement of Local Interfacial Characteristics*. PhD thesis, Purdue University, 1999.
- [40] S. Kim, X. Fu, X. Wang, and M. Ishii. Development of the miniaturized four-sensor conductivity probe and the signal processing scheme. *International journal of heat and mass transfer*, 43(22):4101–4118, 2000.
- [41] G. Kocamustafaogullari and M. Ishii. Interfacial area and nucleation site density in boiling systems. *International Journal of Heat and Mass Transfer*, 26(9):1377–1387, 1983.
- [42] G. Kocamustafaogullari and M. Ishii. Foundation of the interfacial area transport equation and its closure relation. *International Journal of Heat and Mass Transfer*, 38(481), 1995.

- [43] S. B. Kumar, D. Moslemian, and M. P. Duduković. A γ -ray tomographic scanner for imaging voidage distribution in two-phase flow systems. *Flow Measurement and Instrumentation*, 6(1):61–73, 1995.
- [44] G. Lerchl and H. Austregesilo. Athlet mod 1.2 cycle a, user’s manual. *Code Doc. Package, GRS-P-1*, 1, 1998.
- [45] Y. Liao and D. Lucas. A literature review of theoretical models for drop and bubble breakup in turbulent dispersions. *Chemical Engineering Science*, 64(15):3389–3406, 2009.
- [46] Y. Liao and D. Lucas. A literature review on mechanisms and models for the coalescence process of fluid particles. *Chemical Engineering Science*, 65(10):2851–2864, 2010.
- [47] A. Manera. *Experimental and analytical investigations on flashing-induced instabilities in natural circulation two-phase systems*. PhD thesis, Delft University of Technology, 2003.
- [48] A. Manera, B. Ozar, S. Paranjape, M. Ishii, and H.-M. Prasser. Comparison between wire-mesh sensors and conductive needle-probes for measurements of two-phase flow parameters. *Nuclear Engineering and Design*, 239:1718–1724, 2008.
- [49] A. Manera, H. Prasser, T. Van der Hagen, R. Mudde, and W. de Kruijf. A comparison of void-fraction measurements during flashing-induced instabilities obtained with a wire-mesh sensor and a gamma-transmission set-up. *ICMF-2001, New Orleans, May*, 2001.
- [50] A. Manera, H.-M. Prasser, D. Lucas, and T. Van Der Hagen. Three-dimensional flow pattern visualization and bubble size distributions in stationary and transient upward flashing flow. *International journal of multiphase flow*, 32(8):996–1016, 2006.
- [51] K. Mishima and M. Ishii. Flow regime transition criteria for upward two-phase flow in vertical tubes. *International Journal of Heat and Mass Transfer*, 27(5):723–737, 1984.
- [52] R. Moissis and P. Griffith. Entrance effects in a two-phase slug flow. *J. Heat Transfer*, 84(1):29–38, 1962.
- [53] G. Montoya, D. Lucas, E. Baglietto, and Y. Liao. A review on mechanisms and models for the churn-turbulent flow regime. *Chemical Engineering Science*, 141:86–103, 2016.
- [54] L. Neal and S. Bankoff. A high resolution resistivity probe for determination of local void properties in gas-liquid flow. *AIChE Journal*, 9(4):490–494, 1963.
- [55] A. Ohnuki and H. Akimoto. Experimental study on transition of flow pattern and phase distribution in upward air–water two-phase flow along a large vertical pipe. *International journal of multiphase flow*, 26(3):367–386, 2000.
- [56] H.-S. Park, T.-H. Lee, T. Hibiki, W.-P. Baek, and M. Ishii. Modeling of the condensation sink term in an interfacial area transport equation. *International Journal of Heat and Mass Transfer*, 50(25):5041–5053, 2007.

- [57] H.-M. Prasser. Wire-mesh sensors for two-phase flow investigations. *Institute of Safety Research*, 23, 1999.
- [58] H.-M. Prasser, M. Beyer, A. Böttger, H. Carl, D. Lucas, A. Schaffrath, P. Schütz, F.-P. Weiss, and J. Zschau. Influence of the pipe diameter on the structure of the gas-liquid interface in a vertical two-phase pipe flow. *Nuclear Technology*, 152(1):3–22, 2005.
- [59] H.-M. Prasser, A. Böttger, and J. Zschau. A new electrode-mesh tomograph for gas-liquid flows. *Flow Measurement and Instrumentation*, 9, 1998.
- [60] H.-M. Prasser, D. Lucas, M. Beyer, C. Vallee, E. Krepper, T. Hohne, A. Manera, H. Carl, H. Pietruske, P. Schutz, A. Zaruba, S. A. Issa, J.-M. Shi, and F.-P. Weib. Construction and execution of experiments at the multi-purpose thermal hydraulic test facility TOPFLOW for generic investigations of two-phase flows and the development and validation of CFD codes. *Wissenschaftlich-Technische Berichte*, FZD-481, 2007.
- [61] H.-M. Prasser, M. Misawa, and I. Tseanu. Comparison between wire-mesh sensor and ultra-fast X-ray tomograph for an air-water flow in a vertical pipe. *Flow Measurement and Instrumentation*, 16, 2005.
- [62] H.-M. Prasser, D. Scholz, and C. Zippe. Bubble size measurement using wire-mesh sensors. *Flow measurement and Instrumentation*, 12(4):299–312, 2001.
- [63] A. Prosperetti and G. Tryggvason. *Computational methods for multiphase flow*. Cambridge university press, 2009.
- [64] J. P. Schlegel and T. Hibiki. A correlation for interfacial area concentration in high void fraction flows in large diameter channels. *Chemical Engineering Science*, 131:172–186, 2015.
- [65] J. P. Schlegel, T. Hibiki, and M. Ishii. Two-group modeling of interfacial area transport in large diameter channels. *Nuclear Engineering and Design*, 293:75–86, 2015.
- [66] J. P. Schlegel, S. Miwa, S. Chen, T. Hibiki, and M. Ishii. Experimental study of two-phase flow structure in large diameter pipes. *Experimental Thermal and Fluid Science*, 41:12–22, 2012.
- [67] J. P. Schlegel, P. Sawant, S. Paranjape, B. Ozar, T. Hibiki, and M. Ishii. Void fraction and flow regime in adiabatic upward two-phase flow in large diameter vertical pipes. *Nuclear Engineering and Design*, 239(12):2864–2874, 2009.
- [68] H. Schlichting. *Boundary layer theory*, 1979.
- [69] D. Schmitz, N. Reinecke, G. Petritsch, and D. Mewes. High resolution x-ray tomography for stationary multiphase flows. OECD/CSNI Specialist Meeting on Advanced Instrumentation and Measurement Techniques, Santa Barbara, CA, 1997.
- [70] S. Sharaf, M. Da Silva, U. Hampel, C. Zippe, M. Beyer, and B. Azzopardi. Comparison between wire mesh sensor and gamma densitometry void measurements in two-phase flows. *Measurement Science and Technology*, 22(10):104019, 2011.

- [71] X. Shen, Y. Saito, K. Mishima, and H. Nakamura. A study on the characteristics of upward air–water two-phase flow in a large diameter pipe. *Experimental thermal and fluid science*, 31(1):21–36, 2006.
- [72] R. Situ, M. Ishii, T. Hibiki, J. Tu, G. H. Yeoh, and M. Mori. Bubble departure frequency in forced convective subcooled boiling flow. *International Journal of Heat and Mass Transfer*, 51(25):6268–6282, 2008.
- [73] T. R. Smith. *Two-group Interfacial Area Transport Equation in Large Diameter Pipes*. PhD thesis, Purdue University, 2002.
- [74] T. R. Smith, J. P. Schlegel, T. Hibiki, and M. Ishii. Mechanistic modeling of interfacial area transport in large diameter pipes. *International Journal of Multiphase Flow*, 47:1–16, 2012.
- [75] T. R. Smith, J. P. Schlegel, T. Hibiki, and M. Ishii. Two-phase flow structure in large diameter pipes. *International Journal of Heat and Fluid Flow*, 33(1):156–167, 2012.
- [76] X. Sun, M. Ishii, and J. M. Kelly. Modified two-fluid model for the two-group interfacial area transport equation. *Annals of Nuclear Energy*, 30(16):1601–1622, 2003.
- [77] X. Sun, S. Kim, M. Ishii, and S. G. Beus. Modeling of bubble coalescence and disintegration in confined upward two-phase flow. *Nuclear Engineering and Design*, 230(1):3–26, 2004.
- [78] X. Sun, T. R. Smith, S. Kim, M. Ishii, and J. Uhle. Interfacial area of bubbly flow in a relatively large diameter pipe. *Experimental thermal and fluid science*, 27(1):97–109, 2002.
- [79] J. Talley, S. Kim, J. Mahaffy, S. Bajorek, and K. Tien. Implementation and evaluation of one-group interfacial area transport equation in TRACE. *Nuclear Engineering and Design*, 241(3):865–873, 2011.
- [80] W. Wangjiraniran, Y. Motegi, S. Richter, H. Kikura, M. Aritomi, and K. Yamamoto. Intrusive effect of wire mesh tomography on gas-liquid flow measurement. *Journal of nuclear science and technology*, 40(11):932–940, 2003.
- [81] Q. Wu and M. Ishii. Sensitivity study on double-sensor conductivity probe for the measurement of interfacial area concentration in bubbly flow. *International Journal of Multiphase Flow*, 25(1):155–173, 1999.
- [82] Q. Wu, S. Kim, M. Ishii, and S. Beus. One-group interfacial area transport in vertical bubbly flow. *International Journal of Heat and Mass Transfer*, 41(8):1103–1112, 1998.
- [83] Z. Zhang, M. Bieberle, F. Barthel, L. Szalinski, and U. Hampel. Investigation of upward cocurrent gas–liquid pipe flow using ultrafast x-ray tomography and wire-mesh sensor. *Flow Measurement and Instrumentation*, 32:111–118, 2013.